Title

A Study of Voltage-Gated Ion Channels and the Anomalous Diffusion of Membrane Proteins using Molecular Simulations

Permalink

https://escholarship.org/uc/item/0r66583p

Author

Geragotelis, Andrew Damien

Publication Date

2019

Peer reviewed|Thesis/dissertation

UNIVERSITY OF CALIFORNIA,
IRVINE

A Study of Voltage-Gated Ion Channels and the Anomalous Diffusion of Membrane Proteins
using Molecular Simulations

DISSERTATION

submitted in partial satisfaction of the requirements
for the degree of

DOCTOR OF PHILOSOPHY

in Chemistry

by

Andrew Damien Geragotelis

Dissertation Committee:
Professor Douglas J. Tobias, Chair
Professor Ioan Andricioaei
Associate Professor Francesco Tombola

2019

DEDICATION

To

my parents, Mary and Nick,
and my brother, Jeremy

TABLE OF CONTENTS

LIST OF FIGURES

LIST OF TABLES

ACKNOWLEDGMENTS

I would like to express the deepest appreciation to my advisor and committee chair, Professor Douglas Tobias. Without his guidance and support this dissertation would not have been possible. He has been a great inspiration to me in becoming a better scientist and teacher. I have learned so much in the past several years in his research group and always appreciated his guidance. I could not have hoped for a better advisor and someone who was willing to let me explore my interests.

I would also like to thank my committee members, Professor Ioan Andricioaei and Professor Francesco Tombola, who have provided me with inspiration and insight. Their knowledge depth and eagerness to share it with others has been truly motivational.

Another important thanks goes out to Professor Kimberly Edwards and Professor Stacey Littlejohn for their support, guidance, and motivation as I pursue a career in teaching college chemistry.

Lastly, I am grateful for all of my friends and family and their support on my journey to this point. I cannot imagine getting to where I am now without them.

Andrew D. Geragotelis
Curriculum Vitae

Education

August 2019   Ph.D. in Chemistry, University of California, Irvine
                              Research Area: Theoretical and Computational Chemistry
                              Thesis Advisor: Professor Douglas Tobias

December 2018   M.S. in Chemistry, University of California, Irvine

May 2013   B.S. in Chemistry, Siena College, Loudonville, NY
                              Minors: Physics and Mathematics

Research Experience

2013 – present   University of California, Irvine
                              Graduate Thesis Research
                              Advisor: Professor Douglas Tobias
                              My graduate work consists of two main research areas: using molecular dynamics simulations to study the dynamics and regulation of voltage-gated ion channels and using statistical analysis tools to uncover the mechanisms of anomalous subdiffusion of membrane proteins from simulations and experiments.

2012 – 2013   Siena College, Loudonville, NY
                              Undergraduate research project
                              Advisor: Professor George Barnes
                              I used mixed quantum mechanics/molecular mechanics simulations to study the fragmentation of small peptides and organic molecules on a chemically modified self-assembled monolayer (SAM) surface. I also performed some parameterization for modelling the interactions between small organic radical species and the modified SAM surface.

2012   University of Vermont, Burlington, VT
                              REU on Complex Materials
                              Advisor: Professor Dennis Clougherty
                              I competed a summer REU in the Physics department where I studied the adsorption of hydrogen gas on graphene surfaces. I wrote a Matlab code to calculate transition probabilities using on Fermi's Golden Rule.

2009 – 2011   Siena College, Loudonville, NY
                              Undergraduate research project

Advisor: Professor William Kennerly
As a first and second-year student, I helped design computational chemistry lab experiments for the inorganic chemistry course. My task was to write detailed procedures and test different methods using the Spartan quantum chemistry program. An experiment on Walsh Correlation Diagrams is published in *The Chemical Educator*.

Publications

Tronin, A. Y.; Maciunas, L.; Grasty, K. C.; Loll, P. J.; Ambaye, H.; Parizzi, A.; Lauter, V.; **Geragotelis, A. D.**; Freites, J. A.; Tobias, D. J.; Blasie, J. K. Direct Evidence for Conformational Changes Associated with Voltage-Gating in Kv-Channels. *Biophys. J.* **2019**, *117*, 1–16.

Geragotelis, A. D.; Edwards, K. D. Integrating Computational Chemistry in the General Chemistry Laboratory: Combining Laboratory Experiments with Computational Modeling. *Chem. Educ.* **2018**, *23*, 52-57.

Geragotelis, A.; Barnes, G. L. Surface Deposition Resulting from Collisions between Diglycine and Chemically Modified Alkylthiolate Self-Assembled Monolayer Surfaces. *J. Phys. Chem.* C. **2013**, *117*, 13087-93.

Kennerly, W. W.; Billings, K. B.; **Geragotelis, A. D.**; O'Donnell, J. L. A Computational Approach to Walsh Correlation Diagrams for the Inorganic Chemistry Curriculum. *Chem. Educ*. **2012**, *17*, 57–63.

Publications In-preparation

Geragotelis, A. D.; Freites, J. A.; Tobias, D. J. Modeling diffusion of membrane-bound signaling proteins. *In preparation*.

Geragotelis, A. D.; Wood, M. L.; Goeddeke, H.; Hong, L.; Freites, J. A.; Tombola, F.; Tobias, D. J. Microsecond simulations of an open state model of the human Hv1 proton channel. *In preparation*.

Lim, V. T.; **Geragotelis, A. D.**; Lim, N. M.; Freites, J. A.; Tombola, F.; Mobley, D. L.; Tobias, D. J. Insights on small molecule binding of the Hv1 proton channel from free energy calculations. *In preparation*.

Conference Posters

Geragotelis, A.; Wood, M. L.; Goeddeke, H.; Riahi, S. Freites, J. A.; Tombola, F.; Tobias, D. J. Multi-Microsecond Molecular Dynamics Simulations of the Hv1 Proton Channel. 2nd Annual SoCal TheoChem Meeting, Irvine, CA. **2017**.

Lim, V.; **Geragotelis, A**.; Lim, N.; Freites, J. A.; Mobley, D.; Tobias, D. J. Molecular modeling of small molecule inhibitors of the Hv1 proton channel. 253rd ACS National Meeting, San Francisco, CA. **2017**.

Geragotelis, A.; Wood, M. L,; Goeddeke, H.; Riahi, S. Freites, J. A.; Tombola, F.; Tobias, D. J. Multi-Microsecond Molecular Dynamics Simulations of the Hv1 Proton Channel. 60th Biophysical Society Annual Meeting, Los Angeles, CA. **2016**.

Geragotelis, A.; Clougherty, D. P. Investigating the Sticking of Hydrogen on Graphene. 245th ACS National Meeting, New Orleans, LA. **2013**.

Geragotelis, A.; Barnes, G. L. Surface Deposition Resulting from Collisions between Diglycine and Chemically Modified Alkylthiolate Self-Assembled Monolayer Surfaces. Eastern NY ACS Local Section Meeting, Albany, NY. **2013**.

Presentations

2018	*Anomalous Subdiffusion of Peripheral Membrane Proteins* Molecular Dynamics Seminar, UC Irvine	
2018	*Anomalous subdiffusion of the Piezo1 channel* TEMPO Group, UC Irvine	
2018	*Anomalous Diffusion of Membrane Proteins from Experiment and Simulation* Chemical & Structural Biology Seminar, UC Irvine	
2015	*Multi-Microsecond Molecular Dynamics Simulations of the Hv1 Proton Channel* Molecular Dynamics Seminar, UC Irvine	

ABSTRACT OF THE DISSERTATION

A Study of Voltage-Gated Ion Channels and the Anomalous Diffusion of Membrane Proteins
using Molecular Simulations

By

Andrew Damien Geragotelis

Doctor of Philosophy in Chemistry

University of California, Irvine, 2019

Professor Douglas J. Tobias, Chair

Molecular Dynamics simulations were used to study a variety of biophysical systems. The first of these used multi-microsecond simulations to model the activation of the Hv1 voltage-gated proton channel under a depolarizing membrane potential. The generated model reproduced several important experimental measurements and provided insight into the conformational change of the protein in response to the membrane potential. The second project involved modeling several different voltage-gated K^+ channels in open and closed states to compare with neutron and x-ray scattering experiments. Voltage-dependent changes in the membrane profile structure and comparison with atomistic models demonstrated a large inward translation of the voltage-sensing domain S4 helix and a de-wetting of the cytoplasmic half of the pore. The third project utilized multi-microsecond simulations of two peripheral membrane proteins, the C2 domain and PH domain, to study their diffusion on the membrane surface. Both proteins were found to exhibit anomalous diffusion for timescales on the order of 10 ns. Lastly, various statistical analyses were performed on trajectories of the mechanosensitive Piezo1 ion channel obtained using single-

particle tracking experiments to elucidate the behavior of the diffusion. The Piezo1 motion was found to be subdiffusive, relying on a mixed model to describe the behavior.

Chapter 1

Introduction

1.1 Molecular dynamics simulations

Computer simulations of molecules can serve as a useful tool for extracting information about the energetics and dynamics. One such method, molecular dynamics (MD) simulations, propagates atomic positions in time by integrating Newton's equations of motion, $\frac{d\mathbf{r}_i(t)}{dt} = \mathbf{v}_i(t)$ and $\frac{d\mathbf{v}_i(t)}{dt} = \frac{\mathbf{F}_i(t)}{m_i}$, for particle i, the position $\mathbf{r}_i(t)$, velocity $\mathbf{v}_i(t)$, and mass, m_i, where the force can be expressed as the gradient of the potential energy, $\mathbf{F}_i = -\nabla_i V$.

The potential energy is a function of all $3N$ atomic positions. Due to the complexity of this function, there is no analytical solution to the equations of motion, and they must be solved numerically. There are several algorithms with which this is performed, but a commonly used one is the Velocity Verlet algorithm.[1] The atomic positions and velocities are calculated as

$$\mathbf{r}_i(t + \delta t) = \mathbf{r}_i(t) + \mathbf{v}_i(t)\delta t + \frac{\delta t^2}{2m_i}\mathbf{F}_i(t) \qquad (1.1a)$$

and

$$\mathbf{v}_i(t + \delta t) = \mathbf{v}_i(t) + \frac{\delta t}{2m_i}[\mathbf{F}_i(t) + \mathbf{F}_i(t + \delta t)] \qquad (1.1b)$$

Early landmarks in the use of MD simulations include a condensed phase system of hard spheres by Alder and Wainwright in the late 1950s,[2,3] the use of a continuous potential for liquid argon by Rahman in 1964,[4] and Verlet in 1967,[5] liquid water simulations in 1971 and 1974 by Stillinger and Rahman,[6,7] and the first protein simulation in 1977 by McCammon, Gelin and Karplus.[8]

The potential energy function describes how the atoms interact with each other. This is typically additive for the different types of interactions, using various empirical parameters. For simulations of biological systems, one of the commonly used empirical force-fields is CHARMM.[9] The CHARMM potential energy function has the form

$$U(\vec{R}) = \sum_{\text{bonds}} K_b (b - b_0)^2 \tag{1.2}$$

$$+ \sum_{\text{angles}} K_\theta (\theta - \theta_0)^2$$

$$+ \sum_{\text{dihedrals}} K_\chi [1 + \cos(n\chi - \sigma)] + \sum_{\text{impropers}} K_{imp} (\varphi - \varphi_0)^2$$

$$+ \sum_{\text{nonbond}} \left(\epsilon \left[\left(\frac{R_{\min,ij}}{r_{ij}} \right)^{12} - \left(\frac{R_{\min,ij}}{r_{ij}} \right)^6 \right] + \frac{q_i q_j}{\epsilon_1 r_{ij}} \right)$$

where K_b, K_θ, K_χ, and K_{imp} are the force constants for the bond, angle, dihedral, and improper dihedral angle, respectively. The bonds between atoms b, angles θ, and improper torsion angles φ, are modeled as harmonic potentials centered at the equilibrium values (with subscript 0). The dihedral torsions of four bonded atoms are modeled by a periodic potential with periodicity n around angle χ with phase-shift σ. Pair-wise interactions between nonbonded atoms use a Lennard-Jones 6-12 potential function for the van der Waals force with well depth ϵ and distance to the minimum $R_{\min}$. Electrostatic interactions are modeled with the Coulombic potential between

two atoms of charges q_i and q_j, distance r_{ij}, and effective dielectric constant ϵ_1. These parameters are obtained using experiments and quantum mechanical calculations.

To run an MD simulation, initial atomic coordinates and velocities are provided, and a short timestep δt, usually on the order of one femtosecond, is selected. The forces on each atom are calculated each timestep and the atomic positions and velocities are updated. Periodic boundary conditions, temperature, and pressure controls can be applied to represent a specific statistical mechanical ensemble. This process is iterated as long as needed. In order to model ensemble averaged observables, as seen in macroscopic experiments, the microscopic system in the simulation must be run for sufficiently long times, as stated by the Ergodic hypothesis

$$\langle a \rangle = \lim_{T \to \infty} \frac{1}{T} \int_0^T a(t)dt \equiv \bar{a} \tag{1.3}$$

where $\langle ... \rangle$ represents an ensemble-average and the overbar represents the time-average of observable a.

Various MD software has been designed to run efficiently on modern computers, such as NAMD[10] and Amber,[11] to name a few. The use of supercomputers at national research centers allow for even greater capabilities with regard to MD simulations of ever-larger system sizes and long simulation times. The work presented in Chapters 2–4 use MD simulations to study various biophysical properties of voltage-gated ion channels and the diffusion of membrane proteins.

1.2 Diffusion processes

1.2.1 Normal Brownian motion

In 1827, Robert Brown observed irregular movement of small pollen grains under a microscope.[12] It was not until 1855, when Adolf Fick came up with the diffusion equation $\frac{\partial \varphi}{\partial t} = D\nabla^2 \varphi$, where D is the diffusion constant and ∇^2 is the Laplacian operator, that one could predict the effect of diffusion on the concentration φ.[13,14] Albert Einstein in 1906 presented his approach linking the diffusion problem to a random walk in his treatises on Brownian motion,[15] a name he coined. This presented a microscopic approach to diffusion driven by molecular collisions. He derived the equation for the probability density function (PDF), or propagator, of the random walker's position

$$P(\mathbf{r}, t) = \frac{1}{(4\pi Dt)^{d/2}} \exp\left(\frac{\mathbf{r}^2}{4Dt}\right) \tag{1.4}$$

with diffusion constant D in d dimensions, which is a Gaussian function with a first moment $\langle \mathbf{r}(t) \rangle = 0$ and second moment $\langle \mathbf{r}^2(t) \rangle = 2dDt$. Shortly after, in 1908, these findings were verified experimentally by Jean Baptiste Perrin in his measurement of Avogadro's constant.[16]

1.2.2 Classification of diffusion as normal or anomalous

The molecular details of the surrounding environment can often affect the movement of the particle of interest. A useful quantity for describing diffusion is the mean squared displacement (MSD), or second moment, of the tracked particle:

$$\langle \mathbf{r}^2(t) \rangle = \frac{1}{N} \sum_{n=1}^{N} \left(\mathbf{r}_n(t) - \mathbf{r}_n(0)\right)^2 = 2dDt \tag{1.5}$$

where N is the number of particles averaged over, d is the dimensionality of the diffusion, and D is the diffusion constant.

The classification of the diffusion can be assessed through the dependence of time on the MSD. A linear dependence, as in Equation 1.5, represents normal Brownian motion. However, when the MSD deviates from this linear behavior and instead follows a power-law relation in time, the diffusion is anomalous:

$$\langle \mathbf{r}^2(t) \rangle \sim t^\alpha \tag{1.5}$$

For an exponent (α) greater than 1, the process is superdiffusive. This is seen, for example, in particles experiencing ballistic diffusion that scales as $\langle \mathbf{r}^2(t) \rangle \sim t^2$. In biological systems, superdiffusion can be caused by strong cytoplasmic flows[17] and active transport by molecular motors.[18,19]

On the other hand, the crowded molecular environments of many biological systems lead to a MDS that scales sublinearly with time, with an exponent α between 0 and 1. This behavior is called subdiffusion, and has been observed in a variety of different systems including: telomeres traversing the nucleus of mammalian cells,[20] chromosomal loci moving within the cytoplasm,[21,22] ion channels in the cell membrane,[23] insulin granules moving along microtubules,[24] lipid molecules within membranes,[25,26] amorphous semiconductors,[27] weak turbulence in liquid crystals,[28] and others. Figure 1.1 shows the time-dependent behavior of the MSD for the different types of motion described above.
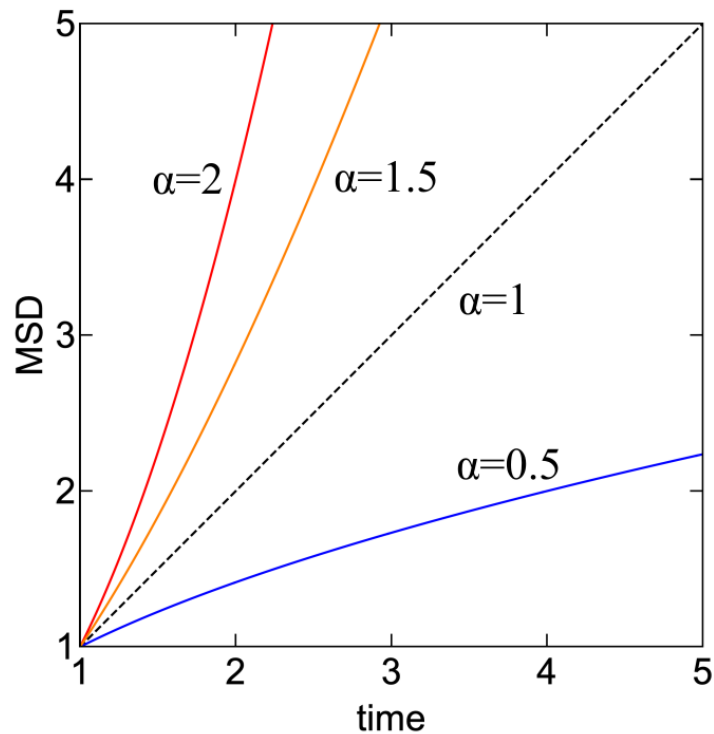
Figure 1.1. A representation of the MSD for the various types of diffusion. Ballistic diffusion is shown in red with $\alpha = 2$, superdiffusion ($\alpha > 1$) is shown in orange with $\alpha = 1.5$, normal Brownian motion is shown in black with $\alpha = 1$, and subdiffusion ($\alpha < 1$) is shown in blue with $\alpha = 0.5$.

1.2.3 Types of subdiffusion

Even within this regime of subdiffusive behavior, there exist several distinct processes that give rise to the anomalous diffusion. These can include trapping events or transient binding, molecular crowding within a viscoelastic environment, or the presence of an underlying fractal geometry. As such, several mathematical models have been developed to describe the diffusion of the particles experiencing one or more of these processes. The three main models that are considered are the continuous-time random walk (CTRW),[27] fractional Brownian motion (FBM),[29] and random walk on a fractal (RWF).[30]
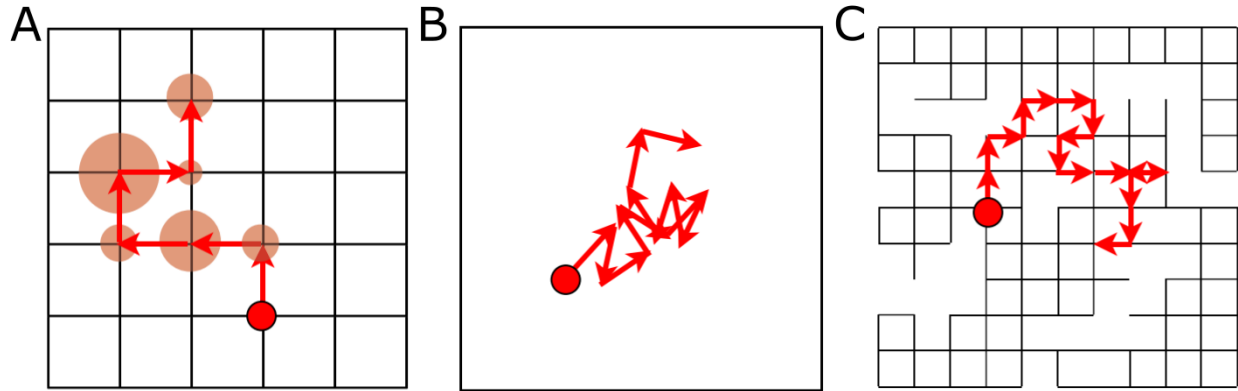
Figure 1.2. Representations of the three primary models of subdiffusion. (A) A CTRW process with trapping where the size of the circle represents the different waiting times. (B) A FBM process with negatively correlated steps. (C) A random walk on a percolation cluster. Adapted with permission from Reference (31).

In the CTRW model, a particle experiences differing waiting times at each step, while the steps are still uncorrelated as in a normal random walk (RW). These waiting times have a heavy-tailed power-law distribution with an infinite mean. This leads to an interesting characteristic called aging. Unlike for a normal RW, where the frequency of steps taken is constant, for a CTRW, the rate of steps decays as $\sim t^{\alpha-1}$. As a result, the system seems to be slowing down with time, eventually sampling longer and longer waiting times until the system comes to a complete stop. The increments in a CTRW are non-stationary and the process is nonergodic. The MSD averaged temporally for a CTRW gives $\overline{\delta^2(t)} \sim t$, while the ensemble-averaged MSD goes as Equation 1.5. A representation of a CTRW process is shown in Figure 1.2A.

The FBM model describes a particle moving within a viscoelastic medium, where a reactionary force is introduced by the local environment. This can be represented by the generalized Langevin equation (GLE)

$$m\dot{v} = -\gamma \int_0^t \Gamma(t - t')v(t')dt' + f + \xi(t) \tag{1.5}$$

where the correlations, or memory, of the viscoelastic environment can be represented by a power law memory kernel $\Gamma(t) \propto t^{-\beta}$ and a Gaussian noise $\xi(t)$. This process has a Gaussian propagator with stationary increments and is ergodic. The MSD takes the form $\langle \mathbf{r}^2(t) \rangle \sim t^{2H}$, where $H \in (0,1)$ is the Hurst exponent. A representation of a FBM process is shown in Figure 1.2B.

The RWF model describes a particle traversing a labyrinthine environment due to crowding of biomolecular objects. As such, it can reach "dead ends" along its path for which it has to retrace its steps. This is often represented with a percolation cluster, as shown in Figure 1.2C. The sublinear MSD is due to the strong anti-persistence of the random walk, with anticorrelated steps. This process is typically ergodic and the PDF for a random walk on a percolation cluster has been shown to be non-Gaussian.[30]

More complex mixed models have been studied using subordination schemes and an assortment of statistical analyses have been developed to classify the different types of subdiffusion.[31] The work presented in Chapters 4 and 5 analyzes trajectories from MD simulations and single-particle tracking experiments to elucidate the subdiffusion mechanism for various membrane proteins.

1.3 Bibliography

1. Swope, W. C., Andersen, H. C., Berens, P. H. & Wilson, K. R. A computer simulation method for the calculation of equilibrium constants for the formation of physical clusters of molecules: Application to small water clusters. *J. Chem. Phys.* 76, 637–649 (1982).

2. Alder, B. J. & Wainwright, T. E. Phase Transition for a Hard Sphere System. *J. Chem. Phys.* 27, 1208–1209 (1957).

3. Alder, B. J. & Wainwright, T. E. Studies in Molecular Dynamics. I. General Method. *J. Chem. Phys.* 31, 459–466 (1959).

4. Rahman, A. Correlations in the Motion of Atoms in Liquid Argon. *Phys. Rev.* 136, A405–A411 (1964).

5. Verlet, L. Computer 'Experiments' on Classical Fluids. I. Thermodynamical Properties of Lennard-Jones Molecules. *Phys. Rev.* 159, 98–103 (1967).

6. Rahman, A. & Stillinger, F. H. Molecular Dynamics Study of Liquid Water. *J. Chem. Phys.* 55, 3336–3359 (1971).

7. Stillinger, F. H. & Rahman, A. Improved simulation of liquid water by molecular dynamics. *J. Chem. Phys.* 60, 1545–1557 (1974).

8. McCammon, J. A., Gelin, B. R. & Karplus, M. Dynamics of folded proteins. *Nature* 267, 585–590 (1977).

9. MacKerell, A. D. *et al.* All-Atom Empirical Potential for Molecular Modeling and Dynamics Studies of Proteins †. *J. Phys. Chem. B* 102, 3586–3616 (1998).

10. Phillips, J. C. *et al.* Scalable molecular dynamics with NAMD. *J. Comput. Chem.* 26, 1781–802 (2005).

11. Case, D. A. *et al.* The Amber biomolecular simulation programs. *J. Comput. Chem.* 26, 1668–1688 (2005).

12. Brown, R. XXVII. A brief account of microscopical observations made in the months of June, July and August 1827, on the particles contained in the pollen of plants; and on the general existence of active molecules in organic and inorganic bodies. *Philos. Mag.* 4, 161–173 (1828).

13. Fick, A. V. On liquid diffusion. *London, Edinburgh, Dublin Philos. Mag. J. Sci.* 10, 30–39 (1855).

14. Fick, A. Ueber Diffusion. *Ann. der Phys. und Chemie* 170, 59–86 (1855).

15. Einstein, A. Zur Theorie der Brownschen Bewegung. *Ann. Phys*. 324, 371–381 (1906).

16. Perrin, J. B. J. Perrin, Comptes Rendus (Paris) 146 (1908) 967. *Comptes Rendus (Paris)* 149, 967 (1908).

17. Reverey, J. F. *et al*. Superdiffusion dominates intracellular particle motion in the supercrowded cytoplasm of pathogenic Acanthamoeba castellanii. *Sci. Rep*. 5, 11690 (2015).

18. Kahana, A., Kenan, G., Feingold, M., Elbaum, M. & Granek, R. Active transport on disordered microtubule networks: The generalized random velocity model. *Phys. Rev. E* 78, 051912 (2008).

19. Bruno, L., Levi, V., Brunstein, M. & Despósito, M. A. Transition to superdiffusive behavior in intracellular actin-based transport mediated by molecular motors. *Phys. Rev. E* 80, 011912 (2009).

20. Bronstein, I. *et al*. Transient Anomalous Diffusion of Telomeres in the Nucleus of Mammalian Cells. *Phys. Rev. Lett*. 103, 018102 (2009).

21. Weber, S. C., Spakowitz, A. J. & Theriot, J. A. Bacterial Chromosomal Loci Move Subdiffusively through a Viscoelastic Cytoplasm. *Phys. Rev. Lett*. 104, 238102 (2010).

22. Di Pierro, M., Potoyan, D. A., Wolynes, P. G. & Onuchic, J. N. Anomalous diffusion, spatial coherence, and viscoelasticity from the energy landscape of human chromosomes. *Proc. Natl. Acad. Sci. U. S. A*. 115, 7753–7758 (2018).

23. Weigel, A. V., Simon, B., Tamkun, M. M. & Krapf, D. Ergodic and nonergodic processes coexist in the plasma membrane as observed by single-molecule tracking. *Proc. Natl. Acad. Sci. U. S. A*. 108, 6438–6443 (2011).

24. Tabei, S. M. A. *et al*. Intracellular transport of insulin granules is a subordinated random walk. *Proc. Natl. Acad. Sci. U. S. A*. 110, 4911–4916 (2013).

25. Flenner, E., Das, J., Rheinstädter, M. C. & Kosztin, I. Subdiffusion and lateral diffusion coefficient of lipid atoms and molecules in phospholipid bilayers. *Phys. Rev. E* 79, 011907 (2009).

26. Jeon, J.-H., Monne, H. M.-S., Javanainen, M. & Metzler, R. Anomalous Diffusion of Phospholipids and Cholesterols in a Lipid Bilayer and its Origins. *Phys. Rev. Lett*. 109, 188103 (2012).

27. Scher, H. & Montroll, E. W. Anomalous transit-time dispersion in amorphous solids. *Phys. Rev. B* 12, 2455–2477 (1975).

28. Silvestri, L., Fronzoni, L., Grigolini, P. & Allegrini, P. Event-Driven Power-Law Relaxation in Weak Turbulence. *Phys. Rev. Lett*. 102, 014502 (2009).

29. Mandelbrot, B. B. & Van Ness, J. W. Fractional Brownian Motions, Fractional Noises and Applications. *SIAM Rev.* 10, 422–437 (1968).

30. Havlin, S. & Ben-Avraham, D. Diffusion in disordered media. *Adv. Phys*. 51, 187–292 (2002).

31. Meroz, Y. & Sokolov, I. M. A toolbox for determining subdiffusive mechanisms. *Phys. Rep*. 573, 1–29 (2015).

Chapter 2

Open-state model of human Hv1 from microsecond simulation

2.1 Background

The voltage-gated proton channel (Hv1) is a membrane protein whose primary function is to modulate acid extrusion from cells.[1] It has been observed in many different types of cells and involved in a wide range of biological processes, including pH regulation and immune response. In neutrophils, Hv1 activity is required for optimal reactive oxygen species (ROS) production by the NADPH oxidase during oxidative bursts.[2–4] In B lymphocytes, activation of the Hv1 channel enhances the B-cell antigen receptor-mediated intracellular signaling cascade that leads to B-cell proliferation and differentiation.[5] In basophils, Hv1 has been proposed to play an important role in the stimulation of histamine release via an NADPH oxidase-independent mechanism.[6] In mature human spermatozoa, Hv1 acts as a flagellar regulator of intracellular pH, promoting sperm capacitation.[7,8] In the respiratory system, Hv1 is involved in the pH homeostasis of the airway surface liquid, by contributing to acid extrusion from the airway epithelium.[9] Hv1 is also preferentially expressed in several types of cancers, such as B-cell malignancies,[5,10] and breast and colorectal cancers.[11–13] Excessive Hv1 activity was found to increase the metastatic potential of cancer cells.[10,12] Hv1 has been found in brain microglia where it is required for NADPH oxidase-dependent ROS production and, consequently, enables brain damage after ischemic stroke.[14] Such an extensive list of associated maladies makes this an interesting system to study as a

pharmaceutical target, increasing the importance of having accurate structural data and an understanding of the activation mechanism.

The Hv1 voltage-gated proton channel is similar to other voltage-sensitive ion channels, including potassium, sodium, and calcium channels, which contain voltage-sensing domains (VSD).[15] However, in contrast to voltage-sensitive metal ion channels, Hv1 does not possess a separate pore domain.[16,17] The VSD in Hv1 consists of four transmembrane helical segments (S1-S4) as well as a S0 helix at the N-terminus and a coiled-coil region at the C-terminus. The functional unit of Hv1 is a homodimer, but truncations of the C-terminal helix result in functional monomer units.[18] The Hv1 monomer has two primary functions: it gates the proton current and also serves as the conduction pathway.[19]

As with other VSD containing proteins, the voltage-sensitivity of Hv1 is conferred by the S4 helix, which moves in the membrane in response to changes in the transmembrane (TM) potential.[20] The S4 helix contains three conserved triplet repeats composed of an arginine, followed by two hydrophobic residues. These arginine residue side-chains interact with acidic residues on the neighboring S1-S3 helices forming an internal salt-bridge network. These salt-bridges are exchanged between the acidic residues on S1-S3 during the movement of S4 and subsequent activation of the channel.[21]

Currently, our structural knowledge of Hv1 consists of a crystal structure of a chimeric mouse Hv1 (mHv1cc) that was solved to 3.45 Å resolution by Takeshita *et al*.[22] This structure provides a putative model for the resting and closed state of the channel with the S4 helix in the "down" position. However, the reported structure is in a non-physiological trimer and does not provide any direct information on the open-state nor the interface between Hv1 subunits. Several models of the

open-state Hv1 generated using molecular dynamics (MD) simulations with applied restraints have been reported.[23–27] We present an open-state model that was generated from microsecond-long MD simulations under potential that replicate physiological conditions without any artificial restraints.

As a result of our simulations, we generated equilibrated membrane-embedded structures for an unpolarized VSD which displays structural differences with the reported mHv1cc crystal structure, a hyperpolarized closed-state, and a depolarized open-state. We observed the dynamics of the transition between the closed and open-states of Hv1 in atomic-level detail. The generated models agree with available experimental data, including electrophysiology measurements, mutant-cycle analysis, and ligand binding experiments.

2.2 Methods

2.2.1 Model construction

The initial configuration of the hHv1 monomer resting state was generated by homology modeling through comparison with the mmHv1cc crystal structure [PDB ID code 3WKV] and the alignment presented by Takeshita *et al*.[22] The missing loops between the transmembrane segments were constructed using Phyre2 web-server for homology modeling.[28] The S4 segment was truncated at E227 as it has been shown that truncating the coiled-coil segment from the C-terminus results in the formation of functional monomeric channels.[19,29] The final hHv1 construct was composed of residues F88 to R230. This protein was inserted into a POPC bilayer consisting of 174 lipid molecules, allowing the putative S0 helix (residues F88-S97) to be in the phosphate headgroup region of the bilayer and unburying the shortest extracellular loop between S1 and S2. Using

CHARMM-GUI,[30] the system was solvated with 10,788 TIP3P water molecules, and 150 mM

NaCl (34 Na^+ and 38 Cl^-) for a total of 58,241 atoms.

2.2.2 Molecular dynamics simulations

The system was equilibrated using all-atom molecular dynamics (MD) simulations. These were

performed with the NAMD version 2.9 software[31] using the CHARMM-27 and CHARMM-36

force-fields[32–35] for proteins and lipids, respectively, and the TIP3P water model.[36] After 5000

steps of minimization with all protein atoms constrained, we ran the system for 100 ps at a constant

temperature of 300 K, and constant volume in a tetragonal cell ($81.5 \times 81.5 \times 88.3$ Å^3) with periodic

boundary conditions, allowing the lipid molecules to relax. The system was then equilibrated for

5 ns in the NPT ensemble, at a pressure of 1 bar and a temperature of 300 K with the protein

backbone atoms restrained harmonically to their initial positions and slowly released over an

additional 10 ns using a decreasing force constant of 50, 25, 10, 5, and 2 kcal mol^{-1}Å^{-1}. After the

backbone was completely released, we ran the system for 10 ns without any restraints.

2.2.3 Microsecond timescale simulation details

After several nanoseconds of equilibration, the system was transferred to Anton, a special-purpose

computer for molecular dynamics simulations of biomolecules,[37] and simulated for 34

microseconds. Anton software version 2.12.4 was used. Specific simulation parameters were the

same as those reported previously.[38] Briefly, an r-RESPA algorithm[39] was employed to integrate

the equations of motion with a time step of 6 fs for the long-range non-bonded forces, and 2 fs for

short-range non-bonded and bonded forces. The k-Gaussian split Ewald method[40] was used for

long-range electrostatic interactions. All bond length involving hydrogen atoms were constrained

using SHAKE.[41] The simulations were performed at a constant temperature of 300 K and a pressure of 1 atm, using Nose-Hoover chain thermostat[42] and the Martyna-Tobias-Klein barostat.[43] The RESPA algorithm and the temperature and pressure controls were implemented using the multigrator scheme.[44] The system was simulated under these conditions for 7.3 μs. Following this, the system was subjected to a hyperpolarizing potential of -140 mV (i.e. the potential was negative on the intracellular side of the membrane relative to the extracellular side) for 4 μs. This was achieved by applying a constant electric field in the direction normal to the membrane surface as described previously.[45] The system was then subjected to a depolarizing potential of +140 mV for an additional 24 μs.

2.2.4 Docking of 2GBI

The docking calculations were performed using a Monte Carlo simulated annealing method implemented in the AutoDock Vina software package.[46] Twenty protein configurations were selected from clustered configurations of the four internal residues in hHv1 that represent the binding-site near the center of the pore (D112, R211, F150, S181) from the last ~10 μs of the trajectory under depolarizing potential, in which S4 was in the "up" position. The clustering analysis was performed using VMD[47] with a root-mean-square deviation (RMSD) cutoff of 2.0 Å for non-hydrogen atoms in these four residues. The centroid structure from each cluster was selected as the target for rigid docking of the 2-guanidinobenzimidazole (2GBI) ligand. Twenty docking poses for 2GBI were generated by AutoDock Vina within the search space confined to a cuboid of dimensions $33 \times 33 \times 24$ Å^3 in the intracellular vestibule of the pore. The 400 poses were clustered with a 1.0 Å RMSD cutoff for non-hydrogen atoms of 2GBI.

An identical docking simulation was performed on the closed-state using the ~4 μs trajectory of hHv1 with a hyperpolarizing potential. The binding-site for the closed-state clustering was chosen to be the four residues: D112, R205, F150, S181.

2.3 Results

2.3.1 Equilibrated structure of Hv1 in a membrane

We constructed a model of the human Hv1 (hHv1) channel using the mHv1cc crystal structure as a template as outlined in Section 2.2.1. The model consisted of one monomeric hHv1 in a hydrated POPC lipid bilayer with approximately 150 mM NaCl. This system was equilibrated under zero transmembrane potential ($\Delta V=0$ mV; unpolarized) for approximately 7.3 μs of all-atom MD. During this unpolarized simulation, the intracellular vestibule widened and the water density inside the pore increased. Within the bilayer, the S3 helix moved upwards, towards the extracellular side of the membrane, by approximately one helical turn. Additionally, the S2 helix tilted outwards causing the space between the intracellular ends of S1 and S2 to widen, while the extracellular ends of S2 and S3 also moved apart. Likewise, the space between the intracellular ends of the S3 and S4 helices widened.

Within the pore of the unpolarized structure, we observed a network of internal salt-bridges. These formed between the three basic arginine residues on the S4 helix and acidic residues on the S1-S3 helices. The uppermost arginine on S4 with respect to the extracellular side, R205 (R1), forms a consistent salt-bridge with D112 on the S1 helix in the down-state. It is proposed that D112 in the center of S1 is the key residue for the selectivity filter of the channel.[48] The other prominent salt-bridges in the down-state consist of R208 (R2) with E153 on the S2 helix and R211 (R3) with D174 on S3.
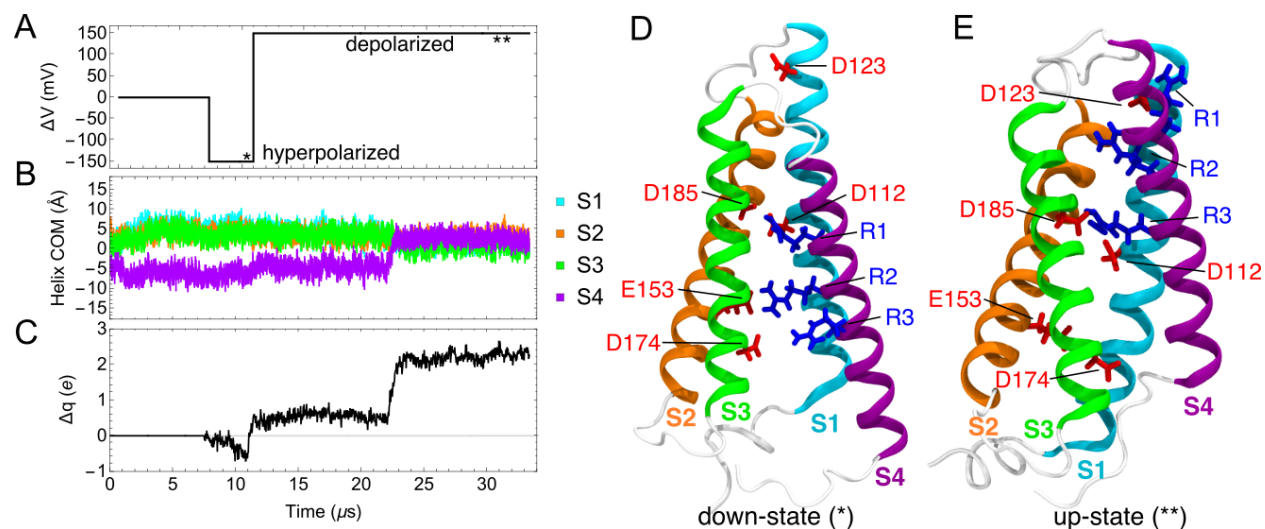
Figure 2.1: MD simulation of the human Hv1 in a hydrated lipid bilayer. (A) TM potential profile during the 33 μs simulation. (A) Time evolution of the centers-of-mass of the four TM helices. The VSD maintains its down-state conformation during 7.3 μs at ΔV = 0 mV and 4 μs of hyperpolarizing potential (ΔV = -150 mV). At 11 μs, shortly after the membrane is depolarized, the S4 Args move up "one click"; at 22 μs there is an additional "two click" upward motion of the S4 helix. (C) Total charge displacement in the membrane electric field. (D) Snapshot of the Hv1 VSD in the down-state at 11 μs and (E) the up-state at 24 μs. The conserved Arg side-chains on S4 (R1–R3) are drawn in blue and the conserved acidic side chains on S1–S3 are in red. The conformational change between the down- and up-states involves primarily an 8 Å upwards motion of the S4 helix and a change in in the S1–S4 orientation.

2.3.2 Simulations under transmembrane potential

The system was subjected to two of TM potentials similar to those experienced under physiological conditions. The first was a hyperpolarizing potential of -140 mV (i.e. the potential was negative on the intracellular side relative to the extracellular side) for 4 μs. The trajectory length and applied potential is shown in Figure 2.1A.

Under the hyperpolarizing potential, the S4 helix moved closer to the intracellular side of the channel, while the other three helices remained fairly stationary, as seen in Figure 2.1B. This led to a shifting of the lower internal salt-bridges. R3 broke away from its interaction with D174 and started contacting the lipid phosphate head groups in the lower membrane. Likewise, R2

maintained its salt-bridge with E153 until moving down to D174 at simulation time 9.5 μs. Following this transition, R1 began interacting with the now free E153. However, the R1 to D112 salt-bridge remained consistent with the unpolarized structure and the S4 helix remained in the down-position.

In order to simulate the activation of the channel, the system was subjected to a depolarizing potential of +140 mV for 24 μs. Soon after the initial depolarization, the three arginine residues moved upwards one-click towards the extracellular side as seen by the jump in charge displacement at approximately 12 μs in Figure 2.1C. At approximately 22 μs, the three arginine residues quickly move two additional clicks upwards pulling the entire S4 helix upwards by approximately 8 Å. This movement accompanied a rapid shift in the internal salt-bridges, in which all three arginine residues began to interact with residues closer to the extracellular side, akin to climbing up a ladder of the acidic residues on S1-S3.

This new configuration of Hv1 with S4 in the upward position remained stable under the depolarizing potential for the remaining 12 μs. During this time, R3 formed new salt-bridges with D112 and D185. Both R2 and R1 were reaching up to the extracellular region of the protein interacting with E192/E119, and D123, respectively. This new orientation of charged residues inside the channel led to an increase of water density in the pore as seen in Figure 2.2. Additionally, there was a widening of the central pore radius, as well as an increase in the probability that a hydrogen-bond chain (HBC) spans the entire channel.
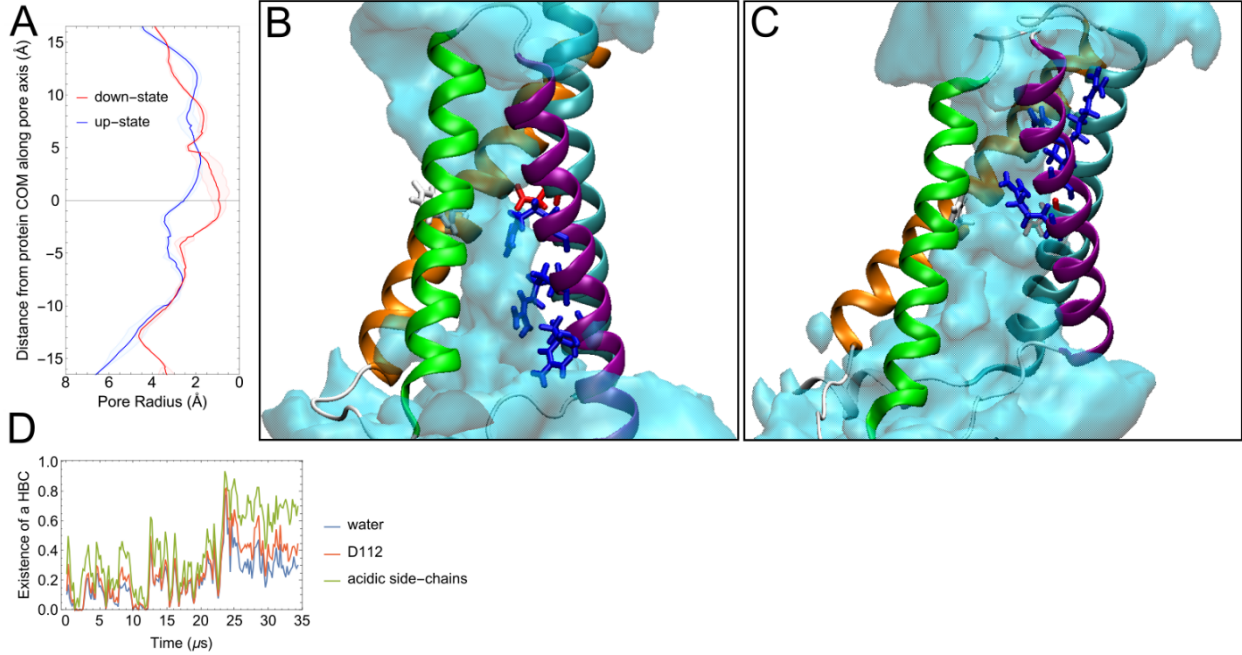
Figure 2.2. Pore water profiles for the down-state and up-state. (A) Plots of the pore radius averaged over 100 frames taken at 25 ns intervals from the end of the hyperpolarized trajectory (down-state) and depolarized trajectory (up-state). The pore radius along the transmembrane axis shows a central constriction site at the center of the pore. (B) Snapshot of the channel in the down-state and (C) up-state with the water density shown in light blue at an isovalue of 0.033 Å^{-3}, the number density of bulk water. (D) The probability of the existence of a hydrogen-bonded chain (HBC) spanning the channel. Each frame was given a binary value of 0 if there was no HBC or 1 if there was at least one HBC. A hydrogen-bond was defined as an O-H cutoff distance of 3.5 Å and an O-H-O angle of less than 40 degrees. The trajectory was averaged over every 50 frames.

2.3.3 Calculated gating charge shows movement of S4 helix

The gating charge is a measure of the net charge on the protein that moves through the membrane electric field during the transition from the resting-state to the activated-state. It can be calculated on a per-residue basis using the equation:

$$Q_i = \left\langle \sum_j q_{ij} \Phi_{mp}[z_j] \right\rangle_{up} - \left\langle \sum_j q_{ij} \Phi_{mp}[z_j] \right\rangle_{down} \tag{1}$$

20

Where q_{ij} is the partial charge of atom j on residue i and Φ_{mp} is the membrane potential at position z_j along the transmembrane direction. The potential at each atomic position was calculated using linearized Poisson-Boltzmann theory as described previously.[49,50] This quantity was averaged from an ensemble of 800 configurations taken at constant intervals for the equilibrated up- and down-states from the hyperpolarizing and depolarizing simulations, respectively. The cumulative contributions to the total charge displacement from each residue are shown in Figure 2.3. The computed gating charge for the transition from the closed-state channel to open-state is 2.7e, with the largest contributions coming from the movement of the three arginine residues on S4. This result compares favorably with electrophysiological measurements of 2.0e for monomeric mHv1,[51] between 1.6-2.7e estimated from monomeric Ci-Hv1,[52] and 3e in hHv1.[53]
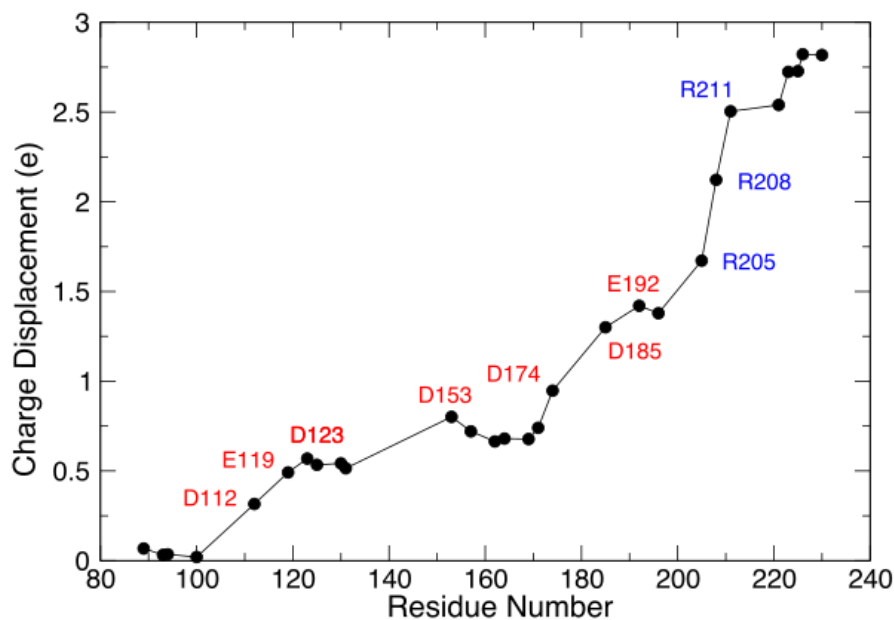
Figure 2.3. Calculated gating charge for hHv1. The gating charge is the cumulative charge displacement within the membrane electric field moving from the down-state to the up-state. The total gating charge magnitude is about 2.7e, with the three arginine residues contributing largely to this total.

2.3.4 Docking calculations of 2GBI

The ligand 2-guanidinobenzimidazole (2GBI) has been shown to inhibit proton conduction in Hv1.[54] It binds within the intracellular side of the selectivity filter region of the open-state channel. The proposed binding site from mutagenesis experiments places the aromatic ring of the benzimidazole moiety of 2GBI near the F150 side chain and the basic guanidine group near D112.
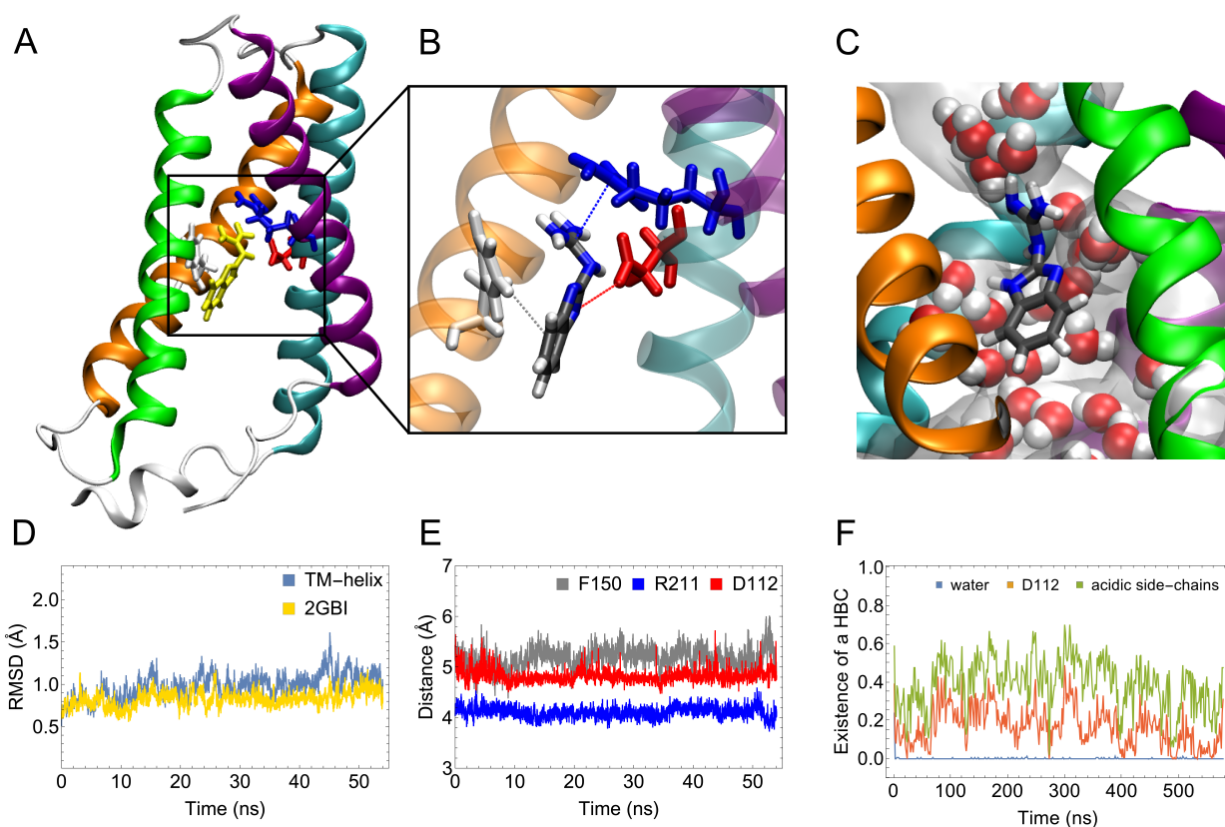
Figure 2.4. Binding of the Hv1 inhibitor, 2GBI, and MD equilibration. (A) The side-view showing the equilibrated binding mode for 2GBI (yellow) and the interacting residues. (B) A close-up of the interactions between 2GBI and R211, D112, and F150. (C) A simulation snapshot of 2GBI blocking the formation of a continuous water-wire. (D) The Cα RMSD over the 54 ns trajectory of one of the selected docking poses. (E) The atomic distances between 2GBI and the selected residues measured as a function of the simulation time. The 2GBI-F150 distance is measured from the center of the benzyl rings, 2GBI-R211 distance is measured from the carbon atoms of the guanidine groups, and the 2GBI-D112 distance is measured from the imidazole nitrogen on 2GBI to the nearest D112 carboxyl oxygen. (F) The probability of the existence of a hydrogen-bonded chain (HBC) spanning the channel. Each frame was given a binary value of 0 if there was no HBC or 1 if there was at least one HBC. A hydrogen-bond was defined as an O-H cutoff distance of 3.5 Å and an O-H-O angle of less than 40 degrees. The trajectory was averaged over every 15 ps.

We performed docking simulations of the 2GBI ligand with our equilibrated up-state model. The four residues chosen to represent the binding site were R211 (R3), D112, F150, and S181. The configurations of these residues from the depolarized simulation were clustered based on an RMSD value than 1 Å. The twenty most populated conformations were used to perform the docking calculations. The resulting docked 2GBI configurations were also clustered based on RMSD. The up-state model showed favorable binding of 2GBI with the aromatic group next to F150 and the guanidine group pointed between D112 and R211, as seen in Figure 2.4A. The ligand is positioned directly below the selectivity filter and effectively blocks the formation of a hydrogen bonded water-wire through the open channel (Figure 2.4C). Further MD of the centroid 2GBI conformation placed in the proposed binding site showed that this position was stable over a 55 ns simulation with a RMSD around 1.0 Å for both the ligand heavy-atoms and protein helix backbone as shown in Figure 2.4D. Three of the proposed binding-site residues had continuous contact with 2GBI as shown in Figure 2.4E. The probability of a continuous HBC spanning the channel is completely eliminated for the waters within the pore, and possible HBCs involving acidic residue side-chains are reduced (Figure 2.4F).

A similar docking calculation on the equilibrated down-state of Hv1 revealed that the orientation of the selected residues does not allow the 2GBI to choose a favorable binding conformation near the selectivity filter. The most populated cluster of 2GBI configurations placed it pointing parallel to the pore axis with the aromatic group located in the solution of the intracellular vestibule of the channel and the guanidine group pointing towards the selectivity filter, mostly D112.

2.3.5 Internal crosslink inhibits conduction

The use of crosslinks between residues on neighboring subunits can provide information about residue side-chain proximity. This can be achieved using engineered cysteine crosslinks, either through disulfide bond formation or a metal ion-bridges.[55] This second technique better allows the protein to maintain its physiological conformation due to the less-rigid binding of the side-chains to the metal ion, as opposed to disulfide crosslinks that can form artificial constructs due to the strong side-chain binding. In the up-state model of hHv1, the residues V109 and F150 sit facing the pore of the channel on the S1 and S2 helices, respectively. Mutation of these two residues to cysteine and subsequent addition of 2 μM intracellular Cd^{2+} ions inhibits proton conduction by 90% compared to control (Hv1-C107A), as shown in Figure 2.5. The individual mutations show only minor current reductions in the presence of Cd^{2+}, while the double-mutant shows a large reduction, suggesting that these two residues form a Cd-crosslink. Therefore, it is likely that F150 and V109 are in close proximity.

In order to compare with the atomistic model of the up-state, we mutated the F150 and V109 residues to cysteine and performed a restrained MD simulation. An artificial harmonic force was applied to the Cβ atoms on the two cysteines to keep them within 5 Å. This technique for modeling crosslinks has been previously reported to generate atomistic protein models consistent with experiment.[56] After 70 ns with the restraints on the two Cβ atoms, the RMSD of the TM helix Cα atoms compared to the starting up-state structure was approximately 1 Å. This indicates that no large protein backbone movements were required to create this artificial crosslink from the generated up-state model, only a rearrangement of the mutated side-chains. An additional 75 ns of simulation with the restraint removed also did not show large backbone rearrangement, with an RMSD less than 2 Å.
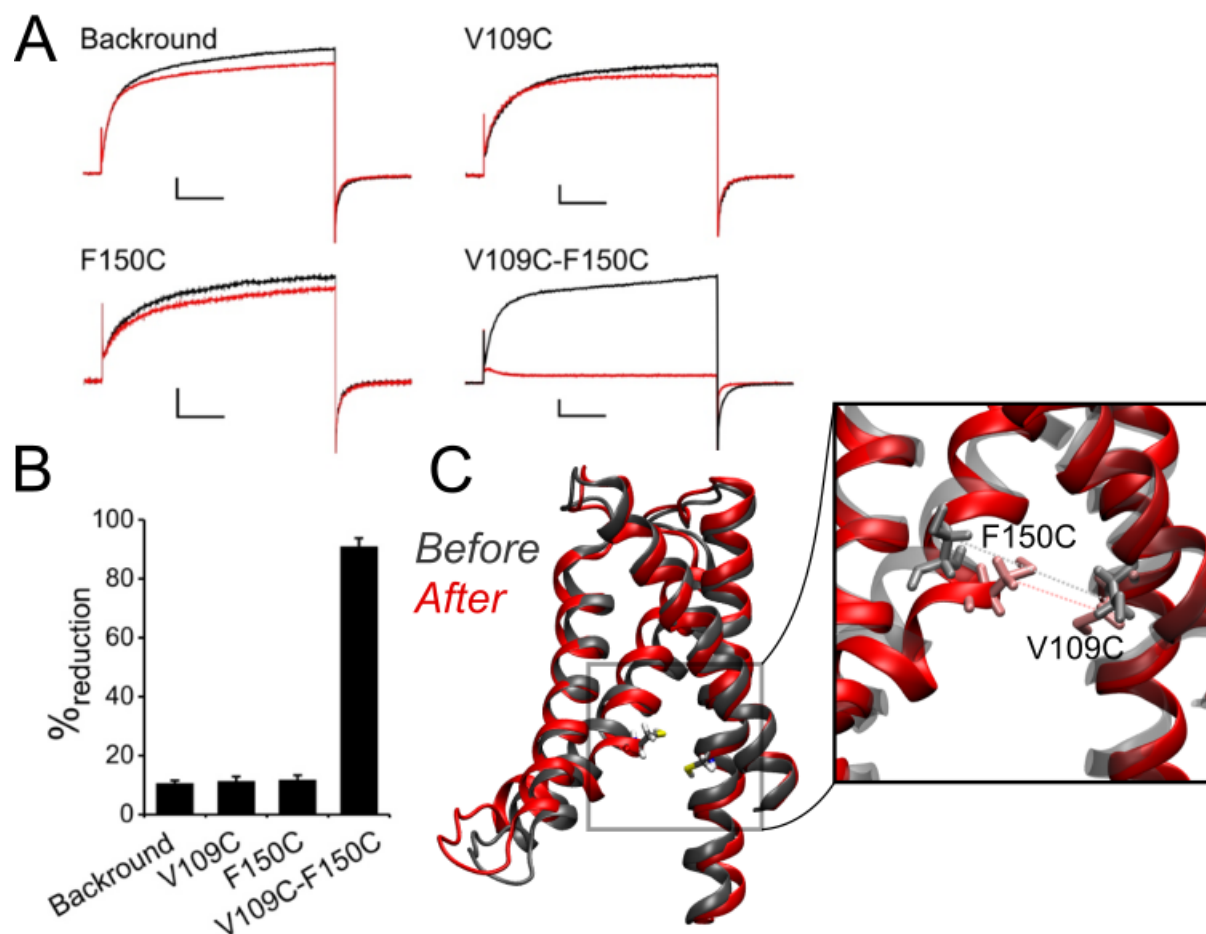
Figure 2.5. (A) Proton currents from the indicated mutants and the reference background (monomeric Hv1-C107A) measured in response to depolarization from -40 mV to +120 mV in the absence (black traces) and presence of 2 μM intracellular Cd^{2+} (red traces). Horizontal scale bars are 0.2 seconds. Vertical scale bars are either 20 pA (V109C, F150C) or 50 pA (Background, V109C-F150C). (B) Average percentage of reduction of current induced by Cd^{2+}. (C) Hv1 VSD after (red) application of a V109C-F150C S-Cd-S restraint, starting with the up-state model generated during the unrestrained Anton simulation (gray). The distance between the two Cβ atoms, to which the restraint force was applied, is shown with dashed lines. The TM helix Cα RMSD of the two structures is ~1 Å.

2.4 Discussion

The microsecond-long simulations of hHv1 under potential provide insight into the mechanism of activation for Hv1 as well as fully atomistic models of equilibrated down- and up-states in a hydrated lipid bilayer. Several key experimental measurements corroborate our simulation models,

including gating charge, mutagenesis analysis of 2GBI inhibition, and metal-ion bridge crosslinking experiments.

2.4.1 Changes in the resting state profile

Over this long simulation timescale, several key changes arise from the starting configuration based on the crystal structure. During the unpolarized simulation, the S3 helix shifts towards the extracellular side by approximately one helical turn compared to the crystal structure, as seen in Figure 2.6A, suggesting that the S3 helix sits higher in the membrane. A similar observation was made using EPR measurements on hHv1 at 0 mV.[57] This lowering of S3 puts V178 in better alignment with F150 to form the hydrophobic gasket. The S4 helix gating charges are straddling this position with the lower two arginine residues, R208 and R211, sitting closer to the intracellular side of the pore, with R205 just above F150. This facilitates interactions between D112 and R205 in the down-state, with R208-E153 and R211-D174 salt-bridges both below the hydrophobic gasket defined by F150 and V178. The second upper hydrophobic gasket seen in the crystal structure does not appear in our unpolarized model, leading to just a single solvent constriction site with low water density.

In a large deviation from the crystal structure, the S2 helix tilts to the side, creating a wider intracellular gap between S1 and S2. Likewise, S4 tilts away from S3, widening the intracellular gap between these two helices. We initially thought this may be due to the unravelling of the C-terminal region of the S4 helix, traditionally defined as the coiled-coil domain, including residues 223-230 that are exposed to intracellular solution. However, running an additional 1 μs of MD simulation with the C-terminus truncated at R223 did not result in any large protein backbone rearrangements, suggesting that this unfolded helix is not the sole cause for the pore widening.
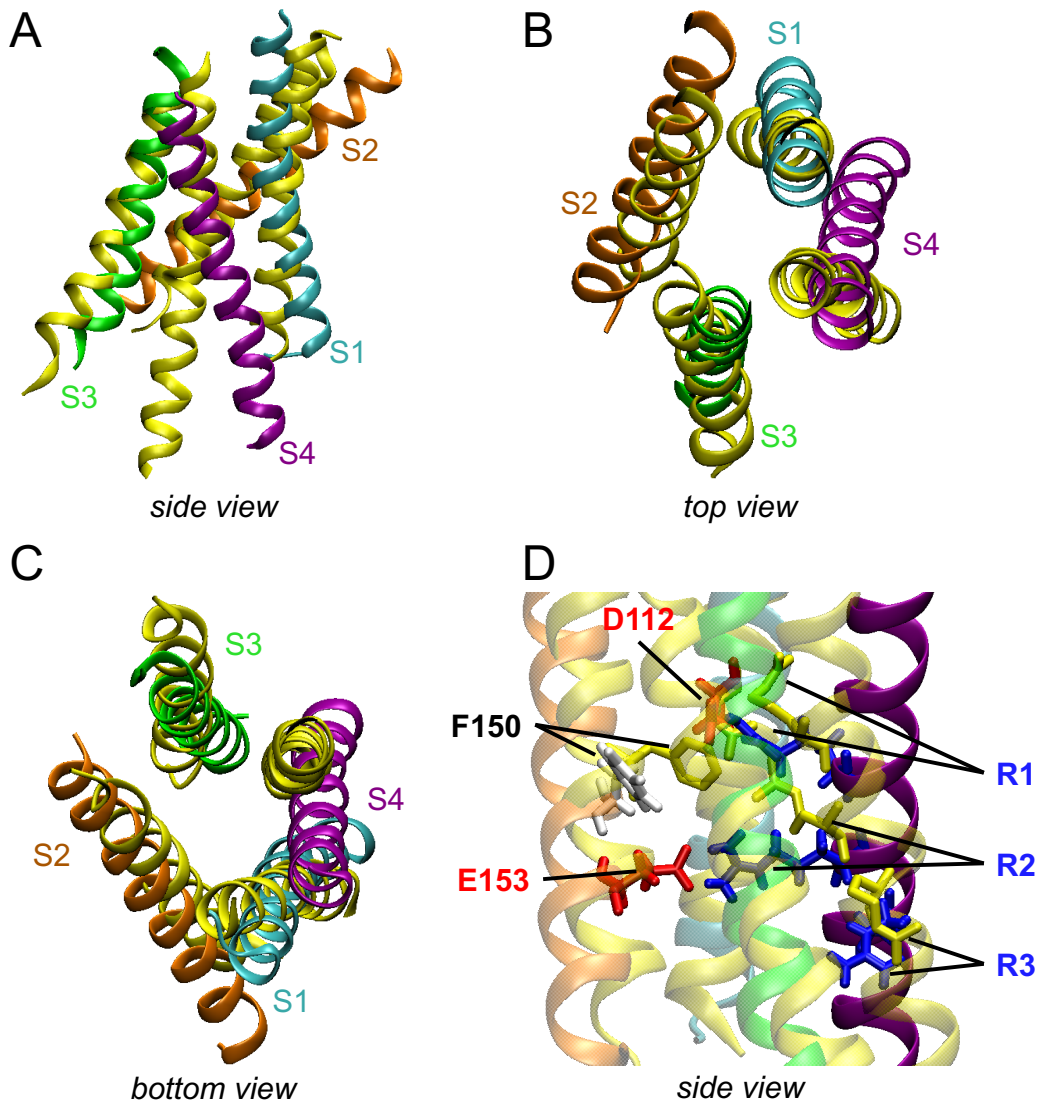
Figure 2.6. Structural alignment of the equilibrated unpolarized Hv1 with the mHv1cc crystal structure. Alignment was performed on the Cα atoms of residues in the S1, S2, and S3 transmembrane helices defined based on the alignment by Takeshita *et al.*[22] The RMSD of the TM helix Cα atoms is 4.34 Å. The crystal structure model is shown in yellow in all panels.

2.4.2 Comparisons with other models

Our model of the up-state differs from previous homology models generated using the structures of metal-cation channel VSDs. In our model, F150 sits at the center of the water constriction site, as shown in Figure 2.7. All three gating-charge arginine residues move above F150, with R211

level with D112 and D185 in the up-state. The positioning of the acidic residues is different from those in both homology models proposed by Wood *et al.*,[23] in which D185 sits higher in the extracellular vestibule while D112 sits just above the intracellular vestibule at the start of the constriction region. This prevents R211 from contacting both D185 and D112 in their R1-Hv1 model, for which the three Hv1 arginine residues are aligned to the first three gating-charges in the Kv1.2-2.1 paddle-chimera structure. Their R2-Hv1 model places R211 much lower so that it only contacts D112, with D185 much higher in the extracellular vestibule.
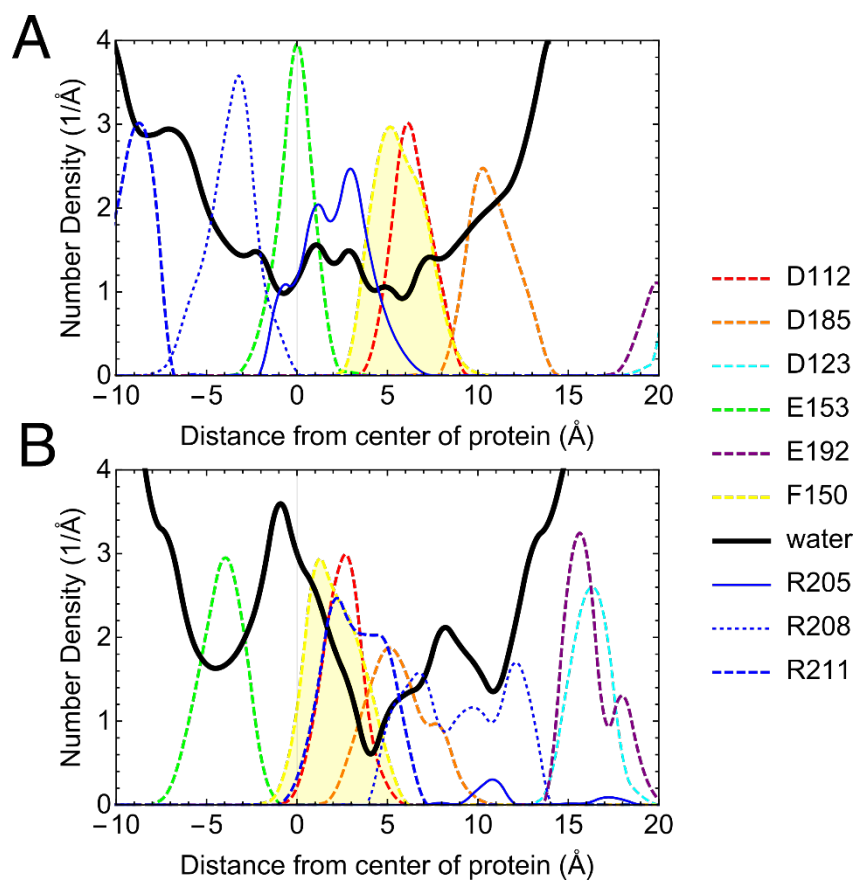
Figure 2.7. Number density of selected residue side-chain atoms and water molecules. (A) The density profiles for the down-state counted over the last 3 μs of the hyperpolarized trajectory. (B) The density profiles for the up-state counted over the last 3 μs of the depolarized trajectory. The bins were 1 Å wide along the TM-axis and the protein was aligned using S1-S3 helix Cα atoms. The profiles were averaged over the number of frames.

Likewise, in the R3D hHv1 homology model developed by Kulleperuma, *et al.*,[24] using the VSDs from KvAP, the paddle-chimera, and NavAb as templates, R211 is in line with D112 located near the center of the pore. In their model, D185 on the S3 helix also sits well within the extracellular vestibule quite far from the D112-R211 salt-bridge. As mentioned previously, a downward shift of the S3 helix in the resting-state models, as suggested by EPR experiments[57] and the mHv1cc crystal structure,[22] would keep D185 closer to D112 and facilitate salt-bridge formation with R211 as we see in our up-state model.

We see salt-bridge contacts in our models similar to those observed by Gianti, *et al.*,[26] who also used the mHv1cc structure as a basis using three different alignments of the three arginine residues on S4 to generate structural ensembles of resting (R), intermediate-resting (IR), and activated states (A). Our unpolarized down-state model resembles their IR-state model, with R205 in contact with D112 and D185 at approximately the same height within the pore. Even the E153-R208 and D174-R211 salt-bridges are observed in both models. When we apply the hyperpolarized potential to the membrane, the arginine residues move down in the pore below F150, resembling their R-state model. R205 is pulled away from D185, leaving the R205-D112 salt-bridge intact.

However, comparing their A-state model with our up-state model, we see a larger translation of the S4 arginine residues. R205 is pulled up into the extracellular vestibule forming a stable salt-bridge with D123 at the top of S1. R208 also reaches upwards in order to form salt-bridges with E119 and E192. This leaves R211 level with D112 and D185 in the pore. This salt-bridge pattern is similar to the open-state homology model proposed by Chamberlin, *et al.*[25] with R211 passing above F150 and the residues they classify as the hydrophobic plug to facilitate interactions with D112 and D185. We do not, however, observe the complete hydrophobic plug that they do in the closed-state with all three arginine residues sitting below this region.

In agreement with mutagenesis analysis from Randolph, *et al.*,[27] R3 in the activated state is in close contact with both D112 and D185.[27] However, their homology models for the resting- and activated-states of Hv1 suggest a larger movement of S4, as much as 14-16 Å, although they report a similar gating charge of 2.5e.

This is in contrast to the Ci-VSD crystal structures captured in the activated- and resting-states by Li, *et al.*,[58] who saw a difference in S4 position of only 5 Å. In their activated state, R3 is in plane with the hydrophobic gasket formed by the conserved F161 (F150 in hHV1). They propose a "one-click" displacement of the gating charges upon translation and rotation of S4. In our model of the up-state, all three arginine residues have moved above F150.

2.4.3 Activation by a three-click mechanism

Upon introduction of a depolarizing potential, R205 moves above F150, signaling the first-click at around 11 µs. R208 also begins interacting with D112. After approximately 22 µs, R205 is the first gating residue to rapidly jump towards the extracellular side in the second-click, leaving R208 alone to interact with D112. For a very brief time, approximately 100 ns, R208 and R211 both interact with D112. R208 then rapidly jumps upwards in the third-click, leaving R211 to interact with D112. During this motion of the three arginine residues, the S4 helix moves upwards in the membrane by approximately 8 Å. Likewise, S4 appears to rotate approximately 75° during the transition. Figure 2.8 highlights the major rotations of the S4 helix, which coincide with the three-steps seen at 11 µs and 22 µs.

In addition to the S4 translation, the second two-clicks are accompanied by increased water content in the pore and a widening of the pore-radius. With the additional water molecules, the probability of water-wire formation through hydrogen bonded chains also increases. This may suggest a more

favorable state for proton conduction through a Grotthuss hopping mechanism, as previously suggested.[23,59,60]
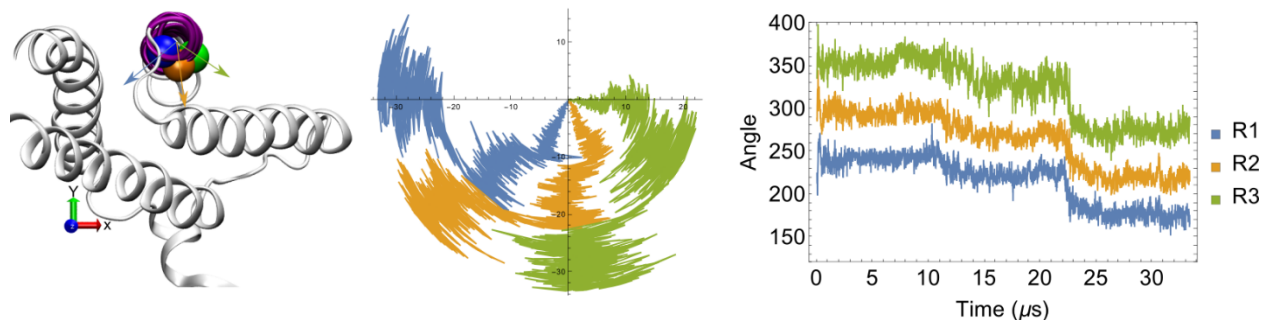
Figure 2.8. Angle of rotation for the S4 helix as it translates upwards in the membrane. The rotation angle was defined for the 2-D vector between the principle axis of the S4 helix backbone atoms and the Cα atoms of R1, R2, and R3 projected on a plane normal to the transmembrane axis. (*Left*) A snapshot showing the S4 helix in purple and the Cα atoms of R1 (blue), R2 (orange), and R3 (green). Each frame of the trajectory was aligned by the S1—S3 transmembrane helices. (*Center*) A radial plot showing the angle with respect to the positive x-axis. The radius from the origin denotes the time of the trajectory. (*Right*) The angle of rotation shown as a function of time indicates an overall rotation of approximately 75° for all three S4 Arginines.

2.4.4 Other structural features

During the unpolarized simulation, a POPC lipid molecule enters the intracellular vestibule between the widening S1-S2 gap from the inner leaflet. The lipid headgroup participates in some polar interactions with residues K94, Q102, R223, and R226 near the intracellular vestibule. The lipid headgroup remains within the intracellular S1-S2 gap during the entire simulation under hyperpolarizing and depolarizing potentials. This flexibility of the S1 helix position may suggest a role in the cooperative activation of the dimer as suggested by Hong, *et al*.[61]

Additionally, the S0 helix (residues 88 to 94), which is believed to act as a membrane anchor,[22] does unfold into a random coil and later refolds during the simulation. However, it always

maintains its position sitting planar within the lipid phosphate groups which supports the hypothesis that it serves to anchor the protein dimer to the membrane.

Lastly, the C-terminal tail of the S4 helix (residues 223 to 230) that is sticking out of the membrane and is exposed to solution becomes disordered. As a loose coil, it moves into plane with the polar headgroups of the bilayer. To check that this structural disorder does not affect the backbone structure of the transmembrane helices, we removed this segment and ran for an additional 1 μs simulation under depolarizing potential. The truncation did not lead to any large structural rearrangements of the transmembrane helices with the backbone RMSD remaining less than 2.5 Å. While this segment would normally be part of the coiled-coil motif responsible for dimerization extending out into the cytosol,[62] it likely does not serve a functional purpose for the monomeric channel.

2.4.5 Concluding remarks

These microsecond-long simulations of hHv1 embedded in a hydrated lipid bilayer provide putative down- and up-state models in the presence of physiological transmembrane potentials. The models agree reasonably well with several experimental measurements, including the monomeric gating charge, 2GBI binding and mutagenesis, and metal-ion bridge crosslinking. These models can provide a basis for further structural refinement using experimental data, including additional crosslinks. They also provide all-atom structures for which explicit modeling of proton transfer can be performed using quantum chemical calculations. Additionally, they can be used as starting structures, or at least a library of structures, for which computational studies of small-ligand binding can be performed.

2.5 Bibliography

1.   Decoursey, T. E. Voltage-gated proton channels and other proton transfer pathways. *Physiol. Rev.* 83, 475–579 (2003).

2.   Okochi, Y., Sasaki, M., Iwasaki, H. & Okamura, Y. Voltage-gated proton channel is expressed on phagosomes. *Biochem. Biophys. Res. Commun.* 382, 274–9 (2009).

3.   Ramsey, I. S., Ruchti, E., Kaczmarek, J. S. & Clapham, D. E. Hv1 proton channels are required for high-level NADPH oxidase-dependent superoxide production during the phagocyte respiratory burst. *Proc. Natl. Acad. Sci. U. S. A.* 106, 7642–7 (2009).

4.   El Chemaly, A., Okochi Y., Sasaki, M., Arnaudeau, S., Okamura, Y. & Demaurex, N. VSOP/Hv1 proton channels sustain calcium entry, neutrophil migration, and superoxide production by limiting cell depolarization and acidification. *J. Exp. Med.* 207, 129–39 (2010).

5.   Capasso, M. *et al.* HVCN1 modulates BCR signal strength via regulation of BCR-dependent generation of reactive oxygen species. *Nat. Immunol.* 11, 265–72 (2010).

6.   Musset, B., Morgan, D., Cherny, V. V., MacGlashan, Jr., D. W., Thomas, L. L., Rios, E. & DeCoursey, T. E. A pH-stabilizing role of voltage-gated proton channels in IgE-mediated activation of human basophils. *Proc. Natl. Acad. Sci. U. S. A.* 105, 11020–5 (2008).

7.   Lishko, P. V, Botchkina, I. L., Fedorenko, A. & Kirichok, Y. Acid extrusion from human spermatozoa is mediated by flagellar voltage-gated proton channel. *Cell* 140, 327–37 (2010).

8.   Lishko, P. V & Kirichok, Y. The role of Hv1 and CatSper channels in sperm activation. *J. Physiol.* 588, 4667–72 (2010).

9.   Iovannisci, D., Illek, B. & Fischer, H. Function of the HVCN1 proton channel in airway epithelia and a naturally occurring mutation, M91T. *J. Gen. Physiol.* 136, 35–46 (2010).

10.   Hondares, E. *et al.* Enhanced activation of an amino-terminally truncated isoform of the voltage-gated proton channel HVCN1 enriched in malignant B cells. *Proc. Natl. Acad. Sci. U. S. A.* 111, 18078–83 (2014).

11.   Wang, Y., Li S. J., Pan, J., Che, Y., Yin, J. & Zhao, Q. Specific expression of the human voltage-gated proton channel Hv1 in highly metastatic breast cancer cells, promotes tumor progression and metastasis. *Biochem. Biophys. Res. Commun.* 412, 353–9 (2011).

12. Wang, Y., Li, S. J., Wu, X., Che, Y. & Li, Q. Clinicopathological and biological significance of human voltage-gated proton channel Hv1 protein overexpression in breast cancer. *J. Biol. Chem*. 287, 13877–88 (2012).

13. Wang, Y., Wu, X., Li, Q., Zhang, S. & Li, S. J. Human voltage-gated proton channel hv1: a new potential biomarker for diagnosis and prognosis of colorectal cancer. *PLoS One* 8, e70550 (2013).

14. Wu, L.-J., Wu, G., Sharif, M. R. A., Baker, A., Jia, Y., Fahey, F. H., Luo, H. R., Feener, E. P., Clapham, D. E. The voltage-gated proton channel Hv1 enhances brain damage from ischemic stroke. *Nat. Neurosci*. 15, 565–73 (2012).

15. Hille, B. *Ion Channels of Excitable Membranes*. (Sinauer Associates, Inc., 2001).

16. Ramsey, I. S., Moran, M. M., Chong, J. A. & Clapham, D. E. A voltage-gated proton-selective channel lacking the pore domain. *Nature* 440, 1213–16 (2006).

17. Sasaki, M., Takagi, M. & Okamura, Y. A voltage sensor-domain protein is a voltage-gated proton channel. *Science* 312, 589–592 (2006).

18. Tombola, F., Ulbrich, M. H., Kohout, S. C. & Isacoff, E. Y. The opening of the two pores of the Hv1 voltage-gated proton channel is tuned by cooperativity. *Nat. Struct. Mol. Biol*. 17, 44–50 (2010).

19. Tombola, F., Ulbrich, M. H. & Isacoff, E. Y. The voltage-gated proton channel Hv1 has two pores, each controlled by one voltage sensor. *Neuron* 58, 546–56 (2008).

20. Jiang, Y., Ruta, V., Chen, J., Lee, A. & MacKinnon, R. The principle of gating charge movement in a voltage-dependent K^+ channel. *Nature* 423, 42–8 (2003).

21. Aggarwal, S. K. & MacKinnon, R. Contribution of the S4 Segment to Gating Charge in the Shaker K^+ Channel. *Neuron* 16, 1169–1177 (1996).

22. Takeshita, K., Sakata, S., Yamashita, E., Fujiwara, Y., Kawanabe, A., Kurokawa, T., Okochi, Y., Matsuda, M., Narita, H., Okamura, Y. & Nakagawa, A. X-ray crystal structure of voltage-gated proton channel. *Nat. Struct. Mol. Biol*. 21, 352–7 (2014).

23. Wood, M. L., Schow, E. V., Freites, J. A., White, S. H., Tombola, F. & Tobias, D. J. Water wires in atomistic models of the Hv1 proton channel. *Biochim. Biophys. Acta* 1818, 286–93 (2012).

24. Kulleperuma, K., Smith, S. M. E., Morgan, D., Musset, B., Holyoake, J., Chakrabarti, N., Cherny, V. V., DeCoursey, T. E. & Pomès, R. Construction and validation of a homology model of the human voltage-gated proton channel hHV1. *J. Gen. Physiol*. 141, 445–65 (2013).

25. Chamberlin, A., Qui, F., Rebolledo, S., Wang, Y., Noskov, S. Y. & Larsson, H. P. Hydrophobic plug functions as a gate in voltage-gated proton channels. *Proc. Natl. Acad. Sci. U. S. A*. 111, E273-82 (2014).

26. Gianti, E., Delemotte, L., Klein, M. L. & Carnevale, V. On the role of water density fluctuations in the inhibition of a proton channel. *Proc. Natl. Acad. Sci. U. S. A.* 113, E8359–E8368 (2016).

27. Randolph, A. L., Mokrab, Y., Bennett, A. L., Sansom, M. S. & Ramsey, I. S. Proton currents constrain structural models of voltage sensor activation. *Elife* 5, (2016).

28. Kelley, L. A., Mezulis, S., Yates, C. M., Wass, M. N. & Sternberg, M. J. E. The Phyre2 web portal for protein modeling, prediction and analysis. *Nat. Protoc*. 10, 845–858 (2015).

29. Koch, H. P., Kurokawa, T., Okochi, Y., Sasaki, M., Okamura, Y. & Larsson, H. P. Multimeric nature of voltage-gated proton channels. *Proc. Natl. Acad. Sci. U. S. A*. 105, 9111–16 (2008).

30. Jo, S., Kim, T., Iyer, V. G. & Im, W. CHARMM-GUI: a web-based graphical user interface for CHARMM. *J. Comput. Chem.* 29, 1859–65 (2008).

31. Phillips, J. C., Braun, R., Wang, W., Gumbart, J., Tajkhorshid, E., Villa, E., Chipot, C., Skeel, R. D., Kalé, L. & Schulten, K. Scalable molecular dynamics with NAMD. *J. Comput. Chem*. 26, 1781–802 (2005).

32. MacKerell, A. D. *et al*. All-Atom Empirical Potential for Molecular Modeling and Dynamics Studies of Proteins. *J. Phys. Chem. B* 102, 3586–3616 (1998).

33. Mackerell, A. D., Feig, M. & Brooks, C. L. Extending the treatment of backbone energetics in protein force fields: limitations of gas-phase quantum mechanics in reproducing protein conformational distributions in molecular dynamics simulations. *J. Comput. Chem*. 25, 1400–15 (2004).

34. Best, R. B., Zhu, X., Shim, J., Lopes, P. E. M., Mittal, J., Feig, M. & MacKerell Jr., A. D. Optimization of the additive CHARMM all-atom protein force field targeting improved sampling of the backbone φ, ψ and side-chain χ(1) and χ(2) dihedral angles. *J. Chem. Theory Comput*. 8, 3257–3273 (2012).

35. Klauda, J. B., Venable, R. M., Freites, J. A., O'Connor, J. W., Tobias, D. J., Mondragon-Ramirez, C., Vorobyov, I., MacKerell Jr., A. D. & Pastor, R. W. Update of the CHARMM all-atom additive force field for lipids: validation on six lipid types. *J. Phys. Chem. B* 114, 7830–43 (2010).

36. Jorgensen, W. L., Chandrasekhar, J., Madura, J. D., Impey, R. W. & Klein, M. L. Comparison of simple potential functions for simulating liquid water. *J. Chem. Phys.* 79, 926 (1983).

37. Shaw, D. E. *et al.* Anton, a special-purpose machine for molecular dynamics simulation. *Commun. ACM* 51, 91 (2008).

38. Freites, J. A., Schow, E. V, White, S. H. & Tobias, D. J. Microscopic origin of gating current fluctuations in a potassium channel voltage sensor. *Biophys. J.* 102, L44-6 (2012).

39. Tuckerman, M., Berne, B. J. & Martyna, G. J. Reversible multiple time scale molecular dynamics. *J. Chem. Phys.* 97, 1990 (1992).

40. Shan, Y., Klepeis, J. L., Eastwood, M. P., Dror, R. O. & Shaw, D. E. Gaussian split Ewald: A fast Ewald mesh method for molecular simulation. *J. Chem. Phys.* 122, 054101 (2005).

41. Ryckaert, J.-P., Ciccotti, G. & Berendsen, H. J. C. Numerical integration of the cartesian equations of motion of a system with constraints: molecular dynamics of n-alkanes. *J. Comput. Phys.* 23, 327–341 (1977).

42. Martyna, G. J., Klein, M. L. & Tuckerman, M. Nosé–Hoover chains: The canonical ensemble via continuous dynamics. *J. Chem. Phys.* 97, 2635 (1992).

43. Martyna, G. J., Tobias, D. J. & Klein, M. L. Constant pressure molecular dynamics algorithms. *J. Chem. Phys.* 101, 4177 (1994).

44. Lippert, R. A., Predescu, C., Ierardi, D. J., Mackenzie, K. M., Eastwood, M. P., Dror, R. O. & Shaw, D. E. Accurate and efficient integration for molecular dynamics simulations at constant temperature and pressure. *J. Chem. Phys.* 139, 164106 (2013).

45. Roux, B. The membrane potential and its representation by a constant electric field in computer simulations. *Biophys. J.* 95, 4205–16 (2008).

46. Trott, O. & Olson, A. J. AutoDock Vina: improving the speed and accuracy of docking with a new scoring function, efficient optimization, and multithreading. *J. Comput. Chem.* 31, 455–61 (2010).

47. Humphrey, W., Dalke, A. & Schulten, K. VMD: Visual molecular dynamics. *J. Mol. Graph.* 14, 33–38 (1996).

48. Musset, B., Smith, S. M. E., Rajan, S., Morgan, D., Cherny, V. V. & DeCoursey, T. E. Aspartate 112 is the selectivity filter of the human voltage-gated proton channel. *Nature* 480, 273–277 (2011).

49. Jogini, V. & Roux, B. Dynamics of the Kv1.2 Voltage-Gated K^+ Channel in a Membrane Environment. *Biophys. J.* 93, 3070–3082 (2007).

50. Khalili-Araghi, F., Jogini, V., Yarov-Yarovoy, V., Tajkhorshid, E., Roux, B. & Schulten, K. Calculation of the gating charge for the Kv1.2 voltage-activated potassium channel. *Biophys. J.* 98, 2189–98 (2010).

51. Fujiwara, Y., Kurokawa, T., Takeshita, K., Kobayashi, M., Okochi, Y., Nakagawa, A. & Okamura, Y. The cytoplasmic coiled-coil mediates cooperative gating temperature sensitivity in the voltage-gated H^+ channel Hv1. *Nat. Commun.* 3, 816 (2012).

52. Gonzalez, C., Koch, H. P., Drum, B. M. & Larsson, H. P. Strong cooperativity between subunits in voltage-gated proton channels. *Nat. Struct. Mol. Biol.* 17, 51–6 (2010).

53. De La Rosa, V. & Ramsey, I. S. Gating Currents in the Hv1 Proton Channel. *Biophys. J.* 114, 2844–2854 (2018).

54. Hong, L., Pathak, M. M., Kim, I. H., Ta, D. & Tombola, F. Voltage-sensing domain of voltage-gated proton channel Hv1 shares mechanism of block with pore domains. *Neuron* 77, 274–87 (2013).

55. Henrion, U., Renhorn, J., Börjesson, S. I., Nelson, E. M., Schwaiger, C. S., Bjelkmar, P., Wallner, B., Lindahl, E. & Elinder, F. Tracking a complete voltage-sensor cycle with metal-ion bridges. *Proc. Natl. Acad. Sci. U. S. A.* 109, 8552–7 (2012).

56. Shen, R., Han, W., Fiorin, G., Islam, S. M., Schulten, K. & Roux, B. Structural Refinement of Proteins by Restrained Molecular Dynamics Simulations with Non-interacting Molecular Fragments. *PLoS Comput. Biol.* 11, e1004368 (2015).

57. Li, Q., Shen, R., Treger, J. S., Wanderling, S. S., Milewski, W., Siwowska, K., Bezanilla, F. & Perozo, E. Resting state of the human proton channel dimer in a lipid bilayer. *Proc. Natl. Acad. Sci. U. S. A.* 112, E5926–E5935 (2015).

58. Li, Q. *et al.* Structural mechanism of voltage-dependent gating in an isolated voltage-sensing domain. *Nat. Struct. Mol. Biol.* 21, 244–52 (2014).

59. van Keulen, S. C., Gianti, E., Carnevale, V., Klein, M. L., Rothlisberger, U. & Delemotte, L. Does Proton Conduction in the Voltage-Gated H^+ Channel hHv1 Involve Grotthuss-Like Hopping via Acidic Residues? *J. Phys. Chem.* B 121, 3340–3351 (2017).

60. Ramsey, I. S., Mokrab, Y., Carvacho, I., Sands, Z. A., Sansom, M. S. P. & Clapham, D. E. An aqueous H^+ permeation pathway in the voltage-gated proton channel Hv1. *Nat. Struct. Mol. Biol.* 17, 869–875 (2010).

61. Hong, L., Singh, V., Wulff, H. & Tombola, F. Interrogation of the intersubunit interface of the open Hv1 proton channel with a probe of allosteric coupling. *Sci. Rep.* 5, 14077 (2015).

62. Li, S. J., Zhao, Q., Zhou, Q., Unno, H., Zhai, Y. & Sun F. The role and structure of the carboxyl-terminal domain of the human voltage-gated proton channel Hv1. *J. Biol. Chem*. 285, 12047–12054 (2010).

Chapter 3

Voltage-Dependent Profile Structures of a Kv-Channel via Time-Resolved Neutron Interferometry

3.1 Background

Nav- and Kv-channels are voltage-gated ion channels (VGICs) selective for sodium or potassium, respectively, that are responsible for the generation and propagation of action potentials in neurological signal transmission.[1] The mechanism of coupling conformational changes within the four voltage sensor domains (VSDs) in response to a change in the transmembrane voltage, either depolarizing or polarizing relative to the resting voltage, to opening or closing the channel within the pore domain (PD), remains unknown.[2,3] VGICs are deactivated at the resting transmembrane voltage of -60 mV to -70 mV, and experience the absence of a transmembrane voltage only transiently during the course of an action potential of a few milliseconds duration.[4] To date, higher resolution 3-D structures for VGICs have only been provided by conventional techniques (x-ray crystallography, cryo-EM) in the absence of a transmembrane voltage.[5–7] This seriously complicates any investigation into the mechanism of electromechanical coupling. For example, in the case of Kv channels for which the first high-resolution structures were obtained, the channel within the PD was found to be open, and the conformations of the VSDs were assumed to be

activated since 0 mV would be sufficiently depolarizing.[5,8] In the absence of a structure for the deactivated, closed state of Kv channels, numerous models were developed employing various computational approaches, each relying on specific assumptions.[2,3] Several incorporated restraints based on experimental results provided by indirect techniques.[9–13] For example, one utilized pairs of site-directed cysteine mutations and measurements of metal cross-linking as a function of the transmembrane voltage.[14] Other approaches attempted to induce the deactivated, closed state by applying hyperpolarizing transmembrane voltages.[15–17] The most successful of these utilized very long 250 μs MD simulations.[18] Overall, such studies demonstrated a high degree of similarity in the atomic models, thereby achieving a "consensus" structure for the deactivated, closed state of Kv channels.[2] However, despite the "consensus" noted, experimental validation utilizing one or more direct techniques remains essential.

Some developments were needed to investigate the voltage-dependent structures of VGICs directly, without having to resort to one or more site-directed mutations and subsequent labelling with bulky chromophores or heavy metals. We first developed two methods for the fabrication of single membrane specimens, comprised of a phospholipid bilayer containing a vectorially-oriented voltage-gated K^+ channel protein at high in-plane density, tethered to the surface of an inorganic multilayer substrate to allow for the application of transmembrane voltages in an electrochemical cell.[19,20] The structures of the tethered single membrane specimens were then characterized by both x-ray reflectivity[19] and neutron reflectivity,[21] each enhanced by interferometry enabled by the multilayer substrate.[20–22] The electrical properties of the membranes were characterized by electrical impedance spectroscopy (EIS). With these essential developments, we then utilized time-resolved x-ray and neutron interferometry to investigate the dependence of the so-called "profile structure" of the isolated VSD of the prokaryotic Kv channel KvAP on physiologically relevant

transmembrane voltages that were nonpolarizing, polarizing and depolarizing with respect to the transmembrane resting voltage.[23] The profile structure is the projection of the 3-D structure of the membrane parallel to the membrane plane onto the membrane normal and is dominated by the protein component at the high in-plane density. In these time-resolved, "pump-probe" experiments, the three voltages were applied cyclically, and the interferometry data were collected separately for each voltage and subsequently averaged. For the x-ray case employing a pulsed synchrotron source, radiation damage to the specimens was detected after only three voltage cycles, although the incident photon flux was sufficiently high to provide accurate x-ray scattering-length density (xSLD) profiles for each voltage within a single cycle. For the neutron case utilizing a pulsed spallation source, the incident neutron flux was dramatically lower, therefore requiring many voltage cycles to provide accurate neutron scattering-length density (nSLD) profiles made possible by the absence of any detectable radiation damage to the specimens. The voltage-dependent xSLD and nSLD profile structures for the isolated VSD of KvAP determined from these time-resolved experiments were found to be in good agreement with long (multi-μs) molecular dynamics (MD) simulations of the same VSD protein within a hydrated phospholipid bilayer membrane investigated as a function of similar physiologically-relevant transmembrane voltages.[24]

In this work, we extended our time-resolved neutron interferometry approach to investigate the dependence of the profile structure of the complete homo-tetrameric prokaryotic Kv channel KvAP, vectorially oriented within a phospholipid bilayer membrane at a solid-liquid interface, on the transmembrane voltage. A cyclic sequence of hyperpolarizing and depolarizing voltage pulses, whose amplitudes and duration were judiciously selected to circumvent the inactivation exhibited by the complete homotetrameric channel,[25] was synchronized with the pulsed neutron source.

41

Averaging the data for each of the hyperpolarizing and depolarizing voltage pulses collected over many cycles provided the nSLD profile structure of the membrane for the deactivated, closed state (hyperpolarized) and activated, open state (depolarized) of the channel, as well as the profile structure for water within the Kv channel for these two end states, the latter enabled by using neutrons.[20] There were two key experimental results from this study, namely the difference ΔnSLD profile structures for both the membrane and for water within the membrane, each calculated as the nSLD profile for the deactivated, closed state (hyperpolarized) minus the nSLD profile for the activated, open state (depolarized). The two key results were then compared with those predicted by three fundamentally different computational approaches to modeling these same two states for three different voltage-gated K^+ channels in hydrated phospholipid bilayer membranes. They included a targeted MD simulation applied to the prokaryotic KvAP channel,[13] ROSETTA membrane protein structure prediction followed by MD simulation applied to the transmembrane domain of the eukaryotic Kv1.2 channel,[9–11] and a state-of-the-art, 250 μs timescale MD simulation applied to the transmembrane domain of the eukaryotic Kv1.2/2.1 chimera channel.[18] Only one of these computational approaches was found to be in agreement with both of the two key experimental results for the KvAP channel provided by our time-resolved neutron interferometry experiments.

3.2 Materials and Methods

3.2.1 Expression and purification of KvAP protein

The KvAP gene (coding for residues 14–295 of the protein) was amplified from a PQE60 plasmid that was kindly provided by Dr. Rod McKinnon (Rockefeller University). The gene was inserted into the in-house pETCH vector,[26] which supplies a C-terminal His_6 tag. The plasmid was inserted

into C41(DE3) cells, which were grown in Lurai-Bertani medium at 37°C. When the OD_{600} value reached 0.8, protein expression was induced by addition of 0.4 mM isopropylthiogalactoside; 10 mM $BaCl_2$ was added to the medium at the same time. Cells were harvested after 4 hours, washed with water, and frozen.

All purification steps were carried out at 4°C. Cells were lysed in 20 mM Tris (pH 8), 100 mM KCl (buffer A) using an Emulsiflex cell disruptor operating at 20,000 psi. The lysate was centrifuged at 14,000 × g for 15 min, after which the supernatant was centrifuged at 200,000 × g for 1 hour to isolate the membrane fraction. The membrane pellet was resuspended in buffer A and *n*-decyl-β-D-maltopyranoside (DM) was added to a final concentration of 1.9% (w/v). After one hour, the suspension was centrifuged again at 200,000 × g for one hour. The supernatant was filtered and applied to a 1 mL HisTrap-HP column (GE LifeSciences) equilibrated with buffer A + 0.24% DM. KvAP was eluted with a gradient from 0 to 400 mM imidazole. Fractions containing KvAP were pooled and dialyzed versus buffer A + 0.24% DM. The protein was then reduced with 1 mM TCEP for an hour, after which it was concentrated to approximately 10 mg/mL. DM concentrations in the concentrated protein sample were measured by analytical thin-layer chromatography,[27] and were typically found to be approximately 5% (w/v). A sample of the concentrated protein was analyzed by size-exclusion chromatography on a Sephacryl S-200 column in Buffer A + 0.24% DM, and found to migrate as a tetramer. Aliquots of the concentrated protein were flash-frozen in liquid nitrogen.

3.2.2 Specimens for x-ray interferometry and time-resolved neutron interferometry experiments

We used a modified version of the Self-Assembly method[19] to tether the homotetrameric KvAP solubilized in DM, designated as KvAP-DM, to the surface of Si-Ge-Si multilayer on silicon substrates to result in a unique vectorial orientation of the KvAP protein with respect to the normal to the substrate surface. The modifications included utilizing 3-aminopropyldimethylethoxysilane (Gelest) to alkylate the silicon oxide surface of the substrate, followed by sequential reaction with three linkers: succinic anhydride (Sigma), 1-ethyl-3(3-dimethylaminopropyl)carbodiimide hydrochloride (Pierce Biotechnology) and N-hydroxysuccinimide (Pierce) followed by surface functionalization with N_α,N_α-Bis(carboxymethyl)-L-lysine hydrate (Sigma), to produce an alkylated substrate surface possessing nitrilotriacetate endgroups. The modifications resulted in improved specimen-to-specimen reproducibility for tethering KvAP-DM to the surface of the Si-Ge-Si multilayer on silicon substrates. Each silicon or germanium layer in the multilayer was of ~20Å thickness, fabricated by magnetron sputtering at the Advanced Photon Source, Argonne National Laboratory. The detergent was subsequently exchanged for POPC (1-palmitoyl-2-oleoylphosphatidylcholine; Avanti Polar Lipids) following the self-assembly method.[19]

3.2.3 Electrochemical cell for time-resolved neutron interferometry experiments

The basic features of the electrochemical cells used for the time-resolved neutron interferometry experiments reported herein were similar to those for the cells used previously for the closely related experiments with the isolated VSD from KvAP.[23] Here, instead of a Si-Ni-Si multilayer on silicon substrate as in the reference, the working electrode was provided by a Si-Ge-Si multilayer on a silicon substrate, the latter being heavily-doped with phosphorus to make it sufficiently conductive (R < 1 Ωcm^2), which was held at ground potential. The electric potential (voltage) was applied to the membrane on the surface of the Si-Ge-Si multilayer substrate via a platinum counter

electrode in the aqueous electrolyte comprised of 0.1 M KCl in 1 mM Tris buffer at pH 8. For either the isolated VSD studied previously[23] or KvAP itself tethered to the substrate surface via a His-tag on the protein's C-terminus in this study, this is exactly opposite to the electrophysiological convention where the extracellular side of the membrane is at ground potential and the electric potential is applied to the cytoplasmic side.

3.2.4 Design of the neutron interferometry "pump-probe" experiment to avoid KvAP inactivation

In a classic "pump-probe" experiment, the membrane containing the vectorially-oriented Kv channel is subjected to a periodic alternating sequence of polarizing and depolarizing pulses with respect to the resting transmembrane voltage, each of constant amplitude and finite duration, and the membrane structure is synchronously probed with a small number of neutron pulses for each voltage pulse applied to the membrane. This approach has the absolute requirement that both the activation of the four VSDs and subsequent opening of the channel within the PD produced by the depolarizing voltage pulse, and the deactivation of the four VSDs and closing of the channel within the PD produced by the polarizing voltage pulse, be completely reversible. Utilizing a pulsed neutron source like the Spallation Neutron Source at Oak Ridge National Laboratory, although the incident neutron pulses are of only ~10 μs duration, the momentum transfer $\vec{Q}$ (see Supporting Materials, Section a) for each scattered neutron is determined by time-of-flight (TOF) which requires 16.5 ms. Hence, the number of neutron pulses employed for each voltage pulse depends on the duration of the TOF, down to the lower limit of one neutron pulse for a voltage pulse of 16.5 ms duration.

However, all Nav and Kv channels exhibit inactivation, even those that do not possess the additional cytoplasmic domain of eukaryotic channels, but only a transmembrane domain like the prokaryotic Kv channel KvAP utilized in this work. For an ensemble of channels, only a fraction of the ensemble can be activated in response to a second sufficiently depolarizing voltage pulse to result in pore opening and a measurable potassium current if the first depolarizing pulse is of too long a duration. For KvAP, using polarizing pulses of -120 mV and depolarizing pulses of +100 mV (electrophysiological convention), each of 150 ms duration, only about one third of the ensemble can be activated by a second depolarizing pulse.[25] After four pulses, the entire ensemble is inactivated. Unfortunately, reactivation occurs only on a much longer time-scale, namely about 90 s for KvAP incorporated into a planar phospholipid bilayer comprised of POPC:POPG-decane.[25] This situation would render such a "pump-probe" experiment as described above essentially impossible because the experiment would be exceedingly inefficient utilizing only an infinitesimal fraction (1/600) of the incident neutron flux available, noting the incident neutron pulse rate of 60 Hz, to achieve the requirement of complete reversibility. However, a judicious choice of both the amplitude and duration of the polarizing and depolarizing voltage pulses can be used to circumvent inactivation for a particular Kv channel depending on its membrane environment. As shown in Figure 4 of reference (25), choosing more hyperpolarizing pulses of -150 mV and less depolarizing pulses of +20 mV, each of only 50 ms duration, can be employed to eliminate any measurable inactivation for KvAP in a planar phospholipid bilayer comprised of POPC:POPG-decane. As a result of the above considerations, we employed 3 neutron pulses for each hyperpolarizing or depolarizing voltage pulse, this number averaging over the complete activation of the KvAP channel ensemble upon application of each depolarizing voltage pulse from inspection of Figure 1 of reference (25).

3.2.5 X-ray interferometry data collection

X-ray interferometry data were collected from several specimens, each comprised of either a KvAP-DM monolayer or a KvAP-POPC membrane following POPC-DM exchange, tethered to the surface of the same Si-Ge-Si multilayer substrate. The specimens were maintained in a hydrated state with moist He at 95% relative humidity in a thermo-regulated specimen chamber with Kapton windows. Specular x-ray reflectivity data were collected at 8.048 keV (1.543 Å), using a rotating-anode x-ray source, singly bent LiF monochromator incident beam optics, a Huber 4-circle diffractometer, a Si(111) analyzer and a scintillation detector, via θ-2θ scans as described previously.[19] These data were subsequently corrected for the incident beam footprint on the planar specimen depending on the angle of incidence, and for off-specular background scattering.

3.2.6 Time-resolved neutron interferometry data collection

Time-resolved neutron interferometry data were collected with the Magnetism Reflectometer on Beamline 4A at the Spallation Neutron Source, Oak Ridge National Laboratory.[28] Several specimens were investigated comprised of either a KvAP-POPC membrane tethered to the surface of a Si-Ge-Si multilayer substrate (four), or just the self-assembled monolayer (SAM) used to tether KvAP-DM to the substrate as a voltage-insensitive "control" (two). The incident neutron pulses are polychromatic and of ~10 μs duration at a repetition rate of 60 Hz. 16.5 ms is required to determine the momentum transfer vector $\vec{Q}$ of each reflected neutron via TOF. The cyclic sequence of hyperpolarizing voltage pulses of 150 mV and depolarizing voltage pulses of 20 mV, each of 50 ms duration and constant amplitude, were synchronized with the incident neutron pulses so that there were 3 neutron pulses for each voltage pulse. In order to achieve acceptable reflected neutron counting statistics, reflectivity data were collected from each specimen for 3–200 minutes,

for each of the six angles of incidence employed to span the range of Q_z accessed using the polychromatic neutron pulses. The time required increased with angle of incidence, and the reflected neutrons for each triplet of neutron pulses were collected separately and subsequently averaged over each of the hyperpolarizing or depolarizing voltage pulses. Given the incident neutron pulse rate, this implies that the reflectivity data for each transmembrane voltage were averaged over 10^3–10^6 cycles of the voltage pulse sequence. The time-averaged specular reflectivity data for each transmembrane voltage was then calculated, and the time-averaged data were subsequently corrected for the incident beam footprint on the planar specimen depending on the angle of incidence, and for off-specular background scattering.

3.2.7 X-ray interferometry data analysis

The specular x-ray interferometry data for the KvAP-DM monolayer and KvAP-POPC membrane specimens were analyzed using a constrained refinement approach analogous to that described previously[19] to provide their respective xSLD profile.

3.2.8 Time-resolved neutron interferometry data analysis

The time-averaged specular neutron interferometry data for either the hyperpolarizing or the depolarizing voltage pulses was analyzed, using a constrained refinement approach analogous to that first described previously for a tethered protein monolayer at the solid-gas interface,[29] to provide the nSLD profile for each voltage.

3.2.9 Estimation of error propagation in the x-ray and neutron interferometry data analysis

As described in the Supporting Material, Section a, our data analysis employs the Fresnel-normalized x-ray or neutron interferometry data $R(Q_z)/R_F(Q_z)$, where the specular reflectivity data $R(Q_z)$ containing the standard errors determined by the photon/neutron counting statistics has been divided by an analytic function $R_F(Q_z)$ describing the reflectivity from a single ideal interface. The constrained refinement approach employs Fourier transformations to produce the xSLD or nSLD profile structures which obscure the standard errors in the reflectivity data. For the x-ray case, the propagation of errors from the data into the xSLD profiles was estimated utilizing a region of the profile that should be of constant xSLD. As shown in Figure 3.2A, this occurs for the KvAP-DM specimens over the region 50 Å < z < 100 Å, which is occupied by only the moist helium environment. The low amplitude oscillations about zero xSLD in this region arise from error propagation with a wavelength determined by the truncation of the inverse Fourier transformation at a maximum Q_z of 0.427 Å^{-1}. For the neutron case, the time resolved experiments employed "control" specimens comprised of only the Si-Ge-Si multilayer substrate on silicon and the organic self-assembled monolayer (SAM), otherwise used to tether the KvAP-POPC membrane to the substrate's surface. These control specimens were not expected to exhibit any dependence on the transmembrane voltage applied to the KvAP-POPC membrane specimens. As shown in Figure 3.4C, the difference ΔnSLD profile for the SAM specimen (hyperpolarizing - depolarizing) over the region 0 Å < z < 100 Å, otherwise occupied by the KvAP-POPC membrane when present, exhibits only low amplitude oscillations about zero nSLD in this region. These low amplitude oscillations arise from error propagation with a wavelength determined by the truncation of the inverse Fourier transformation at a maximum Q_z of 0.194 Å^{-1}. Since errors propagate in difference ΔnSLD profiles as the square root of the sum of the squares of the errors in each nSLD

profile contributing to the difference profile, the standard errors in each contributing nSLD profile are then smaller by a factor of $1/\sqrt{2}$.

3.2.10 Modeling the voltage-dependent nSLD profiles for the KvAP-POPC membrane

We believe that it is essential that all-atom MD simulation be incorporated in any approach to modeling either the activated, open state or the deactivated, closed state of a Kv channel protein within a hydrated phospholipid bilayer environment for two reasons. First, the elastic scattering experiment (neutron interferometry) is sensitive only to the time average over the dynamics inherent in such a membrane system. Second, upon embedding a particular state of the protein within the hydrated phospholipid bilayer, the protein must be allowed to relax in response to its environment within the bilayer and conversely, the hydrated bilayer must be allowed to relax in response to the embedded protein. These processes cannot be accurately modeled using static structure representations. In Supporting Materials, Section c, we describe in detail the modeling of the activated, open and deactivated closed states of three Kv channels in a hydrated phospholipid bilayer. These include the transmembrane domain of the eukaryotic Kv1.2/2.1 chimera, the transmembrane domain of the eukaryotic Kv1.2, and the prokaryotic KvAP. Importantly, we also describe how the atomic level detail in the MD simulations is utilized to produce the time-averaged nSLD profiles for either the entire membrane, or the nSLD profiles for the separate protein, lipid and water components, for comparison with their experimental counterparts. A portion of the MD trajectories for either the activated, open state or the deactivated, closed state of Kv channel in the hydrated POPC bilayer was selected over which the system demonstrated stability. These portions were the same length for each state and were sampled at uniform intervals to generate a number

of instantaneous configurations of the system used to calculate the time-averaged nSLD profiles. For the membrane, the atom selection included the protein, water and lipid within a cylinder of defined radius that extended from the center of the protein outward perpendicular to the transmembrane axis. Each selected atom was binned into 0.5 Å steps along the transmembrane-axis for each of the sampled configurations. The neutron atomic scattering lengths were summed for each bin and these values were averaged over all sampled configurations to construct the time-averaged nSLD profile for each state of the Kv-channel. The origin was defined as the protein center of mass for each configuration. Different deuteration ratios were achieved by randomly selecting a fraction of the hydrogen atoms on water and polar hydrogens on the protein to replace with deuterium. The same approach was employed to calculate the separate time-averaged nSLD profiles for the protein, lipid and water components of the membrane as determined by the atom selection.

For the activated, open state of both the Kv1.2/2.1 chimera and the KvAP channel in a hydrated POPC bilayer membrane, we also calculated the resolution-limited nSLD profiles of the separate protein and lipid components. This was accomplished by the least-squares fitting of slab models,[21] based on a finite sum of error functions, to the time-averaged nSLD profiles for either the activated, open state of the protein or the host POPC bilayer, each hydrated with 100% D_2O. Their resolution-limited counterparts were then calculated via Fourier transformation into momentum transfer space (Q_z), followed by inverse Fourier transformation back into real space (z) at somewhat higher spatial resolution than in the experimental nSLD profiles using twice the maximum value of Q_z (i.e., $2 \times 0.194 Å^{-1}$) in the time-resolved neutron interferometry experiments. Thus, the minimum wavelength component in these resolution-limited nSLD profiles is half that of the experimental nSLD profiles, allowing important visualization of the influence of somewhat finer details in the

model profiles on their overall shape at the experimental spatial resolution. Linear combinations of the separate resolution-limited nSLD profiles for the activated, open state of the protein and the host POPC bilayer hydrated with D_2O were then calculated thereby allowing for manipulation of the lipid/protein mole ratio to match that of the experimental KvAP-POPC membrane employed in the time-resolved neutron interferometry experiments. This was essential for the Kv1.2/2.1 chimera protein since the MD simulation cell contained twice the amount of POPC compared with that for the experimental KvAP-POPC membrane.

3.3 Results

3.3.1 Folding KvAP at the solid-liquid interface

Based on a comparison of the x-ray crystal structures for the prokaryotic KvAP channel determined in a detergent micellar environment[30] and the eukaryotic Kv1.2 channel determined in a mixed phospholipid-detergent micellar environment,[8] it was proposed[31] that the VSDs of KvAP would undergo refolding to form a four-helix bundle motif and a substantial reorientation of the bundle axis upon transfer from a micellar detergent environment to that of a phospholipid bilayer. Thus, we first investigated the profile structure of KvAP-DM within a monolayer tethered to the surface of a Si-Ge-Si multilayer substrate, and subsequently the profile structure of the tethered KvAP-POPC membrane following detergent-phospholipid exchange employing the self-assembly method, performing x-ray interferometry following each stage of fabrication in a moist helium environment.[19] Numerous specimens were investigated, using both Si-Ge-Si multilayer substrates (four), as well as monolayer graphene on Si-Ge-Si multilayer substrates (four). For the latter, tethering the KvAP-DM monolayer to the graphene surface was achieved as in reference.[32] In Figure 3.1, we show typical Fresnel-normalized specular x-ray reflectivity data for the specimens
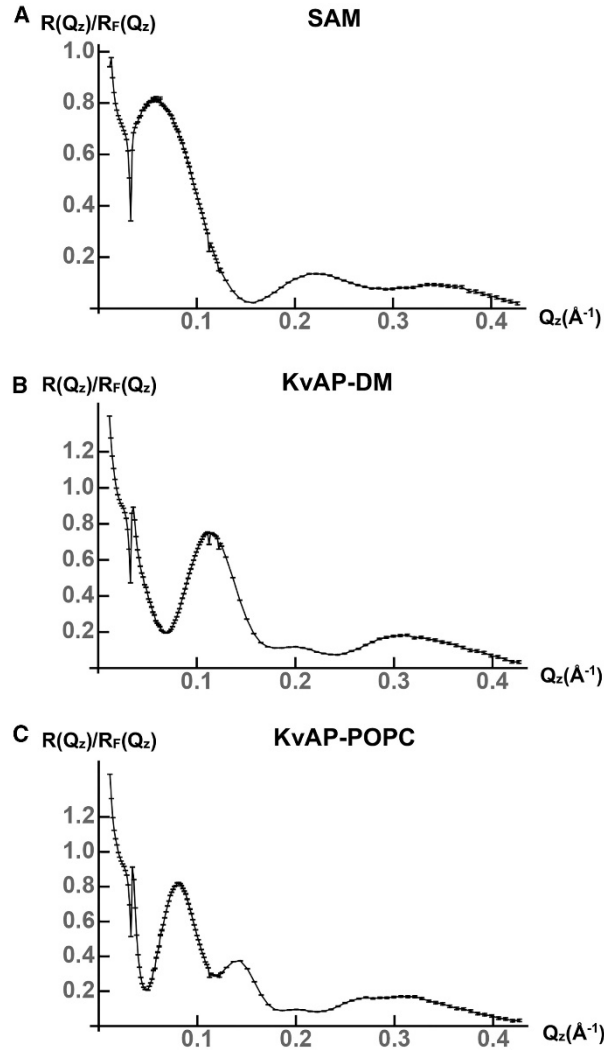
Figure 3.1. Fresnel-normalized x-ray interferometry data $R(Q_z)/R_F(Q_z)$ with regard to folding KvAP at the solid-liquid interface. (A) $R(Q_z)/R_F(Q_z)$ data for the organic self-assembled monolayer (SAM) used to tether the KvAP-DM monolayer to the surface of an Si-Ge-Si multilayer substrate are shown. (B) $R(Q_z)/R_F(Q_z)$ data for a KvAP-DM monolayer tethered to the surface of an Si-Ge-Si multilayer substrate are shown. (C) $R(Q_z)/R_F(Q_z)$ data for a KvAP-POPC membrane tethered to the surface of the same Si-Ge-Si multilayer substrate are shown. Error bars are based on the photon-counting statistics.

on Si-Ge-Si multilayer substrates. Figure 3.1A is the data for the substrate possessing only the organic self-assembled monolayer (SAM) used subsequently to tether the KvAP-DM monolayer to its surface, Figure 3.1B for the substrate with the tethered KvAP-DM monolayer on its surface and Figure 3.1C for the substrate with the tethered KvAP-POPC membrane on its surface following POPC-DM exchange. The error bars are based on the photon counting statistics. In Figure 3.2A, we show the xSLD profile for a typical KvAP-DM monolayer on the surface of either a Si-Ge-Si multilayer substrate or a monolayer graphene on Si-Ge-Si multilayer substrate using the constrained refinement approach. The horizontal dotted lines above and below the abscissa were used to estimate the propagation of errors from the reflectivity data into the xSLD profiles, described in Section 3.2.9. For the tethered KvAP-DM monolayers on either substrate, the xSLD profile of the monolayer occurred relatively close to the substrate's surface. In Figure 3.2B, we show the xSLD profiles for the Si-Ge-Si multilayer substrate with the KvAP-DM monolayer on its surface compared with only the SAM on its surface. The best xSLD profile for the KvAP-DM monolayer itself is the difference of these two profiles as shown in Figure 3.2C with estimated propagated error bars as described. Also shown in Figure 3.2C, the xSLD profile for the KvAP-DM monolayer can be seen to agree fairly well with that calculated from the x-ray crystal structure from reference (30). All specimens for the tethered KvAP-DM monolayer exhibited similar xSLD profiles. As shown in Figure 2D, there is a substantial change in the xSLD profile for the KvAP-POPC membrane following exchange of POPC for DM. The membrane is further from the substrate surface and thus, subtraction of the xSLD profile of the substrate with the SAM on its surface is not required. The estimated propagated errors are the same as for the KvAP-DM monolayer, noting the small change in ordinate scale. In Figure 3.2D, we have also superimposed the xSLD profiles calculated for the model proposed in reference (31), as described in Figure 3.2E,

as well as for rotations of the axis of the four-helix bundle VSDs of 5°, 10°, 15° and 20° less than the 90° rotation originally proposed. As can be seen from Figure 3.2D, a rotation by only 10° less than the 90° rotation originally proposed brings the model into close agreement with the experimental xSLD profile for the KvAP-POPC membrane dominated by the KvAP protein. Based on the estimated propagated errors in the experimental xSLD profile, we estimate that the rotation has been determined with a precision of about ±2°. In Figure 3.2F, we compare the 3-D structure for KvAP originally proposed[31] with that found in our experiments.

A majority of the specimens exhibited xSLD profiles for the KvAP-POPC membrane as shown in Figure 3.2D, while a minority exhibited xSLD profiles intermediate between that for the precursor KvAP-DM monolayer and that for the KvAP-POPC membrane, suggesting incomplete exchange. Electrical impedance spectroscopy (EIS) indicated a substantial increase in the resistance of the overlayer on the substrate's surface upon the transformation from the tethered KvAP-DM monolayer to a tethered KvAP-POPC membrane for all specimens. The resistance of the KvAP-POPC membrane tethered to the surface of graphene was $2.3×10^5$ to $1.3×10^6$ Ωcm^2, while that for the membrane tethered to the surface of silicon was $1.2×10^6$ to $4.7×10^6$ Ωcm^2. Thus, we concluded that a properly folded KvAP homotetramer within the POPC bilayer membrane, structurally homologous with Kv1.2 and capable of sensing changes in the transmembrane voltage, had been achieved.

Figure 3.2. (*next page*) Folding KvAP at the solid-liquid interface. (A) The xSLD(z) profile for a KvAP-DM monolayer tethered to the surface of an Si-Ge-Si multilayer substrate is shown. The horizontal dashed lines above and below the abscissa were used to estimate the propagation of errors. (B) The xSLD(z) profiles for an Si- Ge-Si multilayer substrate with only the organic SAM used to tether the KvAP-DM monolayer to its surface (*dashed*) and for a slightly different Si-Ge-Si multilayer substrate with a KvAP-DM monolayer tethered to its surface (*solid*) are shown. The xSLD profiles for the multilayer substrates occur for z < 0 Å, whereas those for the SAM or tethered KvAP-DM monolayer occur for z > 0 Å. (C) The xSLD(z) profile for the tethered KvAP-DM monolayer (*solid*) with estimated errors is shown, compared with the xSLD(z) profile calculated from the x-ray crystal structure for KvAP-DM (*dashed*). (D) The xSLD(z) profile for the KvAP-POPC membrane after POPC-DM exchange (*gray with estimated errors*) is shown, compared with the xSLD(z) profiles calculated for the model proposed for KvAP (*gray solid*) within a phospholipid bilayer environment described in (E), as well as for rotations of 5° (*dotted*), 10° (*black solid*), 15° (*dashed*), and 20° (*dash-dot*) less than the 90° originally proposed. (E) An illustration is given showing the proposed[31] refolding of the S1 helix to form a four-helix bundle structure for the VSDs and reorientation of the bundle axis relative to the pore axis of KvAP via a rotation of ~90° upon the transformation from a detergent micelle environment (*left side*) to a phospholipid bilayer environment (*right side*). One VSD is shown in the foreground (*black*) with the PD in the background (*gray*). (F) Top view and side view (of one subunit) of the 3-D structure proposed[31] for KvAP in a phospholipid bilayer environment is shown in a ribbon representation (*gray*), compared with that for a rotation of the VSDs by 10° less (*black*) than originally proposed. The xSLD(z) profiles are in units of electron density, $e^-/Å^3$.

A KvAP-DM
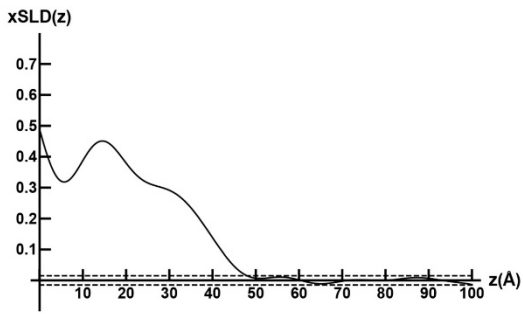
**B KvAP-DM & SAM**
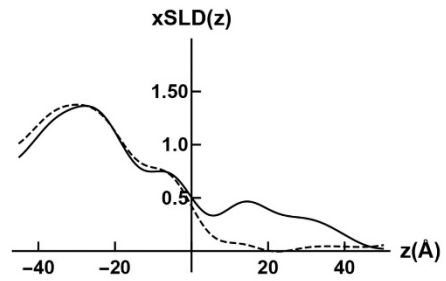

C KvAP-DM & Crystal Structure
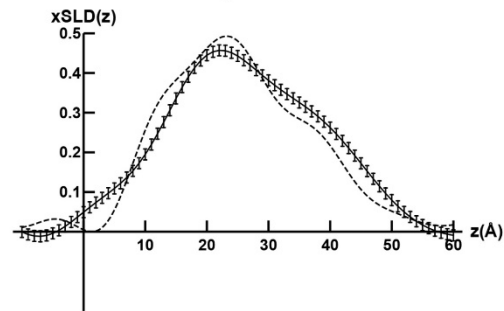
E KvAP Refolding Micelle→Bilayer
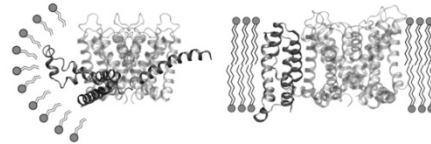
D KvAP-POPC vs Refolding KvAP
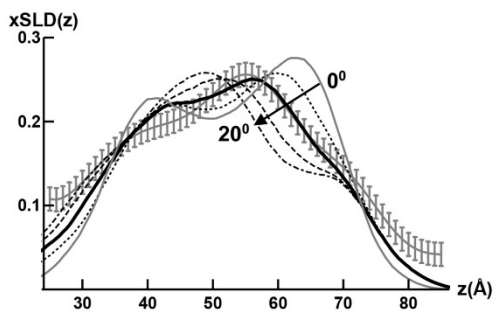
F Best Model Refolded KvAP

Proposed model
VSD rotated 10° out

KvAP top view   KvAP monomer side view
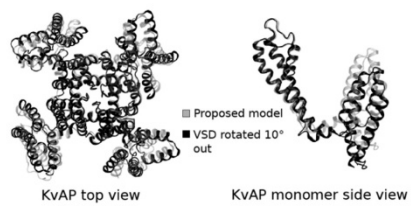
3.3.2 Time-resolved "pump-probe" neutron interferometry

We utilized a cyclic sequence of hyperpolarizing voltage pulses of 150 mV and depolarizing voltage pulses of 20 mV, each of 50 ms duration, in order to circumvent inactivation of the KvAP channel ensemble within a POPC bilayer membrane. The sequence of voltage pulses and synchronized neutron pulse triplets is depicted in Figure 3.3A. The Fresnel-normalized neutron interferometry data $R(Q_z)/R_F(Q_z)$ for one KvAP-POPC membrane (specimen S2), averaged over either the hyperpolarizing or depolarizing voltage pulses with standard errors based on the neutron counting statistics, are shown for aqueous solvent contrasts of 60% D_2O/40% H_2O in Figure 3.3B and 90% D_2O/10% H_2O in Figure 3.3C. There are experimentally significant differences in the mean of the $R(Q_z)/R_F(Q_z)$ data that exceed the standard errors consistently over small ranges of momentum transfer Q_z for both contrasts, becoming more evident with increasing Q_z, and somewhat larger for 60% D_2O/40% H_2O. Four different KvAP-POPC membrane specimens were investigated, and specimen-to-specimen reproducibility is addressed in Supporting Materials, Section b.

The nSLD profiles for specimen S2 at the aqueous solvent contrasts provided by 90% D_2O/10% H_2O and 60% D_2O/40% H_2O, derived from the $R(Q_z)/R_F(Q_z)$ data using the constrained refinement approach, are shown in Figure 3.4. The nSLD profile for the Si-Ge-Si multilayer substrate occurs for z < 0 Å (not shown) while the nSLD profile for the KvAP-POPC membrane occurs within the interval 30 Å < z < 110 Å with the membrane centroid located at z ~ 75 Å. The nSLD profiles for the membrane appear at negative contrast with respect to the average nSLD of both electrolytes shown in Figure 3.4A (left) for 90% D_2O and in Figure 3.4B (left) for 60% D_2O. The changes in the membrane nSLD profiles for the hyperpolarizing versus the depolarizing
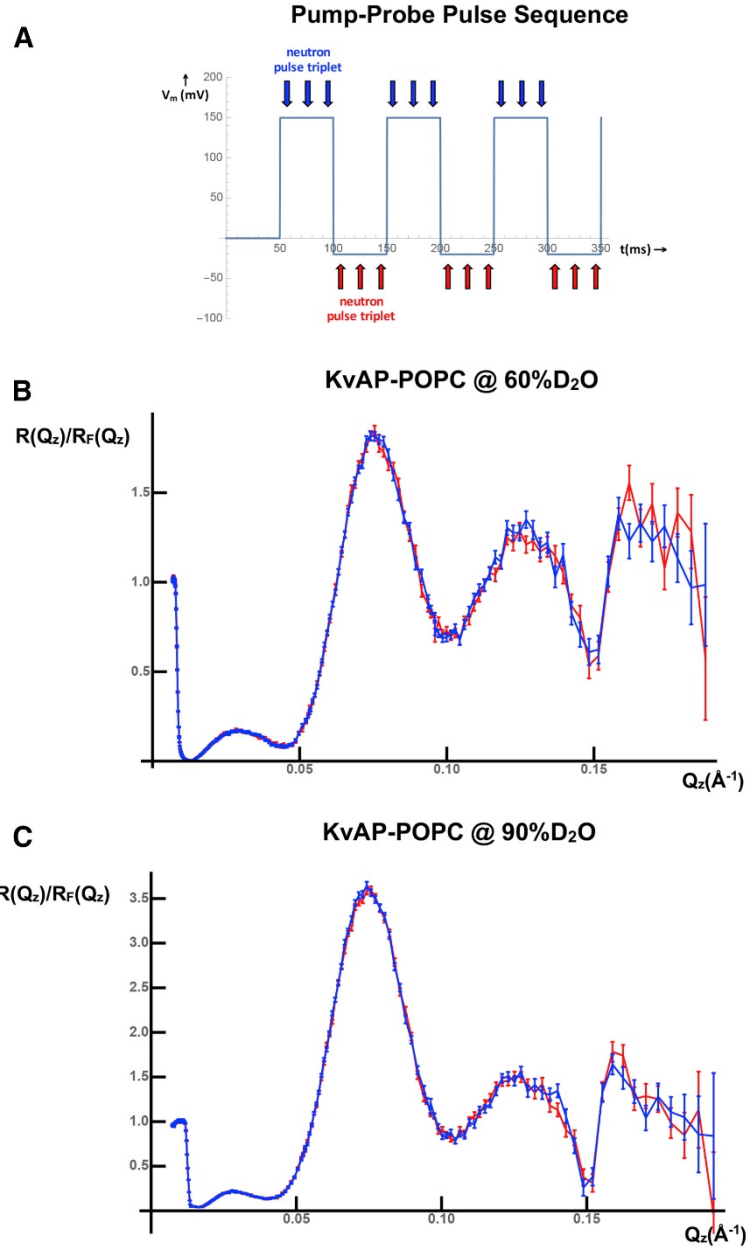
Figure 3.3. Time-resolved ''pump-probe'' neutron interferometry. (A) The cyclic sequence of hyperpolarizing and depolarizing transmembrane voltage pulses, together with the triplet of incident neutron pulses utilized for each voltage (blue hyperpolarizing, red depolarizing), employed in the time-resolved neutron interferometry experiment is shown. (B) Fresnel-normalized neutron reflectivity $R(Q_z)/R_F(Q_z)$, averaged over the hyperpolarizing voltage pulses (blue), is shown compared with that averaged over the depolarizing voltage pulses (red) for the KvAP-POPC membrane of specimen S2 at an aqueous solvent contrast of 60% D_2O/ 40% H_2O. (C) Similar Fresnel-normalized neutron reflectivity $R(Q_z)/R_F(Q_z)$ is shown for the same specimen at a contrast of 90% D2O/10% H2O. The standard errors for each are based on the reflected neutron counting statistics.

59

voltage pulses occur within the interval 65 Å ± 35 Å for both contrasts. In general, they demonstrate a loss of nSLD within the extracellular half of the membrane for $z > 75$ Å and a gain of nSLD within the cytoplasmic half of the membrane for $z < 75$ Å, that exceed the estimated propagated errors, for the deactivated, closed state of the channel (hyperpolarized) relative to the activated, open state (depolarized). The difference ΔnSLD profiles, hyperpolarized minus depolarized, were calculated following superposition of the centroids of the nSLD profiles for the membrane at the maximum contrast provided by 90% D_2O for each transmembrane voltage. This was done so that the small shift in the centroid of the membrane nSLD profile for the hyperpolarizing voltage toward the substrate surface of less than 1 Å relative to that for the depolarizing voltage did not otherwise contribute to the difference ΔnSLD profiles. With this minor adjustment, the difference ΔnSLD profiles manifest the changes noted, as shown in Figure 3.4A (right side) for 90% D2O and in Figure 3.4B (right side) for 60% D_2O and while the changes are similar for both contrasts, they are larger for 60% D_2O. The difference ΔnSLD profile for the control specimen S1 lacking the KvAP-POPC membrane is nearly featureless on the same ordinate-scale as shown in Figure 3.4C. The horizontal dashed lines above and below the abscissa in Figure 3.4C were used to estimate the propagation of errors from the reflectivity data into the ΔnSLD profiles and the nSLD profiles described in Section 3.2.9. The different magnitudes of the features in the ΔnSLD profiles for the different contrasts arise from H-D exchange for both water and protein within the membrane profile, as POPC possesses no exchangeable hydrogens.

The double difference profile, $\Delta\Delta$nSLD, shown in Figure 3.5 for 90% D_2O minus 60% D_2O and hyperpolarizing minus depolarizing voltages, provides the dependence of the H-D exchange profile on the transmembrane voltage. However, any water-accessible sites within the KvAP protein that might be unexposed for one state (e.g., deactivated, closed) and become exposed for
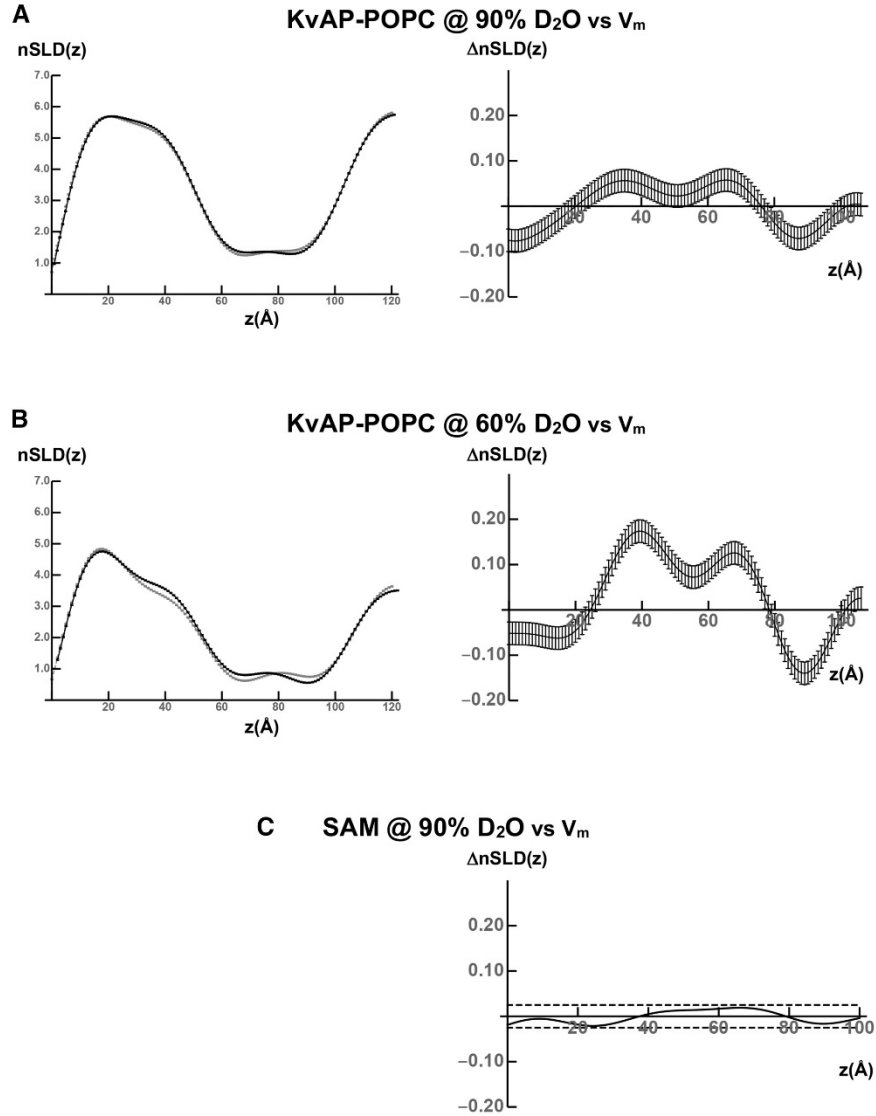
Figure 3.4. Experimental voltage-dependent profile structures for the KvAP-POPC membrane. (A) Left side shows the nSLD(z) profiles for the KvAP-POPC membrane of specimen S2 (black hyperpolarized, gray depolarized) at a solvent contrast of 90% D_2O/10% H_2O. The profile for the membrane is at negative contrast relative to 90% D_2O. (A) Right side shows the difference ΔnSLD(z) profile (hyperpolarized minus depolarized) at the same contrast of 90% D_2O/10% H_2O. (B) Left side shows the nSLD(z) profiles for the same specimen S2 at a contrast of 60% D_2O/40% H_2O. The profile for the membrane is also at negative contrast relative to 60% D_2O. (B) Right side shows the difference ΔnSLD(z) profile (hyperpolarized minus depolarized) at the same contrast of 60% D_2O/40% H_2O. (C) Right side shows the ΔnSLD(z) profile (hyperpolarized minus depolarized) for the organic SAM on the inorganic Si-Ge-Si multilayer substrate's surface, but otherwise lacking the tethered KvAP-POPC membrane, for specimen S1 at a solvent contrast of 90% D_2O/10% H_2O. The horizontal dashed lines above and below the abscissa were used to estimate the propagation of errors into the difference ΔnSLD(z) profiles and hence the nSLD(z) profiles contributing to the difference. The nSLD(z) profiles are in units of $10^{-6}/Å^2$.

the other state (e.g., activated, open) would all undergo H-D exchange due to cycling between the hyperpolarizing and depolarizing voltages. Hence, the double difference profile, $\Delta\Delta$nSLD, in Figure 3.5 is that for only water. The double difference profile demonstrates that water is lost from the cytoplasmic half of the membrane for z < 75 Å, especially at the surface of the cytoplasmic side of the membrane at z ~ 35–45 Å, and water is gained within the extracellular half of the membrane for z ~ 85–95 Å, for the deactivated, closed state of the channel (hyperpolarized) relative to the activated, open state (depolarized). In Figure 3.5, the nSLD profiles at 90% D_2O (hyperpolarized and depolarized) are shown in Figure 3.5A juxtaposed above the double-difference profile $\Delta\Delta$nSLD in Figure 3.5B for reference. The error bars in the double-difference profile $\Delta\Delta$nSLD are $\sqrt{2}$ larger than those in the ΔnSLD profiles contributing to the difference described in Section 3.2.9.

Note that any model for the deactivated, closed state of the Kv channel relative to the activated, open state of the channel should predict both the ΔnSLD difference profiles and the $\Delta\Delta$nSLD double-difference profile from these time-resolved neutron interferometry experiments. This is because the experiments are directly sensitive to the voltage dependence of the profile structure of the Kv channel, and to the voltage dependence of water within that profile structure, in these single phospholipid bilayer membranes containing the vectorially oriented channel at high in-plane density. We compare several models for these two states of Kv channels in the sections that follow.
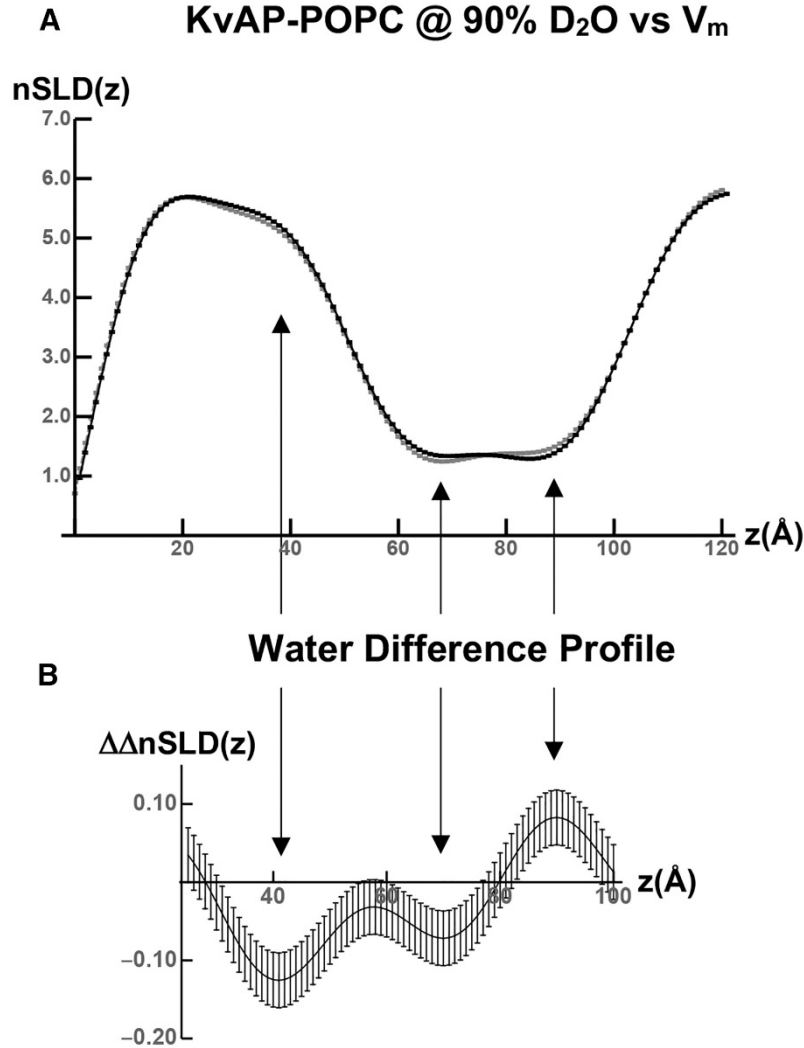
Figure 3.5. Experimental voltage-dependent profile structure for water within the KvAP-POPC membrane. (A) For reference, the nSLD(z) profiles for specimen S2 and an aqueous solvent contrast of 90% D_2O/10% H_2O from Figure 3.4 are shown juxtaposed to better delineate those more relevant regions of the membrane profile exhibiting changes in the ΔnSLD(z) profile for water only (*vertical arrows*). (B) The double-difference $\Delta\Delta$nSLD(z) profile for solvent contrasts of 90% D_2O/10% H_2O minus 60% D_2O/40% H_2O and for hyperpolarizing minus depolarizing transmembrane voltages is shown for specimen S2. The estimated errors in the double-difference $\Delta\Delta$nSLD(z) profile are $\sqrt{2}$ larger than for the ΔnSLD(z) profiles shown in Figure 3.4.

3.3.3 Modeling the nSLD profile for the activated, open state of the KvAP protein within a hydrated POPC bilayer membrane

We first address whether the nSLD profile structure determined for the KvAP-POPC membrane using a depolarizing transmembrane voltage to produce the activated, open state of the channel in our time-resolved neutron interferometry experiments is consistent with what is known about both the high-resolution structure of this Kv channel and the structure of a hydrated POPC bilayer. However, there is no x-ray crystal structure for a properly folded KvAP protein in the activated, open state. Instead, there is a model[31] based on a proposed structural homology for KvAP with the transmembrane domain of Kv1.2 determined by x-ray crystallography[8] employing a more "membrane-like" crystallization environment, as described in Section 3.3.1. In Supporting Materials, Section c, we describe the construction of an improved model for this state of KvAP based on the result that the isolated VSD of KvAP was shown to undergo a substantial conformational change for depolarizing transmembrane voltages compared with the absence of a voltage.[23,24] There are high-resolution x-ray crystal structures for the eukaryotic Kv channels, Kv1.2[8] and the Kv1.2/2.1 chimera,[5] with the highest resolution achieved for the latter. Given the proposed structural homology noted above, we first compare the time-averaged nSLD profile for the transmembrane domain of the Kv1.2/2.1 chimera protein in a hydrated POPC bilayer under a depolarizing transmembrane voltage from the MD simulation,[18] as described in Supporting Materials, Section c. We then compare the time-averaged nSLD profile for the improved model for KvAP in a hydrated POPC bilayer environment under a depolarizing transmembrane voltage in a MD simulation also described in Supporting Materials, Section c.
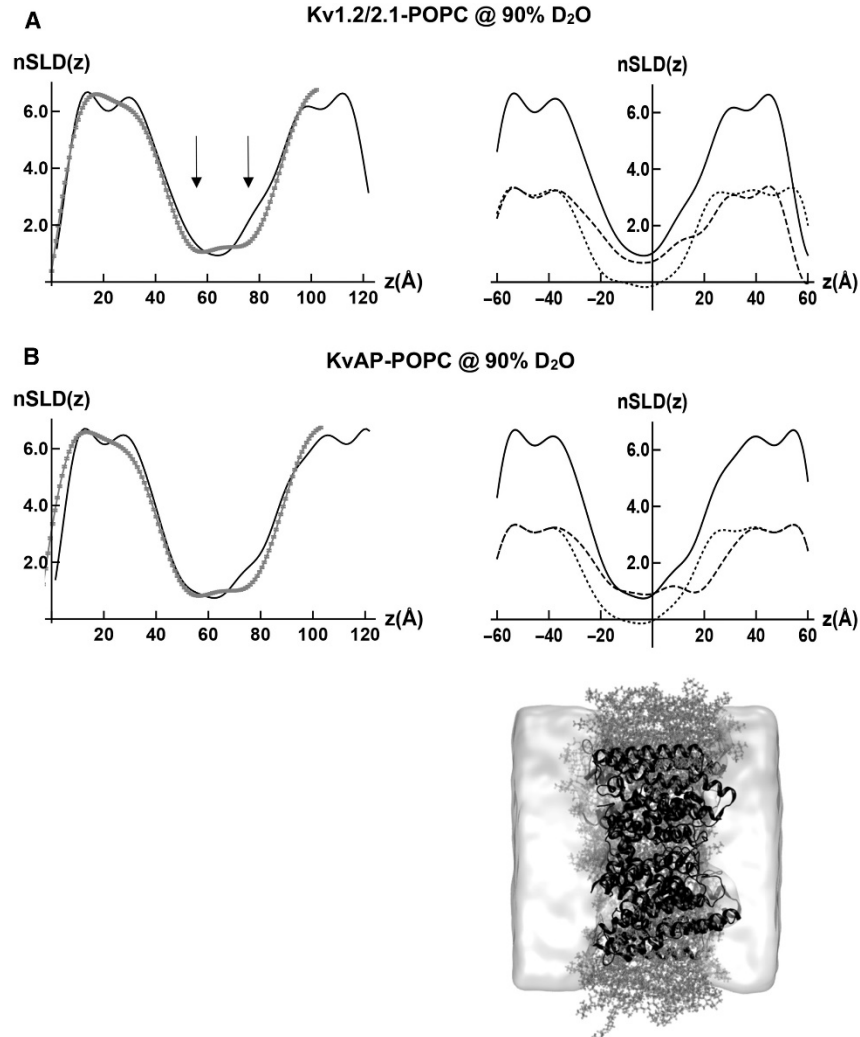
Figure 3.6. Modeling the nSLD profile for the activated, open state of KvAP in a hydrated POPC bilayer membrane. The nSLD profiles for the membranes in (A) and (B) are at negative contrast relative to 90–100% D_2O. (A) Left side shows the experimental nSLD(z) profile for the KvAP-POPC membrane at a contrast of 90% D_2O / 10% H_2O (*gray*) compared with that of the resolution-limited model based on MD simulation for the Kv1.2/2.1 chimera channel within a hydrated, POPC bilayer at a contrast of 100% D_2O (*black*) at twice the spatial resolution of the experimental profile. The two arrows point out the ''double-well'' shape of the experimental nSLD(z) profile. (A) Right side shows the separate contributions of the Kv1.2/2.1 protein (dashed) and the POPC bilayer (*dotted*) in 100% D_2O to the model profile and their sum (*solid*). (B) Left side shows the experimental nSLD(z) profile for the KvAP-POPC membrane at a contrast of 90% D_2O/10% H_2O (*gray*) compared with that of the resolution-limited model based on MD simulation of an improved model for this state of the KvAP channel within a hydrated, POPC bilayer at a contrast of 100% D_2O (*black*) at twice the spatial resolution of the experimental profile. (B) Right side shows the separate contributions of the KvAP protein (*dashed*) and the POPC bilayer (*dotted*) in 100% D_2O to the model profile, and their sum (solid). Juxtaposed below, we show to scale a rendering of an instantaneous configuration of the KvAP protein (black ribbon) embedded with the POPC bilayer (gray licorice) in a water slab (white shaded) from the MD simulation of the improved model for this state of the KvAP channel.

In Figure 3.6A, the left-side panel compares the time-averaged, resolution-limited nSLD profile of the activated, open state for the Kv1.2/2.1 chimera, based on the MD simulation within a hydrated POPC bilayer, with the experimental nSLD profile for the KvAP-POPC membrane at a depolarizing transmembrane voltage. The nSLD profile for the Kv1.2/2.1 chimera within a hydrated POPC bilayer was adjusted to match the lipid-to-protein mole ratio of the experiment. The right-side panel shows the separate resolution-limited nSLD profiles for both the Kv1.2/2.1 chimera protein and the POPC bilayer in D_2O, as well as their sum. In Figure 3.6B, the left-side panel compares the time-averaged, resolution-limited nSLD profile for the activated, open state of the KvAP protein, based on the MD simulation of the improved model within a hydrated POPC bilayer, with the experimental nSLD profile for the KvAP-POPC membrane at a depolarizing transmembrane voltage. The right-side panel shows the separate resolution-limited nSLD profiles for both the KvAP protein and the POPC bilayer in D_2O, as well as their sum.

In Figure 3.6B, the time-averaged, resolution-limited nSLD profile for the activated, open state of the KvAP protein within a hydrated POPC bilayer appears to be in reasonable agreement with the "double well" geometric shape of the experimental nSLD profile for the KvAP-POPC membrane at a depolarizing transmembrane voltage. In Figure 3.6A, there is slightly less agreement between the time-averaged, resolution-limited nSLD profile for the activated, open state of the Kv1.2/2.1 chimera protein within a hydrated POPC bilayer and the "double well" geometric shape of the experimental nSLD profile for the KvAP-POPC membrane at a depolarizing transmembrane voltage. This is not surprising based on the structural homology between the two proteins. For both the Kv1.2/2.1 chimera in Figure 3.6A and KvAP in Figure 3.6B, the more detailed features provided by the somewhat higher spatial-resolution of the nSLD profiles for the models predict that the deeper minimum of the "double well" geometric shape occurs within the cytoplasmic half

of the membrane, as exhibited by the experimental nSLD profile, but to a lesser extent. Note that the separate nSLD profiles for the host POPC bilayer component are very similar while the nSLD profiles for the protein component are more different, as shown in the right-side panels. Thus, any differences in the nSLD profiles for their respective membranes arise from the protein component. Lastly, if the spatial resolution in the resolution-limited nSLD profiles is reduced to approach that of the experimental profiles, the "double well" geometric shape exhibited by the experimental profile is reproduced.

3.3.4 Modeling the difference ΔnSLD profiles between the deactivated, closed state and activated, open state of the KvAP protein within a hydrated POPC bilayer membrane

We next address whether any of the three fundamentally different computational approaches to modeling the deactivated, closed state and the activated, open state of a Kv channel mentioned in Section 3.1 can predict the experimental difference ΔnSLD profiles for the KvAP protein within a hydrated POPC bilayer membrane. Like for the experimental KvAP-POPC membrane, the difference ΔnSLD profiles described below were all calculated as the nSLD profile for the deactivated, closed state minus that for the activated, open state, following the superposition of the membrane centroids for each state of the respective Kv channel. Furthermore, the difference ΔnSLD profiles for each of the three models were calculated from their respective MD simulations described in Supporting Materials, Section c, and smoothed via convolution with a Gaussian function ($\sigma = 5$ Å).
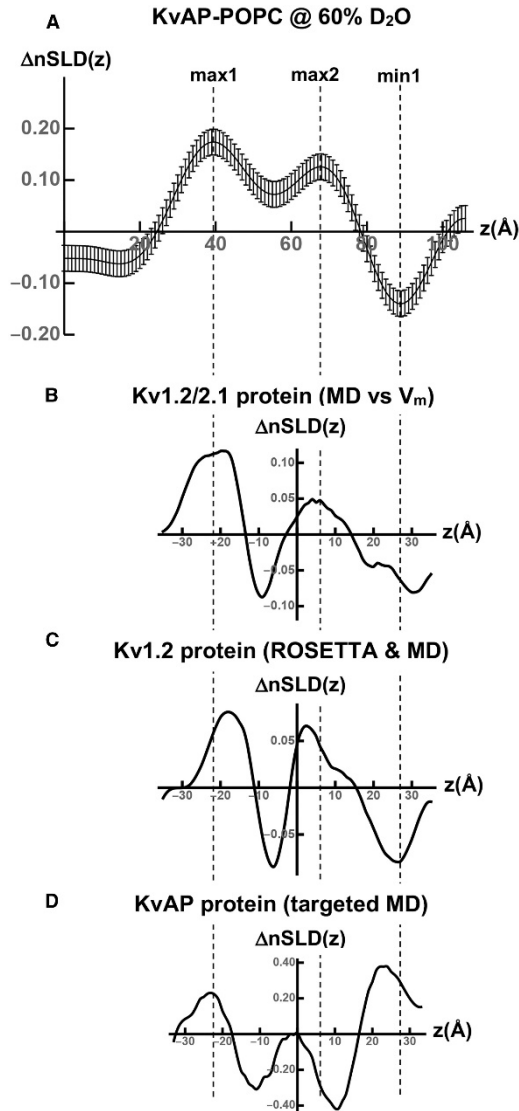
Figure 3.7. Modeling the difference ΔnSLD profile between the deactivated, closed and activated, open states of KvAP in a hydrated POPC bilayer membrane. (A) The experimental difference ΔnSLD(z) profile (hyperpolarized – depolarized) for the KvAP-POPC membrane is shown at a contrast of 60% D_2O/40% H_2O from Figure 3.4B with respect to the z ¼ 0 A° origin at the multilayer substrate surface. (B) The difference ΔnSLD(z) profile for the Kv1.2/2.1 protein within a hydrated POPC bilayer membrane is shown at a contrast of 60% D_2O/ 40% H_2O with respect to the centroid of the membrane. The difference ΔnSLD(z) profile was calculated from MD simulations that utilized transmembrane voltages (V_m) to generate the deactivated, closed and activated, open states. (C) The difference ΔnSLD(z) profile for the Kv1.2 protein within a hydrated POPC bilayer membrane is shown at a contrast of 60% D_2O/40% H_2O with respect to the centroid of the membrane. The difference ΔnSLD(z) profile was calculated from the MD simulations of ROSETTA models for the deactivated, closed and activated, open states. (D) The difference ΔnSLD(z) profile for the KvAP protein within a hydrated POPC bilayer membrane is shown at a contrast of 60% D_2O/40% H_2O with respect to the centroid of the membrane. The difference ΔnSLD(z) profile was calculated from targeted MD simulations to generate the deactivated, closed and activated, open states. The vertical dashed lines serve only to guide the eye.

In Figure 3.7A, we show the difference ΔnSLD profile from the experiment for the KvAP-POPC membrane, with respect to the z = 0 Å origin at the substrate surface, for an aqueous solvent contrast of 60% D_2O. We chose the higher contrast for this comparison because the signal/noise level is higher than for 90% D_2O, and the following difference ΔnSLD profiles for the models are shown at the same contrast (60% D_2O). In Figures 3.7B–D we show the difference ΔnSLD profiles for only the Kv1.2/2.1 chimera protein, for only the Kv1.2 protein, and for only the KvAP protein, respectively. In all of the ΔnSLD profiles for only the Kv channel proteins, the z = 0 Å origin is at the membrane centroid.

There are three main features evident in the experimental difference ΔnSLD profile for the KvAP-POPC membrane shown in Figure 3.7A, namely the two maxima (max1, max2) and the minimum (min1) spanning ~70 Å of the membrane profile. These three features are very similar to those exhibited by the Kv1.2/2.1 chimera protein in Figure 3.7B and the Kv1.2 protein in Figure 3.7C, each spanning ~70 Å of their simulated membrane profile. The only exception is that the minimum between the two maxima within the cytoplasmic half of the membrane for the Kv1.2/2.1 and Kv1.2 proteins is much deeper than for the experimental KvAP-POPC membrane. This difference vanishes when the ΔnSLD profiles for the Kv1.2/2.1 and Kv1.2 proteins are convoluted with a broader Gaussian (e.g., σ ~ 10 Å) that matches the spatial-resolution of the experimental ΔnSLD profile for the KvAP-POPC membrane. The similarity noted comparing the difference ΔnSLD profiles for only the protein components of the simulated membranes for Kv1.2/2.1 and Kv1.2 suggests that the experimental difference ΔnSLD profile for the KvAP-POPC membrane is dominated by its protein component. However, despite utilizing an improved model for the activated, open state of the KvAP protein, the major features in the difference ΔnSLD profile for

only the protein in Figure 3.7D differ substantially from those for the experimental KvAP-POPC membrane in Figure 3.7A, especially within the extracellular half of the membrane.

With respect to the three main features in the experimental difference ΔnSLD profile in Figure 3.7A, the larger maximum occurs near the cytoplasmic surface of the membrane separated from a second maximum within the cytoplasmic half of the membrane by 28 Å while the minimum occurs within the extracellular half of the membrane separated from the first maximum by 50 Å. The two separations of these three main features are the only unique attributes of the experimental ΔnSLD profile. It is notable that the ΔnSLD profiles for both the simulated Kv1.2/2.1 chimera protein and the simulated Kv1.2 protein within their respective POPC bilayer membranes exhibit the same three features, namely two maxima and one minimum that span their respective membrane profiles. As can be seen in Table 3.1, in which the separations noted utilize the centroids of the features, the two unique separations for the ΔnSLD profile of the Kv1.2/2.1 chimera protein match those of the KvAP protein to within less than 1 Å. However, the two unique separations for the ΔnSLD profile of the Kv1.2 protein are 6–8 Å smaller than for the KvAP protein. Thus, the question arises as to whether our time-resolved neutron interferometry experiments could have detected these smaller separations given the relatively low spatial-resolution of the experimental nSLD profiles for the KvAP-POPC membrane at hyperpolarizing and depolarizing transmembrane voltages. The answer is "yes", as is demonstrated in Supporting Materials, Section d.

Table 3.1. Separations between Features in the ΔnSLD Profiles

	Exp. ΔnSLD KvAP	ΔnSLD Kv1.2/2.1	ΔnSLD Kv1.2
$|\Delta(\text{max1} - \text{max2})|$	28 Å	28 Å	20 Å
$|\Delta(\text{max1} - \text{min1})|$	50 Å	51 Å	44 Å

3.3.5 Modeling the difference ΔnSLD profile for water between the deactivated, closed state and activated, open state of the KvAP protein within a hydrated POPC bilayer membrane

Lastly, we address whether any of the three fundamentally different computational approaches to modeling the deactivated, closed state and the activated, open state of a Kv channel mentioned in Section 3.1 can predict the experimental difference ΔnSLD profile for water within the KvAP protein in a hydrated POPC bilayer membrane. Like for the experimental KvAP-POPC membrane, the difference ΔnSLD profiles for water described below were calculated as the nSLD profile water for the deactivated, closed state minus that for the activated, open state, following the superposition of the membrane centroids for each state of the respective Kv channel. Furthermore, the difference ΔnSLD profiles for water in each of the three models were calculated from their respective MD simulations described in Supporting Materials, Section c, and smoothed via convolution with a Gaussian function (σ = 5 Å).

In Figure 3.8A, we show the experimental difference ΔnSLD profile for water within the KvAP-POPC membrane, namely the double difference ΔΔnSLD profile from Figure 3.5B. In Figure 3.8B, we show the difference ΔnSLD profile for water within the transmembrane domain of the Kv1.2/2.1 protein within a hydrated POPC bilayer. The agreement between the experimental and simulated difference nSLD profiles for water is seen to be very good, particularly with regard to both the amplitudes and signs of their major features, corresponding to the loss of water from the cytoplasmic half of the membrane, nearer the membrane surface, and the gain of water within the extracellular half of the membrane, nearer the membrane surface. They differ somewhat within the interior region of the membrane profile structure in between the two membrane surfaces, with
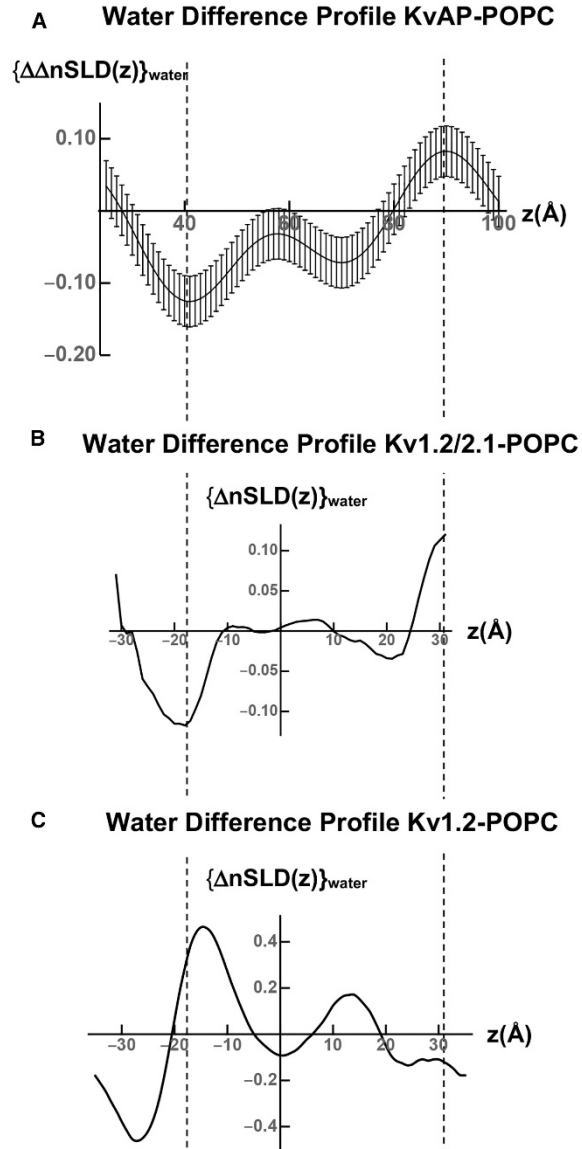
Figure 3.8. Modeling the difference ΔnSLD profile for water between the deactivated, closed and activated, open states of KvAP within a hydrated POPC bilayer membrane. (A) Experimental double-difference ΔΔnSLD(z) profile for water within the experimental KvAP-POPC membrane from Figure 3.5B is shown. (B) The difference ΔnSLD(z) profile for water within the simulated Kv1.2/2.1-POPC membrane shown here with respect to the centroid of the nSLD profile for the membrane is shown. (C) The difference ΔnSLD(z) profile for water within the simulated Kv1.2-POPC membrane shown here with respect to the centroid of the nSLD profile is shown. The vertical dashed lines serve only to guide the eye.

some water being lost from the interior region for KvAP versus essentially none for the transmembrane domain of the Kv1.2/2.1 chimera. In Figure 3.8C, we show the difference ΔnSLD profile for water within the Kv1.2-POPC membrane. In this case, the difference ΔnSLD profile for water within the Kv1.2-POPC membrane bears no resemblance to that for the experimental KvAP-POPC membrane in terms of both amplitudes and signs of their respective features.

3.3 Discussion

We chose to focus this investigation on the activated, open state and the deactivated, closed state of the prokaryotic KvAP channel, the endpoints of the electromechanical coupling mechanism in which all four VSDs of each channel in the ensemble are in the same fully activated or fully deactivated state. Intermediate states are also thought to play a role in the mechanism.[3] Such intermediates can arise when some fraction of the four VSDs within each channel of the ensemble are either activated or deactivated. They can also arise when the VSDs are only partially activated or deactivated, with the translation of the S4 helices within the VSDs at some fraction of the maximal translation between the endpoints, e.g., 1/4, 1/2, or 3/4. We sought to avoid such intermediate states by utilizing depolarizing and hyperpolarizing transmembrane voltages whose amplitudes and duration were not only sufficient to circumvent inactivation, but also sufficient to attain either full activation or deactivation of all four VSDs within each channel of the ensemble. The agreement achieved, as described in the next paragraph, suggests that we were successful.

The ΔnSLD profile for the Kv1.2/2.1 chimera protein from the MD simulations of reference (18), contains the effects of both a relatively large inward translation of the S4 helix within the VSDs of ~15 Å along the membrane profile, toward the cytoplasmic side of the membrane, and the closing of the channel of the PD in response to the hyperpolarizing transmembrane voltage. We

found that the large inward translation of the S4 helix within the VSDs actually dominates the ΔnSLD profile over almost its full extent for the Kv1.2/2.1 protein, except for the extreme cytoplasmic side of the profile where changes in the PD near the C-terminus of the S6 helices also make a contribution. In these simulations, the hyperpolarizing voltage was much larger than in our experiments which could have contributed to the magnitude of this translation of the S4 helices.[2] The agreement in terms of both the amplitudes and positions of the major features within the experimental ΔnSLD profile for the KvAP-POPC membrane and those in the ΔnSLD profile for the Kv1.2/2.1 chimera protein itself from the MD simulation is seen to be very good in Figure 3.7, as quantified in Table 3.1. Although the major features in the difference ΔnSLD profile for the Kv1.2 protein in Figure 3.7C are qualitatively similar to those for both the Kv1.2/2.1 chimera protein in Figure 3.7B and for KvAP within the KvAP-POPC membrane in Figure 3.7A, the separations between the three features are 6–8 Å less for the Kv1.2 protein, using the vertical dashed lines as guides in Figure 3.7, and as quantified in Table 3.1. It is noteworthy in this regard that the ΔnSLD profile from the simulation for the Kv1.2 protein contains the effects of both a smaller inward translation of the S4 helix within the VSDs of ~7 Å along the membrane profile, toward the cytoplasmic side of the membrane, and the closing of the channel within the PD.[10] As for the Kv1.2/2.1 protein chimera, we found that the smaller inward translation of the S4 helix within the VSDs also dominates the ΔnSLD profile over almost its full extent for the Kv1.2 protein. The differences in the separations of the main features in the difference ΔnSLD profiles for the Kv1.2/2.1 chimera protein versus the Kv1.2 protein noted above indicate the sensitivity of these difference ΔnSLD profiles to the magnitude of the translation of the S4 helix within the VSDs. Importantly, our time-resolved neutron interferometry experiments would have been capable of detecting such a smaller translation of the S4 helix within the VSDs of ~7 Å were it to have

occurred in the experimental KvAP-POPC membrane despite the relatively low spatial resolution of the experiment.

Based on the comparisons of the experimental DnSLD profile with those for the models of the Kv1.2/2.1 chimera and Kv1.2 noted in the preceding paragraph, our time-resolved neutron interferometry experiments demonstrate directly that the magnitude of the inward translation of the S4 helix upon the transition between the activated, open state and the deactivated, closed state is ~15 Å for KvAP. The magnitude of the translation associated with this transition for Kv channels has been controversial in the past as reviewed in reference (3), possibly due to the investigation of different channels in differing environments coupled with the indirect techniques utilized. Nevertheless, there are several such experiments that support a translation of this relatively large magnitude.[14,33–35]

3.4 Conclusion

We have demonstrated good agreement between the difference ΔnSLD profile (hyperpolarized minus depolarized) for the experimental KvAP-POPC membrane from our time-resolved neutron interferometry experiments and that for the transmembrane domain of the Kv1.2/2.1 chimera protein embedded within a hydrated POPC bilayer from the MD simulations of reference (18). This agreement indicates that the inward translation of the S4 helices within the VSDs of KvAP upon the transition between the activated, open state and the deactivated, closed state is ~15 Å along the membrane profile. We have also demonstrated good agreement between the difference ΔnSLD profile for water within the experimental KvAP-POPC membrane and that for water within the transmembrane domain of the Kv1.2/2.1 chimera protein. Thus, there is a "de-wetting" of the cytoplasmic half of the pore within the PD of KvAP associated with this transition like that

predicted from the MD simulations of the Kv1.2/2.1 chimera. The other two fundamentally different computational approaches for modeling these same two states in hydrated phospholipid bilayer membranes were unable to provide agreement with both of these two key results from our time-resolved neutron interferometry experiments.

3.5 Bibliography

1. Hodgkin, A. L. The ionic basis of electrical activity in nerve and muscle. *Biol. Rev*. 26, 339-409 (1951).

2. Vargas, E., Yarov-Yarovoy, V., Khalili-Araghi, F., Catterall, W. A., Klein, M. L., Tarek, M., Lindahl, E., Schulten, K., Perozo, E., Bezanilla, F. & Roux, B. An emerging consensus on voltage-gating from computational modeling and molecular dynamics simulations. *J. Gen. Physiol*. 140(6), 587–594 (2012).

3. Grizel, A. V., Glukov, G. S. & Sokolova, O. S. Mechanisms of activation of voltage gated potassium channels. *Acta Naturae* 6(4), 10–26 (2014).

4. Hodgkin, A. L. &Huxley. A. F. A quantitative description of membrane current and its application to conduction and excitation in nerve. *J. Physiol*. 117, 500–544 (1952).

5. Long, S. B., Tao, X., Campbell, E. B. & MacKinnon, R. Atomic structure of a voltage-dependent K^+ channel in a lipid membrane-like environment. *Nature* 450, 376–382 (2007).

6. Payandeh, J., Scheurer, T., Zheng, N. & Catterall, W. A. The crystal structure of a voltage-gated sodium channel. *Nature* 475, 353-358 (2011).

7. Matthies, D., Bae, C., Toombes, G. ES., Fox, T., Bartesaghi, A., Subramaniam, S. & Swartz, K. J. Single-particle cryo-EM structure of a voltage-activated potassium channel in lipid nanodiscs. *eLife* 7, e37558 (2018).

8. Long, S. B., Campbell, E. B. & MacKinnon, R. Crystal structure of a mammalian voltage-dependent Shaker family K^+ channel. *Science* 309, 897-902 (2005).

9. Yarov-Yarovoy, V., Baker, D. & Catterall, W. A. Voltage sensor conformations in the open and closed states in ROSETTA structural models of K^+ channels. *Proc. Natl. Acad. Sci. U. S. A.* 103(19), 7292-7297 (2006).

10. Pathak, M. M., Yarov-Yarovoy, V., Agarwal, G., Roux, B., Barth, P., Kohout, S., Tombola, F. & Isacoff, E. Y. Closing in on the resting state of the Shaker K^+ channel. *Neuron* 56, 124-140 (2007).

11. Khalili-Araghi, F., Jogini, V., Yarov-Yarovoy, V., Tajkhorshid, E., Roux, B. & Schulten, K. Calculation of the gating charge for the Kv1.2 voltage-activated potassium channel. *Biophys. J*. 98, 2189-2198 (2010).

12. Schow, E. V., Freites, J. A., Gogna, K., White, S. H. & Tobias, D. J. Down-state model of the voltage-sensing domain of a potassium channel. *Biophys. J*. 98, 2857-2866 (2010).

13. Schow, E. V., Freites, J. A., Nizkorodov, A., White, S. H. & Tobias, D. J. Coupling between the voltage-sensing and pore domains in a voltage-gated potassium channel. *Biochimica et Biophysica Acta* 1818, 1726-1736 (2012).

14. Henrion, U., Renhorn, J., Börjesson, S. I., Nelson, E. M., Schwaiger, C. S., Bjelkmar, P., Wallner, B., Lindahl, E. & Elinder, F. Tracking a complete voltage-sensor cycle with metal-ion bridges. *Proc. Natl. Acad. Sci. U. S. A.* 109(22), 8552-8557 (2012).

15. Treptow, W., Tarek, M. & Klein, M. L. Initial response of a potassium channel voltage sensor to a transmembrane potential. *J. Am. Chem. Soc*. 131, 2107-2109 (2009).

16. Denning, E. J., Crozier, P. S., Sachs, J. N. & Woolf, T. B. From the gating charge response to pore domain movement: initial motions of Kv1.2 dynamics under physiological voltage changes. *Mol. Membr. Biol*. 26, 397-421 (2009).

17. Delemotte, L., Tarek, M., Klein, M. L., Amaral, C. & Treptow, W. Intermediate states of the Kv1.2 voltage sensor from atomistic molecular dynamics simulations. *Proc. Natl. Acad. Sci. U. S. A.* 108, 6109-6114 (2011).

18. Jensen, M. Ø., Jogini, V., Borhani, D. W., Leffler, A. E., Dror, R. O. & Shaw, D. E. Mechanism of voltage gating in potassium channels. *Science* 336, 229-233 (2012).

19. Gupta, S., Liu, J., Strzalka, J. & Blasie, J. K. Profile structures of the VSD and KvAP channel vectorially-oriented in single membranes at solid-vapor or solid-liquid interfaces via x-ray reflectivity. *Phys. Rev. E* 84(3), 031911-1-15 (2011).

20. Blasie, J. K. 2018. Chapter Four - Time-Resolved Neutron Interferometry and the Mechanism of Electromechanical Coupling in Voltage-Gated Ion Channels. In Methods in Enzymology vol. 603. Chemical and Biochemical Approaches for the Study of Anesthetic Function Part B. R.G. Eckenhoff and I.J. Dmochowski, editors. Elsevier/Academic Press, Oxford, pp. 67-90.

21. Gupta, S., Dura, J., Freites, J. A., Tobias, D. J. & Blasie, J. K. Structural characterization of the voltage sensor domain and voltage-gated K^+-channel proteins vectorially-oriented within a single bilayer membrane at the solid/vapor and solid/liquid interfaces via neutron interferometry. *Langmuir* 28(28), 10504-10520 (2012).

22. Krishnan, V., Strzalka, J., Liu, J., Liu, C., Kuzmenko, I., Gog, T. & Blasie, J. K. Interferometric enhancement of x-ray reflectivity from unperturbed Langmuir monolayers of amphiphiles at the liquid-gas interface. *Phys. Rev. E* 81, 021604-1-10 (2010).

23. Tronin, A. Y., Nordgren, E., Strzalka, J. W., Kuzmenko, I., Worcester, D. L., Lauter, V., Freites, J. A., Tobias, D. J. & Blasie, J. K. Direct evidence of conformational changes associated with voltage gating in a voltage sensor protein by time-resolved x-ray/neutron interferometry. *Langmuir* 30(16), 4784-4796 (2014).

24. Freites, J. A., Schow, E. V., White, S. H. & Tobias, D. J. Microscopic Origin of Gating Current Fluctuations in a Potassium Channel Voltage Sensor. *Biophys. J.* 102, L44-L46 (2012).

25. Schmidt, D., Cross, S. R. & MacKinnon, R. A gating model for the Archeal voltage-dependent K^+ channel in DPhPC and POPE:POPG-decane lipid bilayers. *J. Mol. Biol.* 390(5), 902-912 (2009).

26. Weeks, S. D., Drinker, M. & Loll, P. J. Ligation independent cloning vectors for expression of SUMO fusions. *Prot. Expr. and Purif.* 53, 40-50 (2007).

27. Eriks, L. R., Mayor, J. A. & Kaplan, R. S. A strategy for identification and quantification of detergents frequently used in the purification of membrane proteins. *Anal. Biochem.* 323, 234-241 (2003).

28. Lauter, V., Ambaye, H., Goyette, R., Lee, W.-T.H. & Parizzi, A. Highlights from the magnetism reflectometer at the SNS. *Physica B* 404, 2543-2546 (2009).

29. Kneller, L. R., Edwards, A. M., Majkrzak, C. F., Berk, N. F., Krueger, S. & Blasie, J. K. Hydration state of a single cytochrome c monolayer vectorially-oriented at a soft interface investigated via neutron interferometry. *Biophys. J.* 80(5), 2248-2261 (2001).

30. Jiang, Y., Lee, A., Chen, J., Ruta, V., Cadene, M, Chait, B. T. & MacKinnon, R. X-ray structure of a voltage-dependent K^+ channel. *Nature* 423, 33-41 (2003).

31. Lee, S.-Y., Lee, A., Chen, J. & MacKinnon, R. Structure of the KvAP voltage-dependent K^+ channel and its dependence on the lipid membrane. *Proc. Nat. Acad. Sci. U. S. A.* 102, 15441-15446 (2005).

32. Lu, Y., Lerner, M. B., Qi, Z. J., Mitala Jr., J. J., Lim, J. H., Discher, B. M. & Johnson, A. T. C. Graphene-protein bioelectronic devices with wavelength-dependent photo-response. *Appl. Phys. Lett.* 100, 033110-1-3 (2012).

33. Jiang, Y., Ruta, V., Chen, J., Lee, A. & MacKinnon, R. The principle of gating charge movement in a voltage-dependent K^+ channel. *Nature* 423, 42-48 (2003).

34. Ruta, V., Chen, J. & MacKinnon, R. Calibrated measurement of gating-charge arginine displacement in the KvAP voltage-dependent K^+ channel *Cell* 123, 463-475 (2005).

35. Tao, X., Lee, A., Limapichat, W., Dougherty, D. A. & MacKinnon, R. A gating charge transfer center in voltage sensors. *Science* 328, 67-73 (2010).

Chapter 4

Anomalous diffusion of peripheral membrane signaling-proteins from long Molecular Dynamics simulations

4.1 Background

The key steps for a variety of cell signaling processes include the binding of a membrane-associated protein to the lipid bilayer followed by 2-dimensional diffusion along the membrane. By reducing the diffusion from 3-D to 2-D, this binding can increase the rate at which signaling partners associate, and hence play a vital role in regulating the activity of signaling complexes.[1] In order to better understand how the diffusion of such proteins would rely on the binding mechanism, we looked at two distinct membrane-binding domains, the C2 domain and pleckstrin homology or PH domain.

The C2 domain that we consider is a 121-residue domain from cytosolic phospholipase A2 (cPLA2-C2),[2] which binds to phosphatidylcholine-rich membranes in response to a secondary messenger calcium signal and is important in a variety of eukaryotic signaling pathways. Crystallographic studies of the C2 domain have revealed important structural information, mainly that it is constructed of an eight-strand anti-parallel β-sandwich with three negatively charged calcium-binding-loops (or CBLs) that bind the secondary messenger Ca^{2+} ions and promote membrane association.[3,4] Recent experimental[5,6] and computational studies[7] have elucidated important insights into how the C2 domain induces its docking site and is oriented when bound to a palmitoyloleoylphosphatidyl-choline (POPC) bilayer.
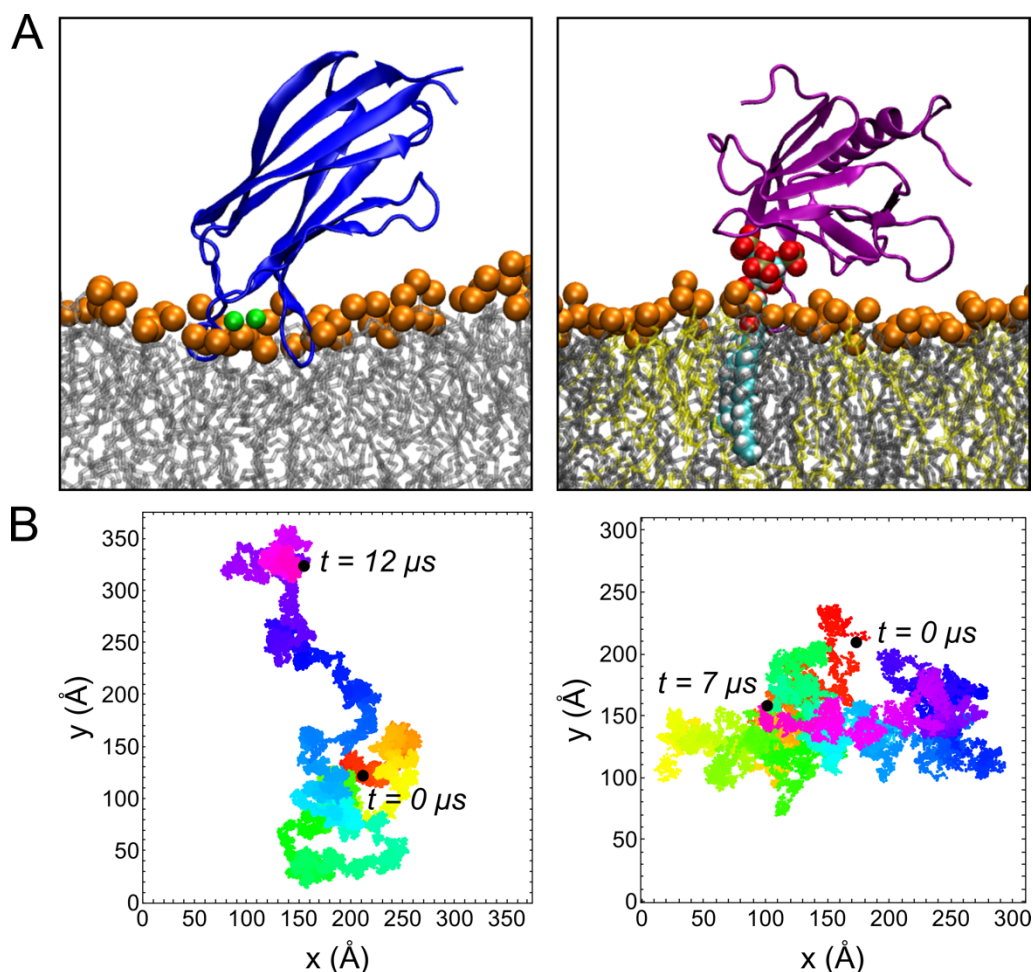
Figure 4.1. Peripheral membrane protein trajectories. (A) The system snapshots for the C2 domain in a POPC bilayer (*left*) showing the protein in blue with cartoon representation and the bound calcium ions in green. The calcium binding loops protrude into the phosphate headgroups of the POPC lipid molecules. The snapshot for the PH domain in a mixed bilayer (*right*) shows the protein in purple and the binding DPPI lipid as spheres colored by atom type: O is red, P is brown, C is cyan, H is white. For both snapshots, the lipid phosphorus atoms are shown as orange spheres to delineate the headgroup region of the membrane while the POPC lipid tails are represented as grey chains and POPS as yellow chains. (B) The trajectories for the protein centers-of-mass projected onto the membrane plane for the C2 domain (*left*) and PH domain (*right*). The color represents the time of the trajectory from the beginning in red to the end in violet.

In contrast to the C2 domain, the PH domain binds to the membrane through transiently appearing phosphatidylinositol-phosphate (PIP) lipids.[8,9] In this work, we look at the triphosphate (PIP$_3$) binding PH domain from the General Receptor for Phosphoinositides 1 (GRP1). Through a combination of crystal structures bound to PIP headgroup analogues[10] and electron paramagnetic resonance (EPR) studies,[11] it was determined that the PH domain rests on the surface of the bilayer,

unlike the C2 domain, which is more deeply embedded. Computational studies have provided support for this binding geometry and insight into how the PH domain hops along the bilayer to encounter the relatively rare PIP lipids.[12,13]

While the PH and C2 domains bind to membranes in very different fashions, as seen in Figure 4.1A, once bound to the bilayer each protein will begin to diffuse along the bilayer until it encounters a partner to propagate the signal. Recent experimental work has begun to shed light on the differing ways that the C2 and PH domains diffuse.[1,14] Techniques such as total internal reflection fluorescence (TIRF) microscopy can track fluorescent labels on proteins to study their diffusion. The GRP1-PH domain in a supported POPC/PIP$_3$ bilayer, was found to have a diffusion constant of D = 2.5 μm^2/s,[14] which is about twice the value measured for the embedded cPLA2-C2 domain on a supported POPC bilayer of D = 1.5 μm^2/s.[1] The diffusion constants of the PH and C2 domains are, respectively, about 3.4 and 5.7 times smaller than the value measured for a single lipid molecule in a POPC bilayer, D = 8.6 μm^2/s.[15]

The diffusion constants of labelled proteins bound to the lipid bilayer or of other membrane components can provide information about the rate at which they traverse the membrane surface. Another interesting aspect is the classification of the 2-D diffusion itself. The molecular details of the surrounding environment can often affect the movement of the particle of interest. A useful quantity for describing diffusion is the mean squared displacement (MSD) of the tracked particle,

$$\langle \mathbf{r}^2(t) \rangle = \frac{1}{N} \sum_{n=1}^{N} \left(\mathbf{r}_n(t) - \mathbf{r}_n(0) \right)^2 = 2dDt \qquad (4.1)$$

where N is the number of particles, d is the dimensionality of the diffusion, and D is the diffusion constant. This equation describes normal Brownian motion. When the MSD deviates from this linear behavior and instead follows a power-law relation in time, the diffusion is anomalous:

$$\langle \mathbf{r}^2(t) \rangle \sim K_\alpha t^\alpha \tag{4.2}$$

For an exponent α greater than 1, the process is superdiffusive. When the exponent α is between 0 and 1, the behavior is called subdiffusion.

Anomalous diffusion has been observed for both the C2 domain and PH domain. A single-particle tracking study was performed using the C2 domain from the synaptotagmin-7 membrane trafficking protein on a supported 3:1 phosphatidylcholine (PC) and phosphatidylserine (PS) bilayer, with an Atto-565 label using TIRF microscopy.[16] The analysis revealed superdiffusive motion of the C2 domain during 10-second trajectories with a 50 ms framerate. This behavior was attributed to bulk-mediated jumps, in which the C2 domain unbinds from the membrane and makes a large excursion into the bulk liquid, before quickly rebinding. Such behavior can be modeled by Lévy-flight dynamics,[17] in which the jump lengths between steps have a heavy-tailed distribution.

In another study, microsecond long coarse-grained and atomistic MD simulations were used to generate trajectories for the DAPP1-PH domain on bilayers of various composition, including POPC, POPS, PIP_2, and PIP_3 lipids.[18] During these long simulations, multiple binding and unbinding events were observed and the PH-PIP association displayed a $1/f$ noise, resulting from a power-law residence time and a long-term correlation in the residence times. Furthermore, the MSD of the lipid-bound PH domain displayed subdiffusion on time-scales up to 10 ns, with an exponent of $\alpha \sim 0.5$.

In order to classify the diffusion of two protein signaling domains with different membrane binding mechanisms, we have run multi-microsecond long atomistic molecular dynamics (MD) simulations of the cPLA2-C2 domain and GRP1-PH domain, each bound to the membrane, as well as two bilayer systems, a pure POPC bilayer and a mixed bilayer containing PIP_3 lipids, of matching composition to the bilayers from the protein systems. In both protein simulations, the protein domains remained bound to the membrane for the entire simulation and the orientation closely matched experimental results from EPR and fluorescence measurements. The mean squared displacements of the proteins show subdiffusive behavior on timescales up to 20 ns for the PH domain and 50 ns for the C2 domain, switching over to normal Brownian motion at longer time-scales. Further analysis of the subdiffusion of all four systems suggests that they closely resemble the fractional Brownian motion (FBM) model, as opposed to a continuous-time random walk (CTRW) or a random walk on a fractal (RWF).

4.2 Methods

4.2.1 C2 domain model setup

The C2 domain conformation was taken from the final configuration of the equilibrated MD simulation of Jaud, *et al.*[7] In summary, two 121-residue cPLA2-C2 domain (PDB: 1RLW),[3] each binding two Ca^{2+} ions, were placed onto a bilayer consisting of 1-palmitoyl-2-oleoyl-phosphatidylcholine (POPC), with one protein in each bilayer leaflet. The binding geometry was based on EPR spin label measurements for the cPLA2-C2 domain, including the membrane depth and β-sheet orientation.[5] The MD simulation involved 5 ns of equilibration, followed by the production run of 9 ns with a harmonic constraint on the Ca^{2+} ion position, followed by 8 ns without

constraints. The final configuration from the unconstrained simulation was used as the initial coordinates for this study.

The system presented in this work used only one of the C2 domains, the other was removed and replaced with a pre-built water sphere. This was done so that there would be no interaction between periodic images of the protein and to minimize the size of the system to obtain a longer trajectory. The system size was approximately $94 \times 92 \times 104$ Å^3, containing one C2 domain, 266 POPC lipid molecules distributed equally in the upper and lower leaflet of the bilayer, two Ca^{2+} ions located in the binding pockets from the crystal structure, four Na$^+$ ions to neutralize the charge, and 16,748 TIP3P water molecules, for a total of 87,883 atoms.

To re-equilibrate the system, we used 2000 steps of energy minimization followed by 1 ns of atomistic MD simulation with harmonic constraints on the protein Cα atom positions, using a force constant of 1 kcal/mol/Å^2, and the Ca^{2+} ions, with a force constant of 10 kcal/mol/ Å^2. The system was run for an additional 10 ns with just the Ca^{2+} ion constraints and then slowly released over 1 ns. The unconstrained system was then run for 10 ns of equilibration before being moved to the Anton supercomputer.[19]

4.2.2 PH domain model setup

The PH domain system was equilibrated as previously reported.[20] In summary, the crystal structure of the GRP1 PH domain (PDB: 1FGY)[10] bound to inositol 1,3,4,5-tetraphosphate (IP$_4$) was docked onto a 3:1 molar ratio POPC to 1-palmitoyl-2-oleoyl-phosphatidylserine (POPS) bilayer in excess water using the orientation and depth prescribed by the model of Chen, *et al*.[11] The IP$_4$ moiety from the crystal structure was used to build a modified PIP$_3$ headgroup for a dipalmitoylphosphatidylinositol (DPPI) lipid molecule to act as the binding site, for a final lipid

composition of 75:25:1 POPC:POPS:DPPI. The initial model contained two PH domains, one docked onto each bilayer leaflet. This system was run for 500 ns of atomistic MD.

For this study, one of the PH domain proteins from the final equilibrated conformation was removed and replaced with a pre-built water sphere. The new PH domain system was approximately $73\times128\times120$ Å^3 and consisted of one 126-residue protein, 192 POPC lipid molecules (96 in each leaflet), 64 POPS lipid molecules (32 in each leaflet), and 2 DPPI lipid molecules (one in each leaflet), 76 K$^+$ ions to balance the charge of the bilayer and protein, and 26,655 TIP3P water molecules, for a total of 116,285 atoms. To re-equilibrate the system, we used 2000 steps of energy minimization followed by 1 ns of atomistic MD simulation with harmonic constraints on the protein Cα atom positions, using a force constant of 1 kcal/mol/Å^2 and then slowly released over 1 ns. The unconstrained system was then run for 10 ns of equilibration.

4.2.3 POPC bilayer model setup

The POPC bilayer system was built in VMD.[21] The system size was approximately $93\times94\times104$ Å^3, similar in size to the C2 domain system. It contained 215 POPC lipid molecules (107 and 108 in the upper and lower leaflet of the bilayer, respectively), and 20,328 TIP3P water molecules for a total of 89,794 atoms. This system was minimized for 5000 steps, followed by 1 ns with the lipid head-groups held fixed in the NVT ensemble at 300 K, followed by 10 ns of equilibration in the NPT ensemble at 300 K and 1 bar.

4.2.4 Mixed bilayer model setup

This mixed bilayer system was built as previously reported.[20] It consisted of the same 75:25:1 molar ratio of POPC:POPS:DPPI as the PH domain system. The system size was approximately

$94 \times 94 \times 103$ Å^3 and contained 192 POPC lipid molecules (96 in each leaflet), 64 POPS lipid molecules (32 in each leaflet), and two DPPI lipid molecules (one in each leaflet), 78 K$^+$ ions to neutralize the charge, and 18,827 TIP3P water molecules for a total of 90,699 atoms. This system had been previously equilibrated, so only an additional 5 ns of equilibration in the NPT ensemble at 300 K and 1 bar was performed.

4.2.5 Equilibration simulation details

Equilibration of all four of the systems was performed using NAMD-2.10.[22] Simulations were done in the NPT ensemble at a temperature of 300 K using Langevin dynamics and a pressure of 1.0 bar using the Nosé-Hoover Langevin piston.[23,24] A timestep of 2 fs was used to calculate nonbonded and electrostatic interactions every two and four steps, respectively, using a cutoff of 12 Å by employing a switching function.[25] The SHAKE[26] and SETTLE[27] algorithms were used to constrain the lengths of all bonds involving hydrogen atoms. The particle-mesh Ewald summation method[28,29] was employed in the calculation of electrostatic interactions. The CHARMM36[30–32] force-field parameters were used for protein, lipids, and ions, with the TIP3P water model.[33] The PIP$_3$ headgroup was modeled using the CHARMM36 force-field for carbohydrates.[34]

4.2.6 Production run on Anton

After several nanoseconds of equilibration, the systems were transferred to Anton,[19] a special-purpose supercomputer for molecular dynamics simulations of biomolecules, and run for several microseconds. Anton software version 2.12.4 was used. An r-RESPA algorithm[35] was employed to integrate the equations of motion with a time step of 6 fs for the long-range non-bonded forces, and 2 fs for short-range non-bonded and bonded forces. The k-Gaussian split Ewald method[36] was

used for long-range electrostatic interactions. All bond lengths involving hydrogen atoms were constrained using SHAKE.[26] The simulations were performed at constant temperature (300K) and pressure (1 atm), using Nose-Hoover chains[37] and the Martyna-Tobias-Klein barostat.[23] The r-RESPA algorithm and the temperature and pressure controls were implemented using the multigrator scheme.[38] A summary of the simulations is provided in Table 4.1.

Table 4.1. Summary of membrane simulations

System	Bilayer Composition	Simulation Time
cPLA2-C2 domain	POPC	12 μs
GRP1-PH domain	75:25:1 POPC:POPS:DPPI	7 μs
POPC bilayer	POPC	1 μs
Mixed bilayer	75:25:1 POPC:POPS:DPPI	4 μs

4.3 Results

4.3.1 Stability of protein orientations

During the multi-microsecond simulations, the proteins remained stable and bound to the membrane for the entire time. The C2 domain tertiary structure remained highly stable, as seen in Figure 4.2. The Cα root mean squared deviation (RMSD) for the entire protein remained stationary over the 12 μs simulation, with an average value of 1.495 Å (± 0.181), while the β-sheets regions remained even more rigid with an average Cα RMSD value of 0.747 Å (± 0.109). The time-averaged root mean squared fluctuations (RMSF) for individual residues, shown in Figure 4.2, displays a higher degree of flexibility in the loops between the β-sheets. CBL1 displays slightly higher fluctuations than CBL2 and CBL3, which may be due to its larger presence in the lipid head-group region.
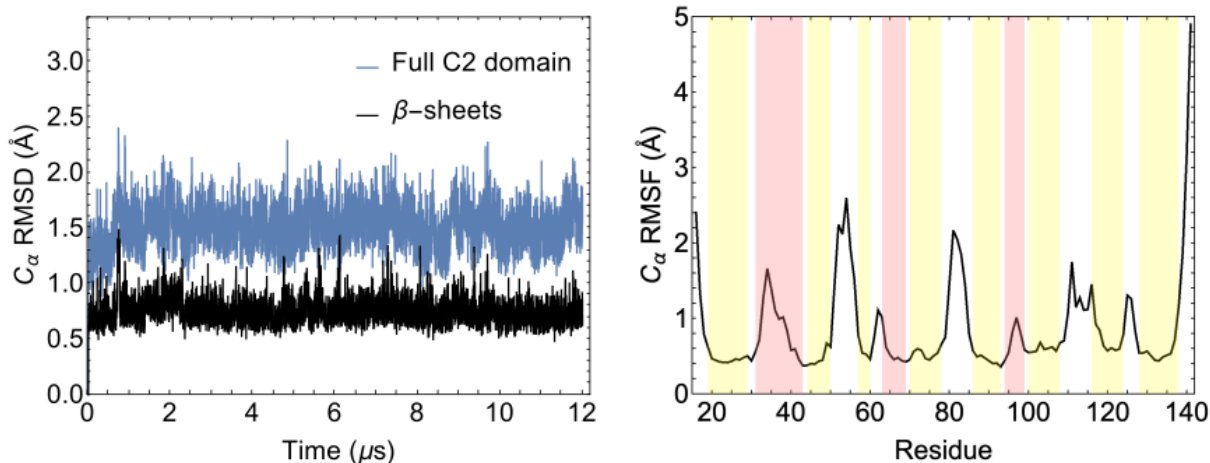
Figure 4.2. C2 domain structural fluctuations from MD simulation. (*left*) The root-mean-square deviation (RMSD) of the Cα positions for the full protein and only the β-sheet motifs. (*right*) The root-mean-square fluctuations (RMSF) of the Cα positions for each residue averaged over every 1 ns of simulation after aligning the structures by all Cα atom positions. The regions highlighted in yellow represent the β-sheets, and in pink the CBLs. The CBLs display relatively high fluctuations compared to the β-sheets.

The geometric orientation of the C2 domain remains fairly close to the predicted binding orientation from EPR measurements,[5] as seen in Figure 4.3. The protein remains embedded at a constant depth, although the angle made by the transmembrane axis and the vector defined by the total protein COM to the β-sheet COM, is slightly lower than reported from the experiments. Comparison with the crystal structure[3] show only slight deviations in the conformation at the end of the 12 μs simulation, as seen in Figure 4.4

Similar residue-lipid contacts are seen in Figure 4.5 compared to the initial binding pose and short MD simulations of Jaud, *et al*.[7] Each of the CBLs have some contact with the charged phosphate head-groups of the POPC lipids, but more interesting are the contacts from CBL1 and CBL3 with the deeper carbonyl and alkyl chain groups, highlighting that several of the lipid tails reach up and wrap around the CBLs as observed previously.[7]
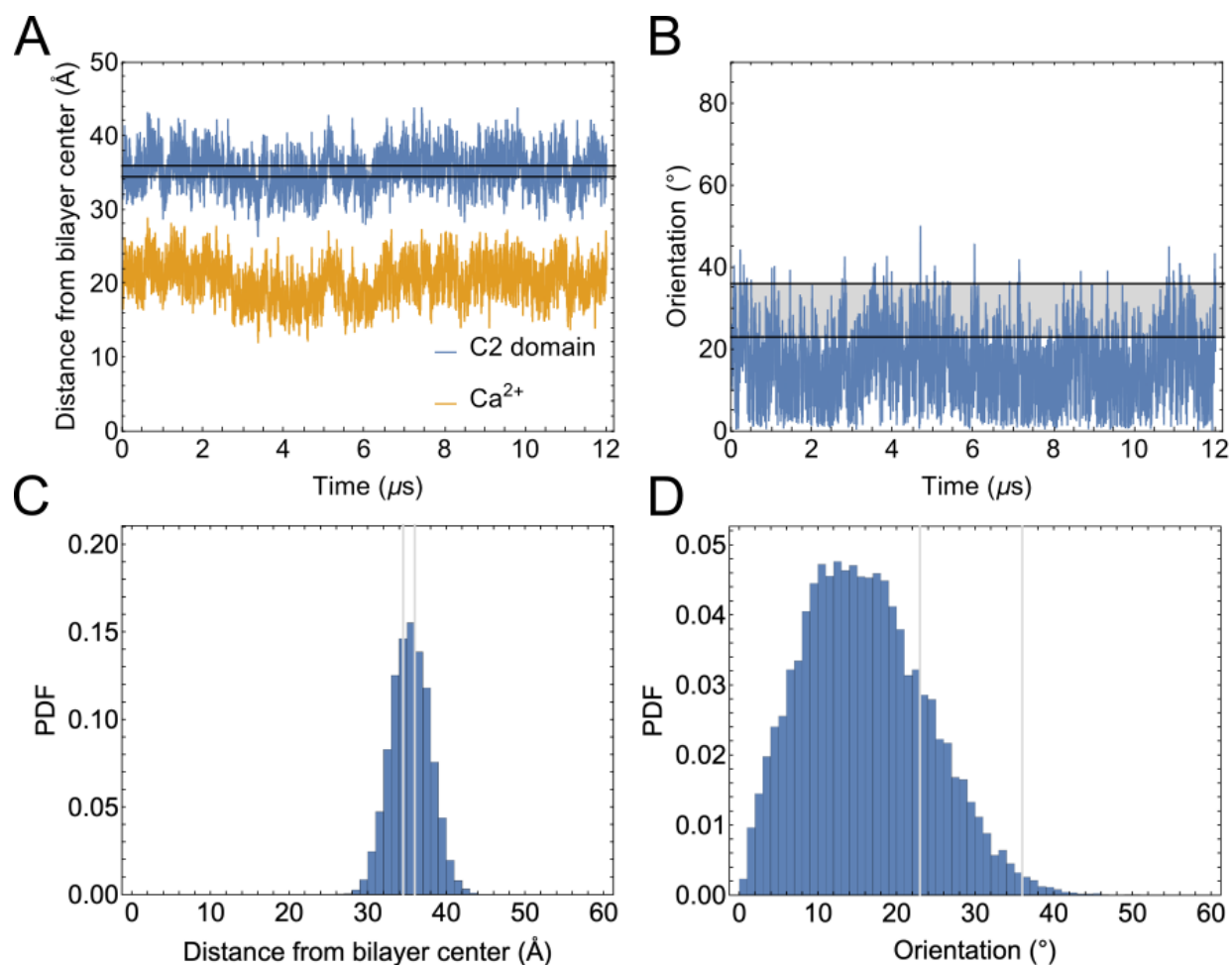
Figure 4.3. C2 domain orientation in the membrane matches experiments. (A) The distance from the center-of-mass (COM) of the bilayer for the protein and the Ca^{2+} ions. The black lines show the experimentally measured distance.[5] (B) The orientation angle of the C2 domain defined as the angle between the vector representing the transmembrane axis and the total protein COM to the beta-sheet COM. This was selected due to the beta-sheet stability. The observed angle is slightly lower than the expected value. (C) A histogram of the distances in panel (A) with 1 Å bin width. This shows good agreement with the EPR experiments. (D) A histogram of the orientation angles in panel (B) with 1° bin width.
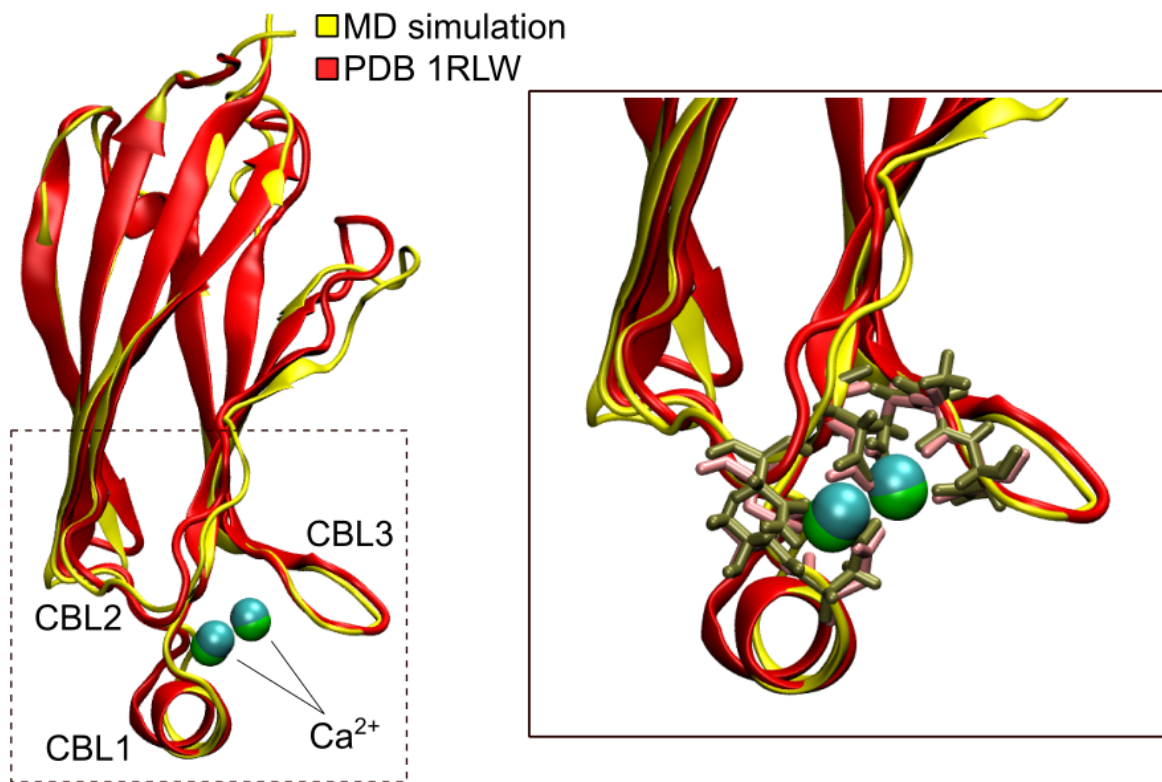
Figure 4.4. C2 domain structural comparison between the equilibrated model from MD simulation (*yellow*) and the crystal structure (PDB: 1RLW; *red*). The structures are in very good agreement with an average RMSD of 1.25±0.193 Å over the 12 µs simulation (sampled at every 10 ns) with a range of 0.89–1.71 Å. The bound Ca^{2+} ions are shown for the simulation (*cyan*) and crystal structure (*green*). Zooming in on the CBLs shows that the residue-ion contacts remain relatively constant.
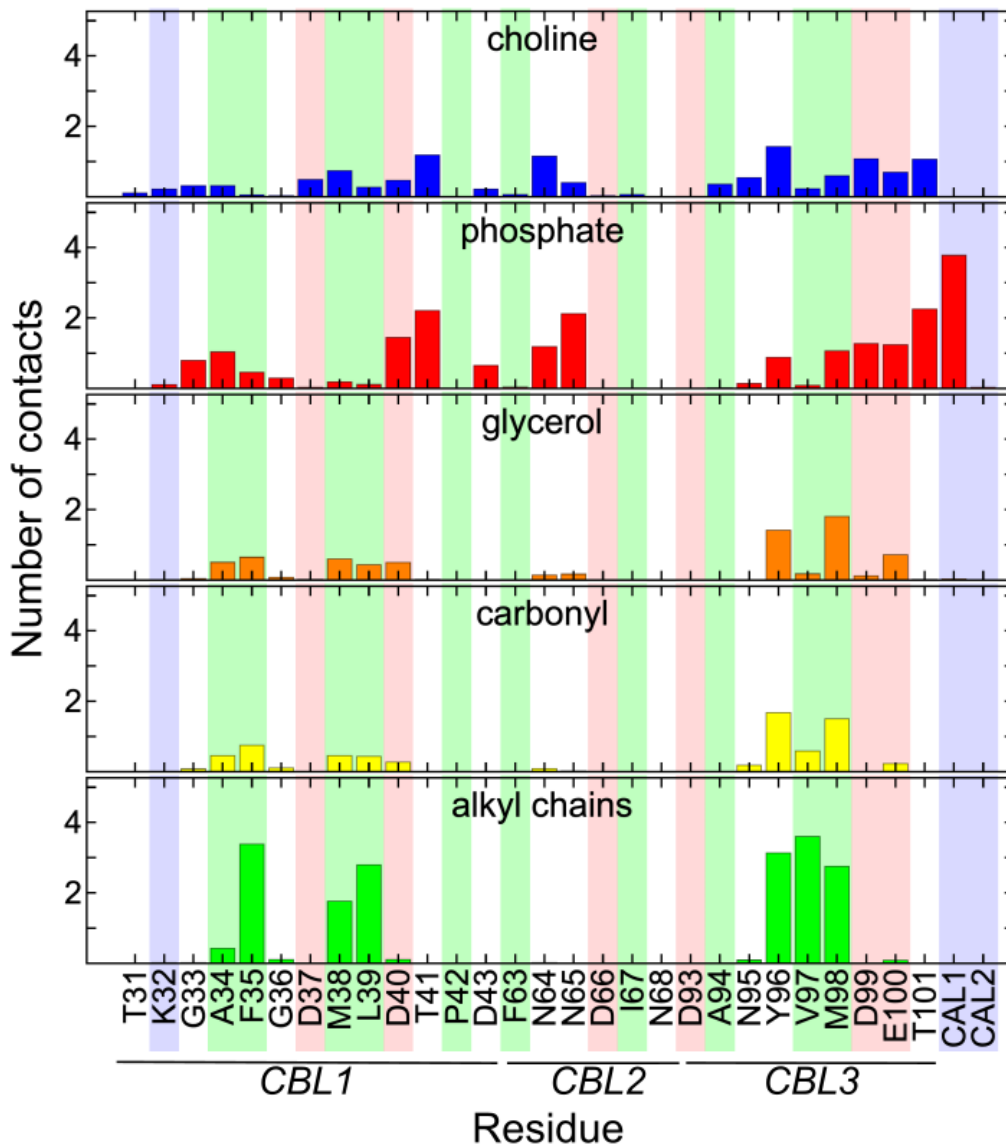
Figure 4.5. The time-averaged number of contacts between a C2 residue/Ca^{2+} with the lipid components in the POPC bilayer. Contacts were defined as heavy-atoms within a 4 Å cutoff. The transparent background vertical rectangles represent the type of interaction: positively charged (blue), negatively charged (red), non-polar (green), and polar (white).

The PH domain displays a similar level of stability, despite a different membrane binding mechanism. The Cα RMSD levels off during most of the 7 μs simulation, as seen in Figure 4.6, with a mean value of 1.621 Å (± 0.186) for the full protein and 1.315 Å (± 0.144) for the β-sheets. Again, the secondary structural elements, β-sheets and the α-helix, display lower fluctuations, while the connecting loops, including those identified to bind the PIP headgroup, show higher mobility. The PH domain binding geometry closely matches EPR experiments, in both the distance between centers-of-mass of the protein and bilayer, and the angle defined by the stable β-sandwich and membrane normal, as seen in Figure 4.7. To define the orientation, Chen, *et al.*[11] used the vector between the Cα atoms on C292 and F296, which makes an angle of 46° (± 7) with the membrane normal. Alignment to the crystal structure[10] shows stability in the secondary structural components, seed in Figure 4.8
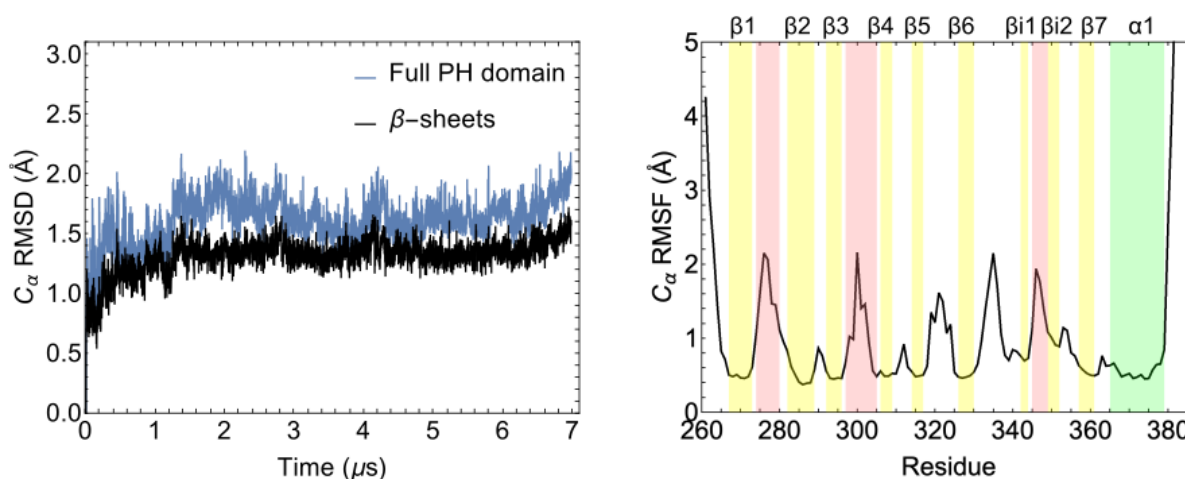

Figure 4.6. PH domain structural fluctuations from MD simulation. (*left*) The RMSD of the Cα positions for the full protein and only the β-sheet motifs. (Right) The RMSF of the Cα positions for each residue averaged over every 1 ns of simulation after aligning the structures by all Cα atom positions. The regions highlighted in yellow represent the β-sheets, in green is the α-helix, and in pink are the lipid binding loops. Like with the C2 domain, the β-sheets are highly stable with small fluctuations, while the linking loops, including those that bind with the lipid headgroups, are more mobile.
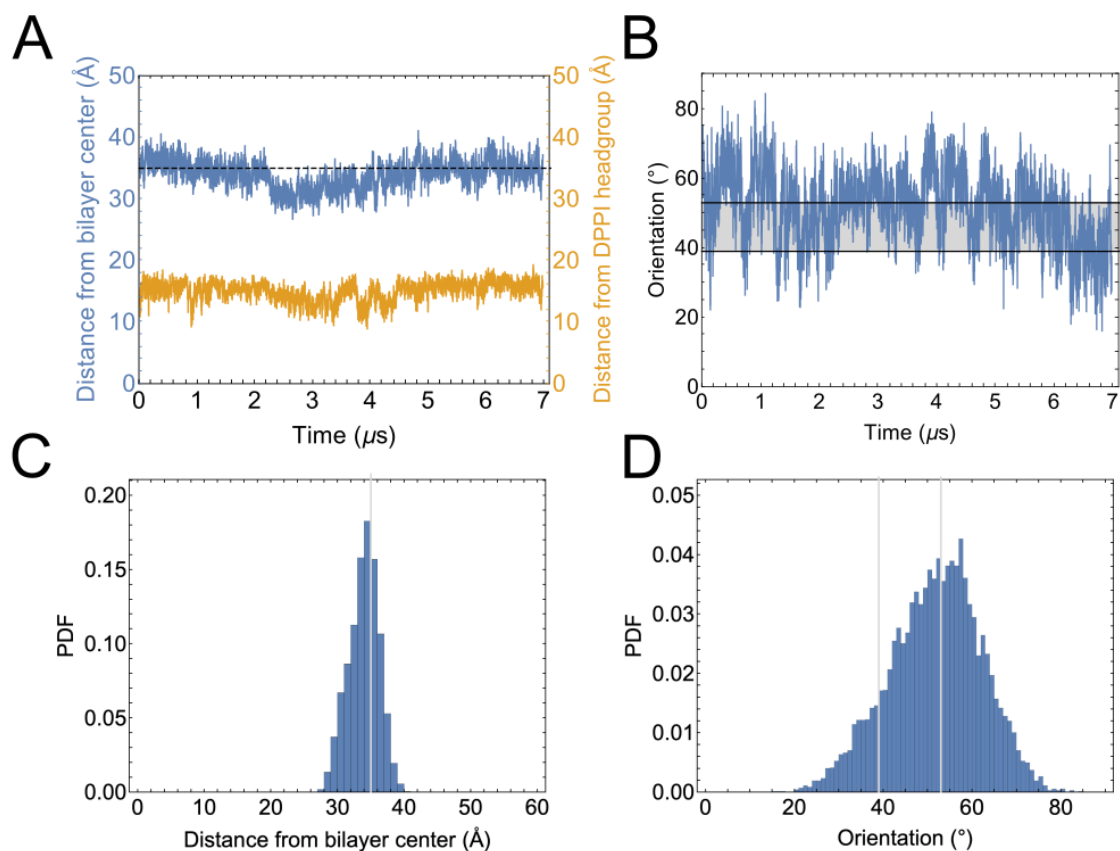
Figure 4.7. PH domain orientation in the membrane matches experiments. (A) The distance between the COM of the bilayer and the protein (*blue*) closely matches the predicted distance from a binding study based on EPR measurements.[11] The protein remains tightly bound to the DPPI lipid head-group (*orange*). The black lines show the experimentally measured value. (B) The orientation angle of the PH domain defined as the angle between the vector representing the transmembrane axis and the β-sheets represented by the vector from the Cα atoms of C292 to F296. (C) A histogram of the protein COM distance from the bilayer center with bin widths of 1 Å. (D) A histogram of the protein orientation angle with respect to the transmembrane axis. Bin widths are 1°.
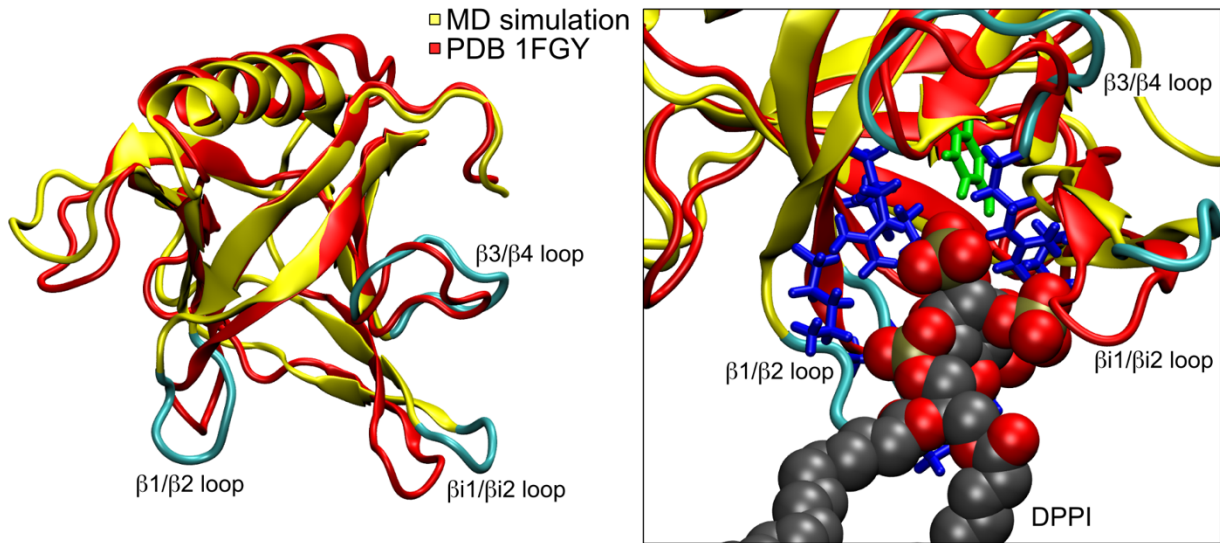
Figure 4.8. PH domain structural comparison between the equilibrated model from MD simulation (*yellow*) and the crystal structure (PDB: 1FGY; *red*). The structures are in very good agreement with an average RMSD of 2.25±0.21 Å over the 7 μs simulation (sampled at every 10 ns) with a range of 1.76–3.35 Å. The bound Ca^{2+} ions are shown for the simulation (*cyan*) and crystal structure (*green*). Zooming in on the CBLs shows that the residue-ion contacts remain relatively stationary.

The contacts made between the PH domain and different lipid components of the mixed bilayer are shown in Figure 4.9 and 4.10. Not surprisingly, positively charged basic residues on the loops β1/β2, β3/β4, and β5/β6 make multiple contacts with the negatively charged triphosphate headgroup of the DPPI lipid. In a similar fashion to the C2 domain, the lipid tails of surrounding POPC and POPS molecules make several protein contacts, but a majority of the contacts are with the headgroups, in line with the observation that the PH domain binds to the bilayer much less deeply than the C2 domain. The negatively charged headgroup of the POPS likely help to bind the protein through contacts with positive residues in the β-loops, as the serine headgroup sits slightly above the phosphate plane of the bilayer.
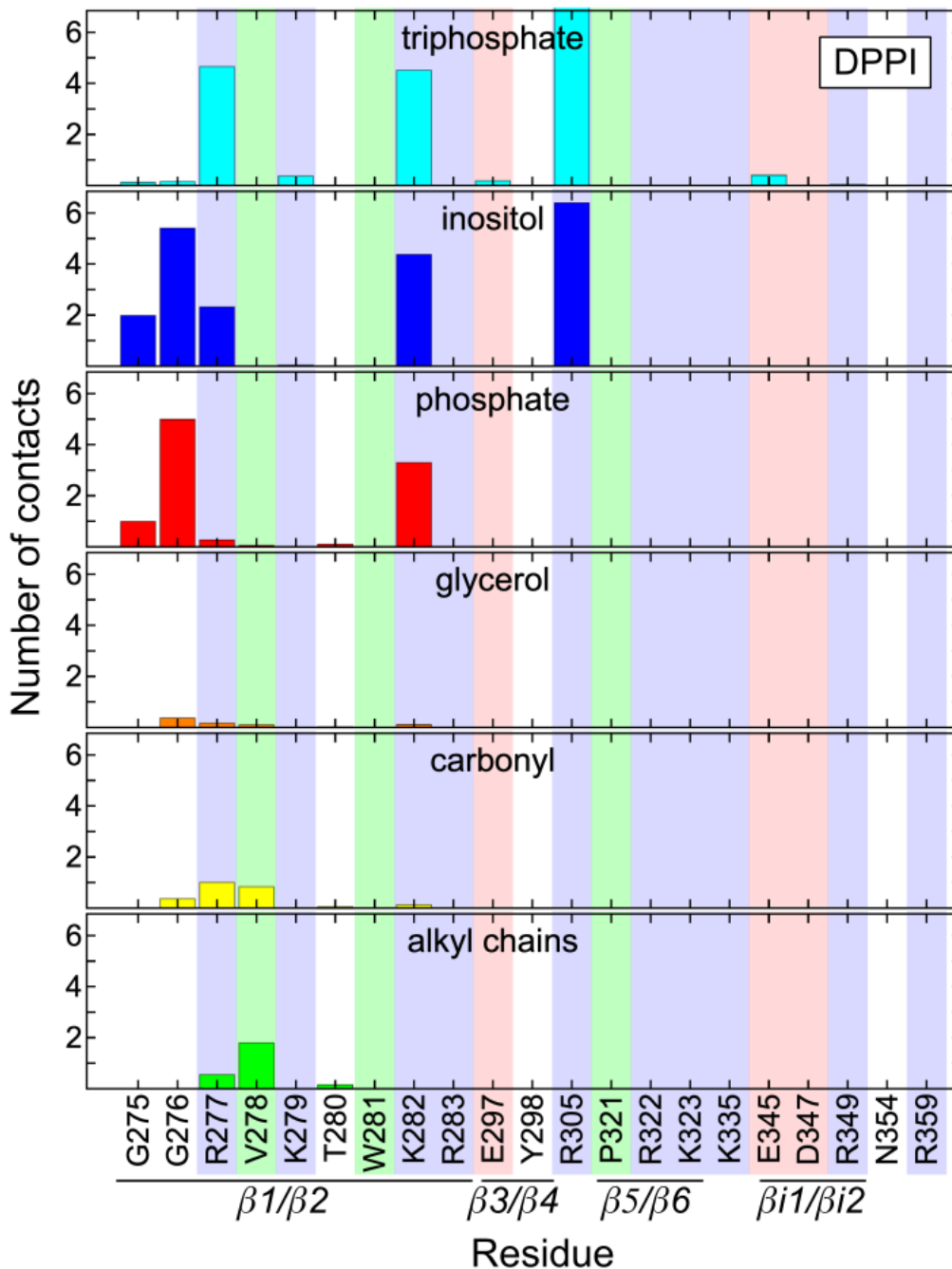
Figure 4.9. The time-averaged number of contacts between a PH residue with the DPPI lipid components in the bilayer. Contacts were defined as heavy-atoms within a 4 Å cutoff. The transparent background vertical rectangles represent the type of interaction: positively charged (blue), negatively charged (red), non-polar (green), and polar (white).
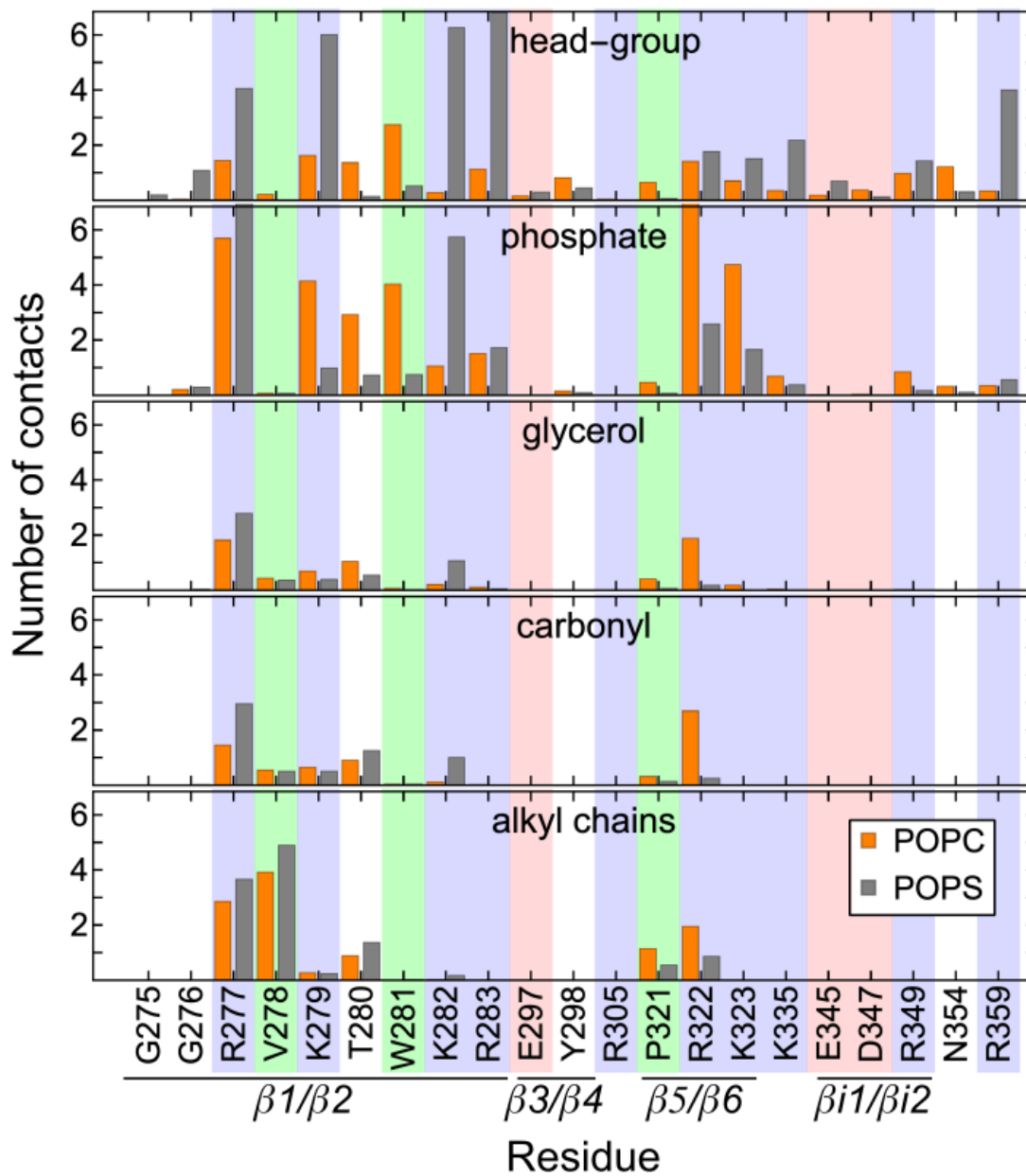
Figure 4.10. The time-averaged counts of contacts between a PH domain residue with the POPC (*orange*) and POPS (*gray*) lipid components in the bilayer. Contacts were defined as heavy-atoms within a 4 Å cutoff. The background vertical rectangles represent the type of interaction: positively charged (blue), negatively charged (red), non-polar (green), and polar (white).

4.3.2 Analysis of the 2-D trajectories

To analyze the diffusion, the centers-of-mass (COM) positions of the unwrapped protein systems were recorded for the lengths of the trajectories. Since we are interested in characterizing the 2-D diffusion along the membrane surface, we used the projection of the protein COM position on the membrane plane as the tracker. This allowed us to extract a 2-D trajectory, as seen in Figure 4.1B. For the membrane-only systems, the lipid phosphate COM positions were used for the POPC bilayer, and the DPPI triphosphate COM position for the mixed bilayer. The time-averaged MSD, $\overline{\delta^2(\Delta)}$, was calculated for each tracked particle by the following equation

$$\overline{\delta^2(\Delta)} = \frac{1}{T - \Delta} \int_0^{T-\Delta} [\mathbf{r}(t + \Delta) - \mathbf{r}(t)]^2 dt \qquad (4.3)$$

where Δ is the lag time and T is the measurement time of trajectory $\mathbf{r}(t)$.

For the POPC system, we were able to compute the average over the ensemble of particles

$$\langle \overline{\delta^2(\Delta)} \rangle = \frac{1}{N} \sum_{i=1}^{N} \overline{\delta_i^2(\Delta)} \qquad (4.4)$$

where N is the total number of particles. To classify the MSD, a linear fit was performed on the $\log_{10}$ data. This allowed us to obtain an estimate for the exponent (α) of the time-dependence, following the power-law relationship from Equation 4.2. The analysis for the C2 domain is shown in Figure 4.11, the PH domain in Figure 4.12, the POPC bilayer in Figure 4.13, and the DPPI lipids in the mixed bilayer in Figure 4.14.

The MSD gets noisy at long lag times due to less sampling, however, the MSD calculations at short lag times are averaging on the order of 10^5 separate displacements. During the longest

simulation, for the C2 domain, we see a crossover in the MSD lag-time dependence from $\sim t^{0.82}$ to $\sim t^{0.99}$, around 50 ns lag-time. This is also seen clearly in the POPC bilayer system, with a crossover from $\sim t^{0.72}$ to $\sim t^{1.06}$ around a lag-time of 10 ns. This result is similar to what was observed for atomistic simulations of a DSPC bilayer.[39] The PH domain system and DPPI system displayed a smaller change in the α-values, 0.89 to 0.95 and 0.86 to 0.96, respectively. Both of these systems would likely have benefitted from running longer simulations to better sample long lag times. Regardless, all four systems display anomalous subdiffusion at short lag times.

The C2 domain system showed a slight dependence at short lag times on the atom selection used to track the motion. When the Ca^{2+} ions were used as the tracker, as opposed to the protein COM position, the MSD appears linear for all lag-times, suggesting it follows normal Brownian motion. This may be due to a higher mobility of the Ca^{2+} ions within the binding pocket. However, in order to make a consistent comparison with the PH domain, the COM positions of the proteins were used as the tracker in both systems for subsequent analyses.
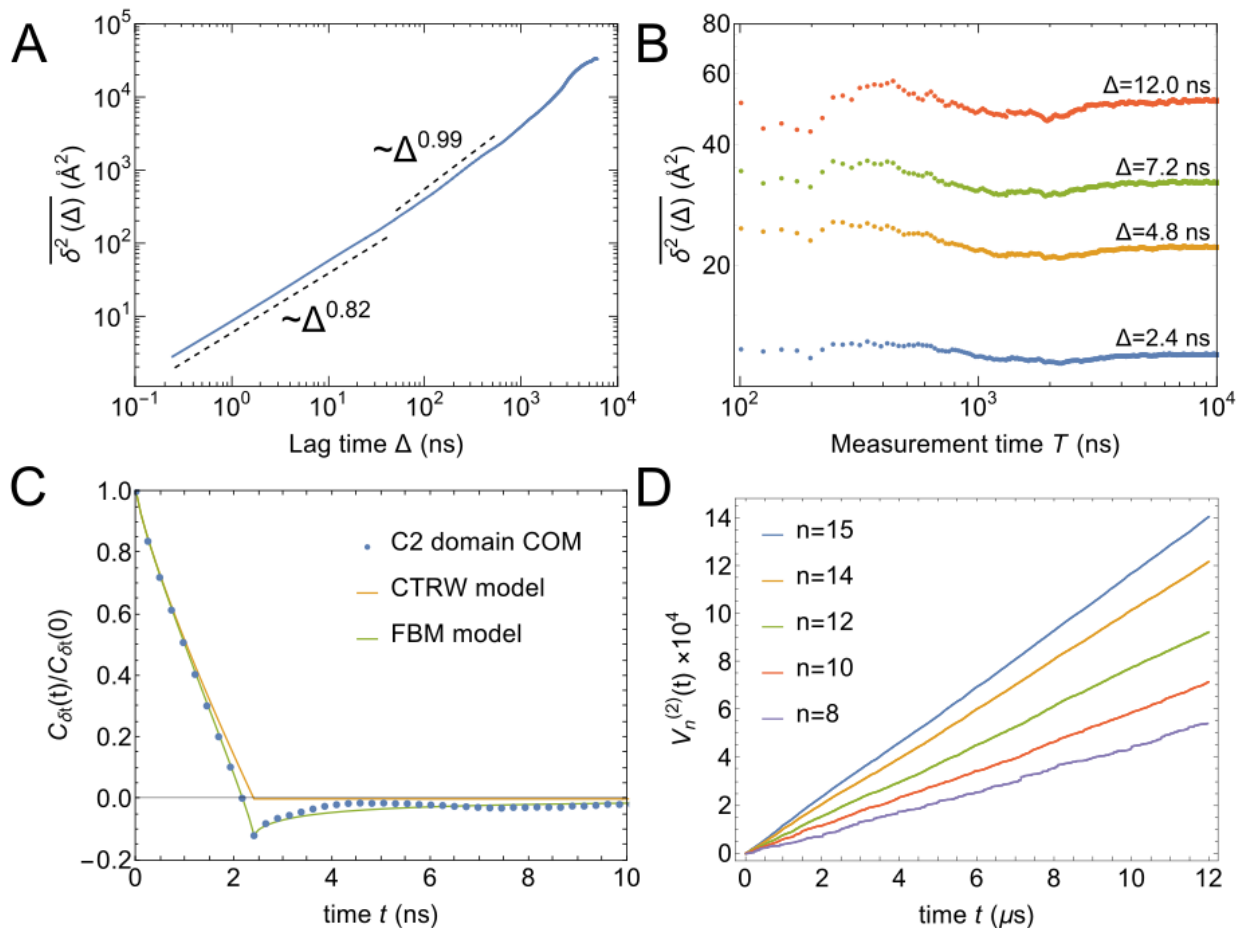
Figure 4.11. Anomalous subdiffusion of the C2 domain along the membrane surface. (A) The time-averaged MSD of the COM for the C2 domain. Subdiffusion is observed for lag times (Δ) up to ~50 ns with $\alpha = 0.82$. After that it appears to switch over to normal Brownian motion with $\alpha = 0.99$. (B) The MSD for selected Δ as a function of the measurement time, T. There is no observed measurement time dependence on the MSD. (C) The displacement autocorrelation for $\delta t = 2.4$ ns (10 frames). The anti-correlation near δt is indicative of FBM. (D) The quadratic variation of the increments of the trajectory shown for different sizes, n, of the increments.
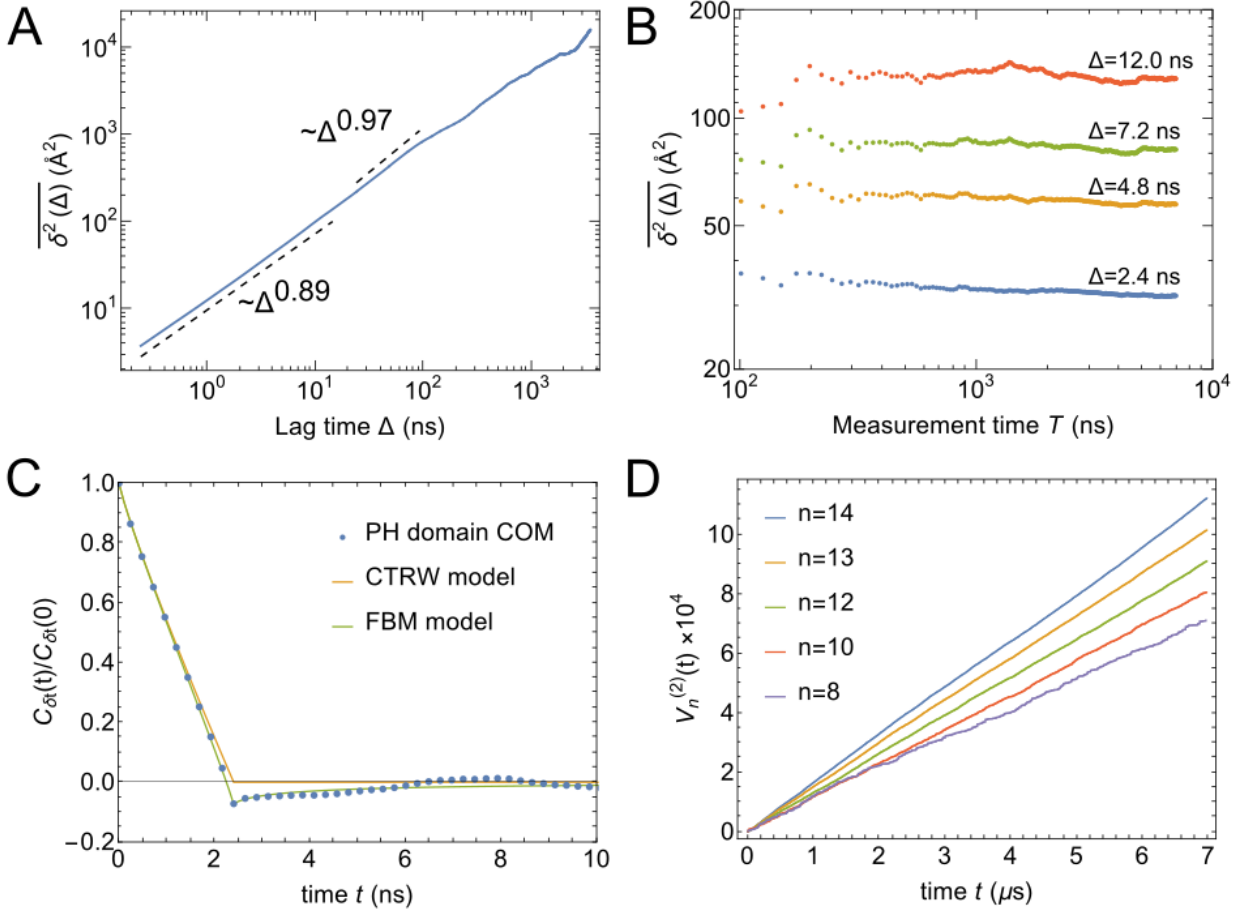
Figure 4.12. Anomalous subdiffusion of the PH domain along the membrane surface. (A) The time-averaged MSD of the COM of the PH domain. Subdiffusion is observed for lag times (Δ) up to ~20 ns with $\alpha = 0.89$. After that it appears to switch over to normal Brownian motion with $\alpha = 0.97$. (B) The MSD for selected Δ as a function of the measurement time, T. There is no observed measurement time dependence on the MSD. (C) The displacement autocorrelation for $\delta t = 2.4$ ns (10 frames). The anti-correlation near δt is indicative of FBM. (D) The quadratic variation of the increments of the trajectory shown for different sizes, n, of the increments.
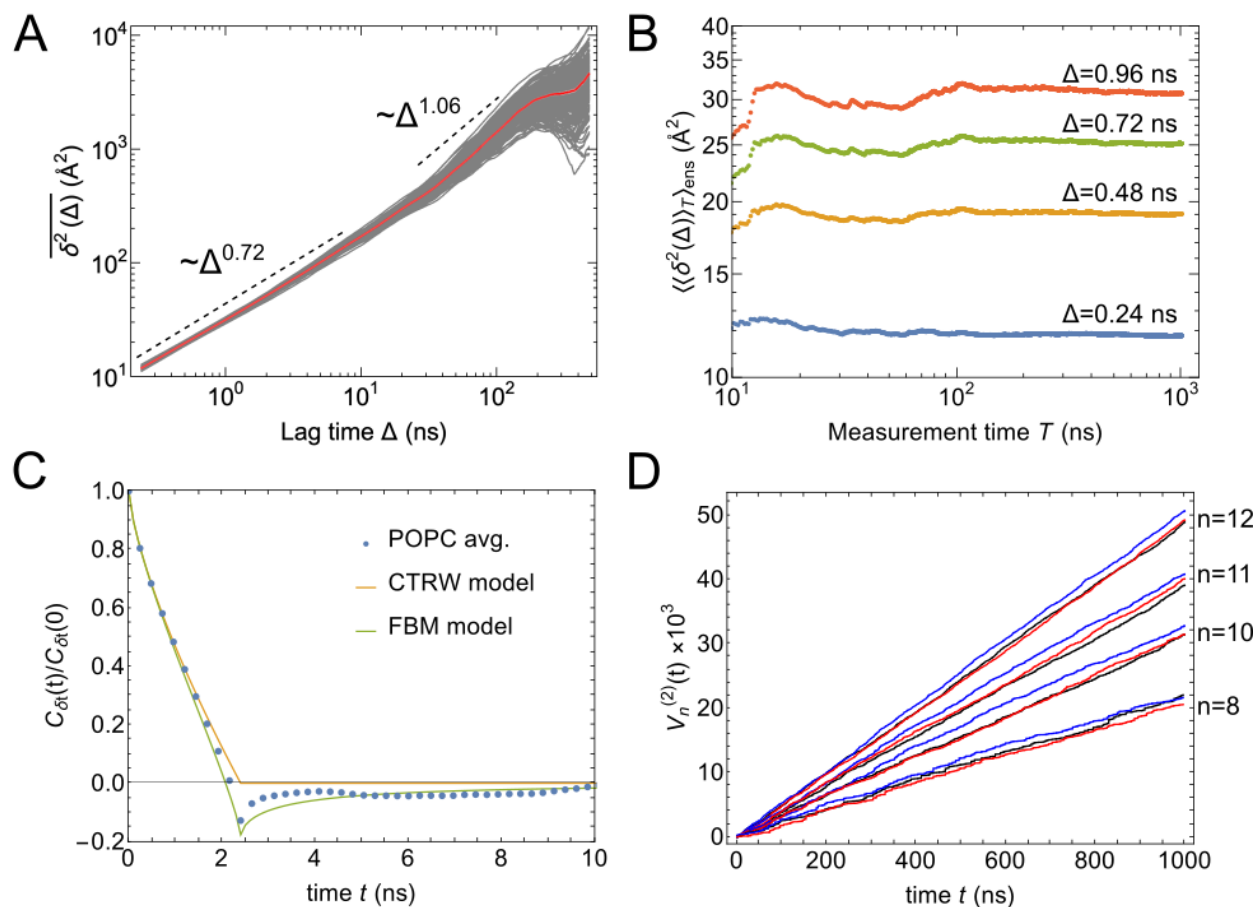
Figure 4.13. Anomalous subdiffusion of lipids in the POPC membrane system. (A) The time-averaged MSD for the COM of the phosphate groups in each of the 215 POPC lipid molecules (*grey*) and the average (*red*). (B) The time-ensemble-averaged MSD as a function of measurement time for selected lag time values. Unlike for the protein systems, this quantity adds a further averaging over the ensemble of POPC molecules. (C) The displacement autocorrelation as a function of time averaged over all 215 POPC molecules. The error bars (SEM) are smaller than the points. The theoretical models were plotted for the parameters: $\alpha = 0.72$ and $\delta t = 2.4$ ns. (D) The quadratic variation of three individual POPC molecules randomly selected (shown in black, blue, and red) for various n.
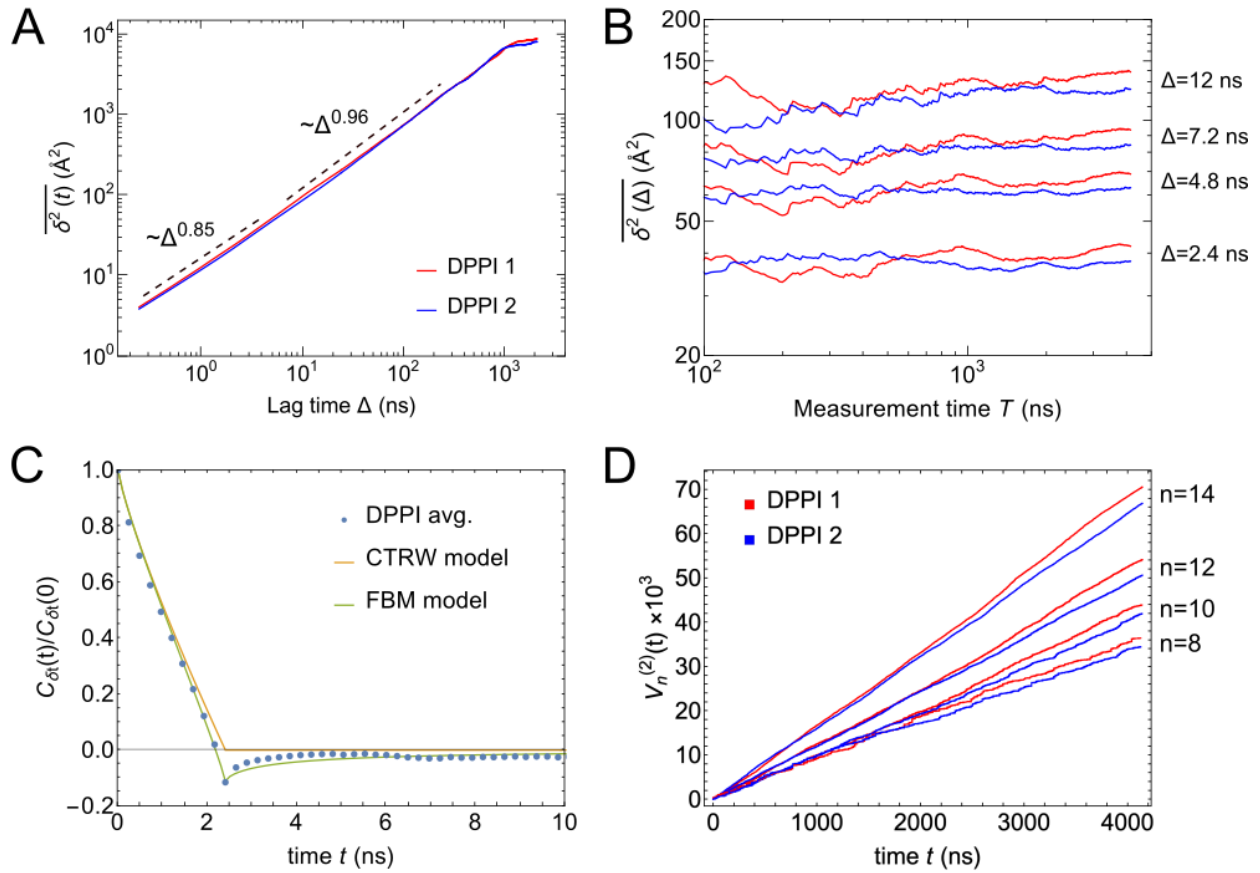
Figure 4.14. Anomalous subdiffusion of the two DPPI lipid molecules in the mixed membrane system. (A) The time-averaged MSD for the COM of the triphosphate head-groups in both of the DPPI molecules. (B) The MSD as a function of measurement time for selected lag time values. (C) The displacement autocorrelation as a function of time averaged over the two DPPI molecules. The theoretical models were plotted for the parameters $\alpha = 0.85$ and $\delta t = 2.4$ ns. (D) The quadratic variation of each of the DPPI molecules for various n.

4.3.3 Dependence on the measurement time

Further tests were performed in order to assign the observed subdiffusion to one of the primary mathematical models. One such measure is to compute the MSD at a set value of the lag time for varying measurement times, T. If the MSD displays a strong dependence on the measurement time, it is said to exhibit aging behavior.[40] A continuous-time random walk (CTRW) process has a measurement time dependence that scales as $T^{(\alpha-1)}$,[41] while an ergodic process like fractional Brownian motion (FBM) is independent of the measurement time due to the stationary increments of the steps.

For all four systems, $\overline{\delta^2(\Delta)}$ does not display a dependence on the measurement time and instead remains constant. The lag times were selected to be well within the region where the MSD is subdiffusive. This can be used to say that the diffusion of the particle does not exhibit ageing, and therefore does not follow a CTRW model. Instead, this measurement supports the FBM model. Similar behavior was also seen in the simulations of the DSPC bilayer.[39]

4.3.4 Autocorrelation of the displacements

The displacement autocorrelation function is another convenient analysis for studying subdiffusion. For arbitrary time step δt,

$$C_{\delta t}(t) = \langle [\mathbf{r}(t + \delta t) - \mathbf{r}(t)] \cdot [\mathbf{r}(\delta t) - \mathbf{r}(0)] \rangle / \delta t \qquad (4.5)$$

Normal Brownian motion displays no correlation after the first step, due to the zero mean of the first moment. The same can be said for a particle in the CTRW model, the displacements are uncorrelated for $t > \delta t$.[41] The normalized autocorrelation for a CTRW follows the equation

$$\frac{C_{\delta t}(t)}{C_{\delta t}(0)} = \begin{cases} 1 - \left({}^{t}/_{\delta t} \right)^{\alpha} & t \leq \delta t \\ 0 & t \geq \delta t \end{cases} \tag{4.6}$$

However, the FBM model has a strong anticorrelation in its displacements, before becoming uncorrelated at longer times, given by the equation

$$\frac{C_{\delta t}(t)}{C_{\delta t}(0)} = \frac{|t + \delta t|^{\alpha} - 2t^{\alpha} + |t - \delta t|^{\alpha}}{2\delta t^{\alpha}} \tag{4.7}$$

All four systems show anticorrelation for δt = 2.4 ns, as displayed by the negative peak for $\frac{C_{\delta t}(t)}{C_{\delta t}(0)}$. This is addition evidence that the subdiffusion displayed by the lipids and lipid-bound proteins follows a FBM model, and not a CTRW model.

4.3.5 Variation in the increments

A novel statistical test developed by Magdziarz, *et al.*[42] looks at the partial sum over varying increments of the trajectory. For a stochastic process, $x(t)$ observed on the time interval $[0, T]$, the p-variation for time t within $[0, T]$ is given by the equation

$$V^{(p)}(t) = \lim_{n \to \infty} V_n^{(p)}(t) \tag{4.8}$$

Where $V_n^{(p)}(t)$ is the partial sum of the increment given by

$$V_n^{(p)}(t) = \sum_{j=0}^{2^n - 1} \left| x \left(\frac{(j+1)T}{2^n} \wedge t \right) - x \left(\frac{jT}{2^n} \wedge t \right) \right|^p \tag{4.9}$$

Where $\wedge$ represents the minimum operator. This so-called p-variation test is useful for distinguishing between the CTRW and FBM models due to the different behavior that they display. For a process with stationary increments, like FBM, the p-variation behaves as

$$V^{(p)}(t) = \begin{cases} +\infty & \text{if } p < \dfrac{1}{H} \\[2mm] tE\left(|B_H(1)|^{\frac{1}{H}}\right) & \text{if } p = \dfrac{1}{H} \\[2mm] 0 & \text{if } p > \dfrac{1}{H} \end{cases} \tag{4.10}$$

Where H is the self-similarity Hurst exponent, which is related to the subdiffusion exponent by $H = \alpha/2$, and the expected value is given by the equation

$$E\left(|B_H(1)|^{\frac{1}{H}}\right) = \frac{\sigma^{1/H} 2^{1/2H}}{\sqrt{\pi}} \Gamma\left(\frac{1}{2H} + \frac{1}{2}\right) \tag{4.11}$$

Where Γ is the gamma function and σ is the coefficient factor of the second moment. In the case of a process with non-stationary increments, such as with a heavy-tailed CTRW,

$$V^{(p)}(t) = \begin{cases} +\infty & \text{if } p < 2 \\ S_\alpha(t) & \text{if } p = 2 \\ 0 & \text{if } p > 2 \end{cases} \tag{4.12}$$

For the quadratic variation, $p = 2$, as you increase the number of increments, n up to 2^N, the observed behavior for each subdiffusive model is different. For a CTRW process, $V_n^2(t)$ follows the inverse subordinator $S_\alpha(t)$ of the motion, whereas for a FBM process, $V_n^2(t)$ increases with increasing n. The second variation is plotted for various n in Figure 4.5D. A clear trend shows the increase in $V_n^2(t)$ with n.

Additionally, one can look at the $1/H$ variation. For a FBM process, $V_n^{1/H}(t)$ goes as time scaled by the factor in Equation 4.11. For a CTRW process, $V_n^{1/H}(t)$ decays to zero for increasing n. As

seen in Figure 4.6, each of the systems converges fairly well to the expected value for FBM, independent of *n*.

4.3.6 Ensemble quantities for the POPC bilayer

The POPC domain system can be examined even further, taking into account ensemble-averaged quantities. Looking at ensemble measurements provides further verification for the FBM behavior. Averaging over the 215 POPC lipid molecules, the time- and ensemble-averaged MSD show very similar behavior, as seen in Figure 4.8. This is indicative of an ergodic process, like FBM. It is interesting to see that the distribution of α-values span from 0.5, a common value for subdiffusive processes, to slightly over 1.0. The mean of this distribution is 0.75, close to the fitted α-value from Figure 4.13A.
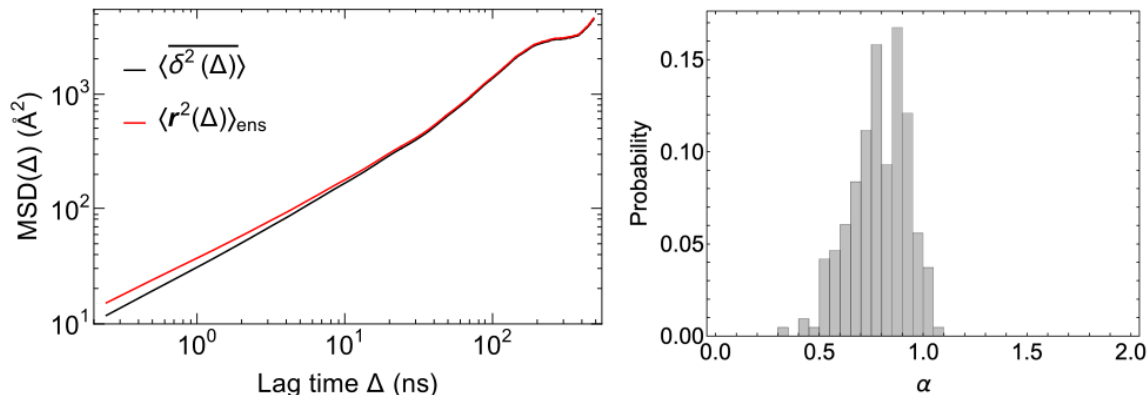

Figure 4.15. Ensemble analysis of the POPC lipids. (*left*) A comparison of the averaged time-averaged MSD and the ensemble-averaged MSD shows good agreement, indicating ergodicity. (*right*) The distribution of α-values for all POPC lipids from fitting the first 10% of the total trajectory time.

4.4 Discussion

The long multi-microsecond atomistic simulations of the two peripheral membrane signaling proteins revealed three new observations. The first was that on the timescales explored by these simulations, both the C2 domain, which is embedded into the headgroup region of the bilayer, and the PH domain, which specifically binds to a single PIP_3 lipid, remain bound to the membrane and maintain a constant orientation. While membrane dissociation has been reported from fluorescent measurements of the GRP1 PH domain on a supported bilayer,[55] the typical residency time is greater than one second. So we do not expect to see dissociation events during our microsecond simulations.

The second observation is that the signaling proteins and the lipids within the bilayers exhibit anomalous subdiffusion on short timescales, i. e. less than 50 ns. This is seen from the exponent of the MSD time dependence, reported in Table 4.2. It is worth noting that these alpha values are larger than those reported from simulations of bilayers[25] comprising of DSPC ($\alpha = 0.63$), DOPC ($\alpha = 0.67$), SOPC ($\alpha = 0.66$), and POPE[56] ($\alpha = 0.7$).

Table 4.2. Diffusion parameters

System	Subdiffusion exponent (α)	Diffusion constant ($\mu m^2/s$)
C2 domain	0.82	11.0
PH domain	0.89	25.7*
POPC lipid	0.72	28.8
DPPI lipid	0.85	24.5

*system dimensions do not match

All of the systems reported here display a crossover from anomalous subdiffusion ($\alpha < 1$) to normal Brownian motion ($\alpha = 1$) at long lag times. By fitting this linear segment of the MSD, a diffusion constant can be extracted. Although, it has been shown that diffusion measurements

obtained from simulations using the particle mesh Ewald treatment of electrostatic interactions have a strong dependence on finite system-size effects.[57,58] The embedded C2 domain diffuses slower than the lipid-binding PH domain, and comparing simulations of comparable system sizes can show a qualitative trend. However, the PH domain system was elongated in the y-axis compared to the x-axis, which makes a direct comparison of the diffusion constants unreliable.

The final observation is that the subdiffusion follows a fractional Brownian motion model, displaying anticorrelation for the particle excursions and an independence from the overall measurement time. Subdiffusion of this type is due to a viscoelastic medium in which the particle is diffusing. Similar FBM behavior is reported for other pure bilayer systems.[25] So it is reasonable to expect that the PH domain, by binding to a single lipid, would display similar behavior, perhaps at a slower rate. However, it was interesting to see that the C2 domain, which does not diffuse in tandem with a single lipid molecule, displays the same type of subdiffusive motion. It appears evident from these results that individual lipid molecules in the bilayer and small membrane associated proteins experience the same viscoelastic environment during their excursions, at least up to microsecond timescales.

4.5 Bibliography

1. Ziemba, B. P. & Falke, J. J. Lateral diffusion of peripheral membrane proteins on supported lipid bilayers is controlled by the additive frictional drags of (1) bound lipids and (2) protein domains penetrating into the bilayer hydrocarbon core. *Chem. Phys. Lipids* 172–173, 67–77 (2013).

2. Leslie, C. C. Regulation of the specific release of arachidonic acid by cytosolic phospholipase A2. *Prostaglandins, Leukot. Essent. Fat. Acids* 70, 373–376 (2004).

3. Perisic, O., Fong, S., Lynch, D. E., Bycroft, M. & Williams, R. L. Crystal Structure of a Calcium-Phospholipid Binding Domain from Cytosolic Phospholipase A2. *J. Biol. Chem.* 273, 1596–1604 (1998).

4. Dessen, A. *et al*. Crystal Structure of Human Cytosolic Phospholipase A2 Reveals a Novel Topology and Catalytic Mechanism. *Cell* 97, 349–360 (1999).

5. Malmberg, N. J., Van Buskirk, D. R. & Falke, J. J. Membrane-Docking Loops of the cPLA2 C2 Domain: Detailed Structural Analysis of the Protein-Membrane Interface via Site-Directed Spin-Labeling. *Biochemistry* 42, 13227–13240 (2003).

6. Frazier, A. A. *et al*. Membrane Orientation and Position of the C2 Domain from cPLA2 by Site-Directed Spin Labeling †. *Biochemistry* 41, 6282–6292 (2002).

7. Jaud, S., Tobias, D. J., Falke, J. J. & White, S. H. Self-induced docking site of a deeply embedded peripheral membrane protein. *Biophys. J.* 92, 517–24 (2007).

8. Ferguson, K. M. *et al*. Structural Basis for Discrimination of 3-Phosphoinositides by Pleckstrin Homology Domains. *Mol. Cell* 6, 373–384 (2000).

9. Moravcevic, K., Oxley, C. L. & Lemmon, M. A. Conditional Peripheral Membrane Proteins: Facing up to Limited Specificity. *Structure* 20, 15–27 (2012).

10. Lietzke, S. E. *et al*. Structural Basis of 3-Phosphoinositide Recognition by Pleckstrin Homology Domains. *Mol. Cell* 6, 385–394 (2000).

11. Chen, H.-C., Ziemba, B. P., Landgraf, K. E., Corbin, J. A. & Falke, J. J. Membrane Docking Geometry of GRP1 PH Domain Bound to a Target Lipid Bilayer: An EPR Site-Directed Spin-Labeling and Relaxation Study. *PLoS One* 7, e33640 (2012).

12. Lai, C.-L. *et al*. Molecular Mechanism of Membrane Binding of the GRP1 PH Domain. *J. Mol. Biol.* 425, 3073–3090 (2013).

13. Lumb, C. N. *et al*. Biophysical and Computational Studies of Membrane Penetration by the GRP1 Pleckstrin Homology Domain. *Structure* 19, 1338–1346 (2011).

14. Knight, J. D., Lerner, M. G., Marcano-Velázquez, J. G., Pastor, R. W. & Falke, J. J. Single Molecule Diffusion of Membrane-Bound Proteins: Window into Lipid Contacts and Bilayer Dynamics. *Biophys. J.* 99, 2879–2887 (2010).

15. Gaede, H. C. & Gawrisch, K. Lateral Diffusion Rates of Lipid, Water, and a Hydrophobic Drug in a Multilamellar Liposome. *Biophys. J.* 85, 1734–1740 (2003).

16. Campagnola, G., Nepal, K., Schroder, B. W., Peersen, O. B. & Krapf, D. Superdiffusive motion of membrane-targeting C2 domains. *Sci. Rep.* 5, 17721 (2016).

17. Fogedby, H. C. Langevin equations for continuous time Lévy flights. *Phys. Rev. E* 50, 1657–1660 (1994).

18. Yamamoto, E., Kalli, A. C., Akimoto, T., Yasuoka, K. & Sansom, M. S. P. Anomalous Dynamics of a Lipid Recognition Protein on a Membrane Surface. *Sci. Rep.* 5, 18245 (2015).

19. Shaw, D. E. *et al.* Anton, a special-purpose machine for molecular dynamics simulation. *Commun. ACM* 51, 91 (2008).

20. Hollingsworth, S. A. At the interface of experiment and computation: Explorations of heme protein redox partner interactions, water behavior on organic surfaces and other systems. (Dissertation, University of California, Irvine, 2016).

21. Humphrey, W., Dalke, A. & Schulten, K. VMD: Visual molecular dynamics. *J. Mol. Graph.* 14, 33–38 (1996).

22. Phillips, J. C. *et al.* Scalable molecular dynamics with NAMD. *J. Comput. Chem.* 26, 1781–802 (2005).

23. Martyna, G. J., Tobias, D. J. & Klein, M. L. Constant pressure molecular dynamics algorithms. *J. Chem. Phys.* 101, 4177 (1994).

24. Feller, S. E., Zhang, Y., Pastor, R. W. & Brooks, B. R. Constant pressure molecular dynamics simulation: The Langevin piston method. *J. Chem. Phys.* 103, 4613 (1995).

25. Grubmüller, H., Heller, H., Windemuth, A. & Schulten, K. Generalized Verlet Algorithm for Efficient Molecular Dynamics Simulations with Long-range Interactions. *Mol. Simul.* 6, 121–142 (1991).

26. Ryckaert, J.-P., Ciccotti, G. & Berendsen, H. J. C. Numerical integration of the cartesian equations of motion of a system with constraints: molecular dynamics of n-alkanes. *J. Comput. Phys.* 23, 327–341 (1977).

27. Miyamoto, S. & Kollman, P. A. Settle: An analytical version of the SHAKE and RATTLE algorithm for rigid water models. *J. Comput. Chem*. 13, 952–962 (1992).

28. Sagui, C. & Darden, T. A. Molecular dynamics simulations of biomolecules: long-range electrostatic effects. *Annu. Rev. Biophys. Biomol. Struct*. 28, 155–179 (1999).

29. Essmann, U. *et al*. A smooth particle mesh Ewald method. *J. Chem. Phys*. 103, 8577–8593 (1995).

30. MacKerell, A. D. *et al*. All-Atom Empirical Potential for Molecular Modeling and Dynamics Studies of Proteins †. *J. Phys. Chem. B* 102, 3586–3616 (1998).

31. Mackerell, A. D., Feig, M. & Brooks, C. L. Extending the treatment of backbone energetics in protein force fields: limitations of gas-phase quantum mechanics in reproducing protein conformational distributions in molecular dynamics simulations. *J. Comput. Chem*. 25, 1400–15 (2004).

32. Klauda, J. B. *et al*. Update of the CHARMM all-atom additive force field for lipids: validation on six lipid types. *J. Phys. Chem. B* 114, 7830–43 (2010).

33. Jorgensen, W. L., Chandrasekhar, J., Madura, J. D., Impey, R. W. & Klein, M. L. Comparison of simple potential functions for simulating liquid water. *J. Chem. Phys*. 79, 926 (1983).

34. Hatcher, E. R., Guvench, O. & MacKerell, A. D. CHARMM Additive All-Atom Force Field for Acyclic Polyalcohols, Acyclic Carbohydrates, and Inositol. *J. Chem. Theory Comput*. 5, 1315–1327 (2009).

35. Tuckerman, M., Berne, B. J. & Martyna, G. J. Reversible multiple time scale molecular dynamics. *J. Chem. Phys*. 97, 1990 (1992).

36. Shan, Y., Klepeis, J. L., Eastwood, M. P., Dror, R. O. & Shaw, D. E. Gaussian split Ewald: A fast Ewald mesh method for molecular simulation. *J. Chem. Phys*. 122, 054101 (2005).

37. Martyna, G. J., Klein, M. L. & Tuckerman, M. Nosé–Hoover chains: The canonical ensemble via continuous dynamics. *J. Chem. Phys*. 97, 2635 (1992).

38. Lippert, R. A. *et al*. Accurate and efficient integration for molecular dynamics simulations at constant temperature and pressure. *J. Chem. Phys*. 139, 164106 (2013).

39. Sokolov, I. M. Models of anomalous diffusion in crowded environments. *Soft Matter* 8, 9043 (2012).

40. Burov, S., Jeon, J.-H., Metzler, R. & Barkai, E. Single particle tracking in systems showing anomalous diffusion: the role of weak ergodicity breaking. *Phys. Chem. Chem. Phys.* 13, 1800 (2011).

41. Magdziarz, M., Weron, A., Burnecki, K. & Klafter, J. Fractional Brownian Motion Versus the Continuous-Time Random Walk: A Simple Test for Subdiffusive Dynamics. *Phys. Rev. Lett*. 103, 180602 (2009).

42. Magdziarz, M. & Klafter, J. Detecting origins of subdiffusion: *P*-variation test for confined systems. *Phys. Rev. E* 82, 011129 (2010).

43. Knight, J. D. & Falke, J. J. Single-Molecule Fluorescence Studies of a PH Domain: New Insights into the Membrane Docking Reaction. *Biophys. J.* 96, 566–582 (2009).

44. Akimoto, T., Yamamoto, E., Yasuoka, K., Hirano, Y. & Yasui, M. Non-Gaussian Fluctuations Resulting from Power-Law Trapping in a Lipid Bilayer. *Phys. Rev. Lett.* 107, 178103 (2011).

45. Klauda, J. B., Brooks, B. R. & Pastor, R. W. Dynamical motions of lipids and a finite size effect in simulations of bilayers. *J. Chem. Phys*. 125, 144710 (2006).

46. Vögele, M. & Hummer, G. Divergent Diffusion Coefficients in Simulations of Fluids and Lipid Membranes. *J. Phys. Chem. B* 120, 8722–8732 (2016).

Chapter 5

Classification of the subdiffusion of the Piezo1 mechanosensitive ion channel from single-particle tracking experiments

5.1 Background

Mechanical forces in cell membranes play an important role in many physiological processes. Specialized proteins, mechanically-activated ion channels, provide rapid and highly sensitive response to mechanical stimuli.[1] The recently identified Piezo channels permeate Ca^{2+} and other cations, generating both chemical and electrical signals in response to mechanical stimuli.[2,3] Piezo1 has diverse roles in various physiological processes, including the differentiation of neural stem/progenitor cells and the development of the vascular system.[4–7] However, the sub-cellular dynamics of the channel, and how these characteristics contribute to its function, are unknown.

Previous work using measurements of endogenous Piezo1 activity and traction forces in native cellular conditions showed that actomyosin-based cellular traction forces generate Ca^{2+} "flickers" in the absence of externally-applied mechanical forces.[8] Using total internal reflection fluorescence (TIRF) microscopy, Piezo1 channels were observed to diffuse readily in the membrane. However, the flicker activity was enhanced in regions near to traction-force producing adhesions. It was proposed that diffusion allows Piezo1 to efficiently respond to transient, local mechanical stimuli.[8] Classification of the diffusion of Piezo1 may provide insight into this process.

A previous single-particle tracking experiment using TIRF microscopy performed on the Kv2.1 voltage-gated K^+ ion channel revealed that channel clusters exhibited subdiffusive motion.[9]

Further analysis revealed that the subdiffusion displayed both ergodic and nonergodic properties. The nonergodic process was linked to transient binding events to the actin cytoskeleton, which could be modeled by a continuous-time random walk (CTRW). Disruption of the cytoskeleton by treatment with drugs that inhibit actin polymerization recovered ergodicity in the diffusion, while still remaining anomalous. This ergodic process was attributed to an underlying fractal structure, as modeled by a random walk on a fractal (RWF). In order to fully describe the subdiffusion of the channel clusters, a subordination process was used, for which a RWF model was subordinated to a CTRW model.

Likewise, insulin granules expressing fluorescent fusion proteins in MIN6 cells were also found to display properties of a subordinated random walk, although the model that best described this system was fractional Brownian motion (FBM) subordinated to a CTRW.[10] Upon addition of Vinblastine, a drug which disrupts microtubule formation, the FBM and CTRW components of the motion were separated to short-times and long-times, respectively. The shuttling of the insulin granules along the fragmented microtubules lead to FBM-type behavior for short times (< 10 s), while the long-time behavior more closely matched a CTRW model with the granules detaching and then moving to a disconnected segment on the microtubules.

In order to study the diffusion of Piezo1, we performed single-particle tracking measurements of tdTomato-tagged endogenous Piezo1 channels using TIRF microscopy. We found that the channels undergo anomalous diffusion. This subdiffusion was categorized most prominently as non-ergodic, modeled by a CTRW process indicative of trapping events along the particle's trajectory. However, an observed anticorrelation in the displacements, consistent with FBM, suggests that a mixed model supporting multiple mechanisms better describes the diffusion. We

performed additional studies of this system disrupting the actin cytoskeleton to elucidate the secondary component of the subdiffusion.

The following represents an on-going project to elucidate the nature of Piezo1's mobility and its interactions with the cellular environment in order to gain insight into how this ion channel transduces mechanical cues under native cellular conditions.

5.2 Methods

5.2.1 Mouse embryonic fibroblast culture

The experiments used mouse embryonic fibroblast (MEF) cells from a reporter mouse with a tdTomato knock-in on the C-terminus of the endogenous Piezo1 channel.[5] These tdTomato-MEFs (tdT-MEFs) were cultured in DMEM (ThermoFisher Scientific) with 15% fetal bovine serum, 1x GlutaMax (ThermoFisher Scientific), 1 mM sodium pyruvate (ThermoFisher Scientific), and 1x non-essential amino acid solution (ThermoFisher Scientific) at 37°C with 5% CO_2. Cells were used at passages 3-6. tdT-MEFs were coated onto 35 mm dishes with a no. 1.5 coverslip and a 14 mm glass diameter bottom (MatTek) and adhered using human fibronectin, incubated on the plate for 3 hours in MEM solution.

5.2.2 Drug treatment of Piezo1

tdT-MEFs were treated with 50 μM and 100 μM Cytochalasin D and allowed to incubate for 15 minutes prior to imaging. Cells were then imaged from 15-45 minutes post-treatment.

5.2.3 Cell staining

tdT-MEFs were fixed using 4% paraformaldehyde, 1x PBS, 5 mM MgCl$_2$, 10 mM EGTA, 40 mg/mL sucrose buffer for 10 minutes at room temperature. The cells were washed once with PBS for 15 minutes. The cells were then permeabilized with 0.3% Triton X-100 (Sigma Aldrich) in PBS and washed once again with PBS for 15 minutes. The cells were then probed with phalloidin 488 for actin (prepared in 1% BSA in PBS) overnight at 4°C. The cells were washed once with PBS for 15 minutes. Following this, the cells were probed with Hoechst for 5 minutes.

5.2.4 Total internal reflection fluorescence microscopy

For Piezo1 diffusion studies, images were acquired on a Nikon N-STORM system built around a Nikon Eclipse Ti microscope. The imaging objective used was a Nikon 100x APO TIRF oil immersion objective (NA 1.49). Images were acquired on an Andor iXon3 electron-multiplying charge-coupled device (EMCCD) camera with a 100 ms exposure time and 109.5 nm/px in TIRF mode. Cells were continuously illuminated with a 561 nm.

5.2.5 Piezo1 particle tracking

TIRFM image stacks were processed using Flika software[11] in order to determine the location of Piezo1-tdTomato puncta in each frame. Each frame was spatially bandpass filtered by taking the difference of Gaussians, an image processing algorithm that enhances a band of spatial frequencies, in this case, around the size of the particles. The spatially filtered movie was then thresholded using a manually determined threshold, yielding a binary movie. Spatially contiguous pixels above threshold were grouped together and considered a single particle. The centroid for each particle was determined by fitting a 2-D Gaussian function to each particle, yielding a centroid with subpixel precision. The initial coordinates for the fit were set to be the center of mass of the

binary pixels in the particle. Any localizations within consecutive frames that were within three pixels of each other were assumed to arise from the same particle. These localizations were linked over time to generate the particle tracks. A snapshot of the trajectory extraction process is shown in Figure 5.1.
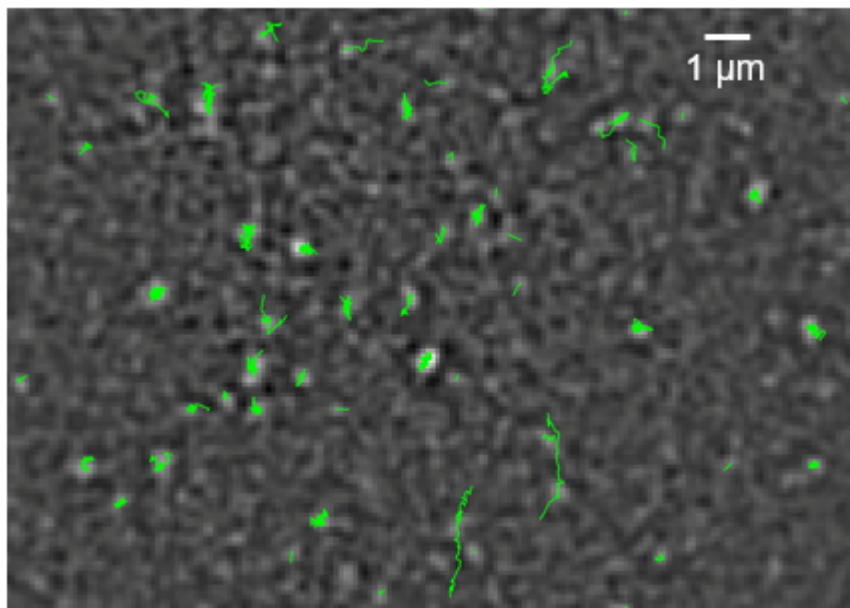

Figure 5.1. The particle track extraction process in Flika. Linked tracks are shown in green.

5.2.6 Defining mobile trajectories

For the analyses presented here, the tracks were obtained from ten videos of individual untreated cells and seven videos of cells treated with 50 μM Cytochalasin D. All of the cells were plated on the same day. Tracks from cells under similar conditions (untreated versus treated) were aggregated into larger sets. Two criteria were used for selecting the tracks for the analysis: (1) the track had to be at least 20 seconds long, and (2) the mean-squared displacement (MSD) value at one second lag time had to be greater than 0.018 μm^2. This value was selected based on the estimated localization error of 12.7 nm for the 2-D particle fitting. This estimation was obtained

as the standard deviation of the normally distributed particle point intensity as $\sqrt{2/\pi}\left(\frac{1}{SNR}\right)$.

Particles with mean squared displacements less than this localization error were assumed to be trapped due to some condition of the cell plating, or likely autofluorescence from a non-Piezo1 artifact. Two example tracks, one mobile and the other trapped, artificially moved next to each other are shown in Figure 5.2.
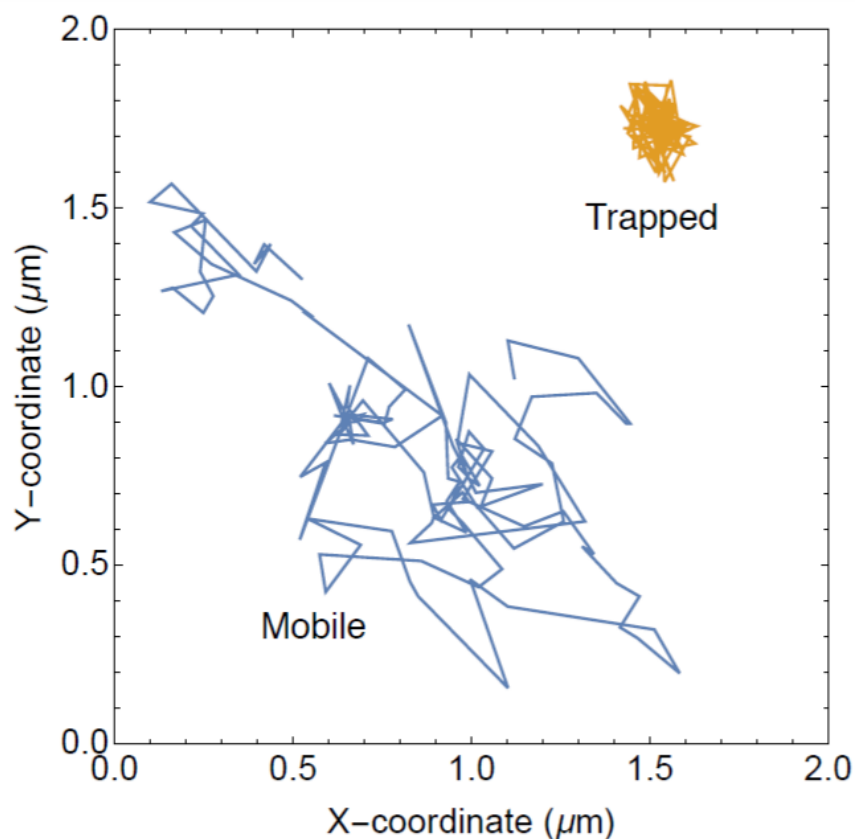

Figure 5.2. Sample trajectories of a mobile and a trapped track. Both trajectories are the same length, 12.5 seconds, and artificially moved next to each other.

5.3 Results

5.3.1 Piezo1 trajectories display anomalous subdiffusion

The mean-squared displacement serves as a primary analysis when studying diffusion. This can be calculated for an individual trajectory as an average over the time origins using the equation

$$\overline{\delta^2(\Delta)} = \frac{1}{T-\Delta} \int_0^{T-\Delta} [\mathbf{r}(t+\Delta) - \mathbf{r}(t)]^2 dt \tag{5.1}$$

With lag time Δ during the total measurement time T for trajectory $\mathbf{r}(t)$. The collection of time-averaged MSD $\overline{\delta^2(\Delta)}$ for 473 mobile trajectories is shown in Figure 5.3. Even with a fairly rigorous selection criteria, the spread of $\overline{\delta^2(\Delta)}$ is still quite significant over all lag times, but especially at long lag times where it spans more than two orders of magnitude.
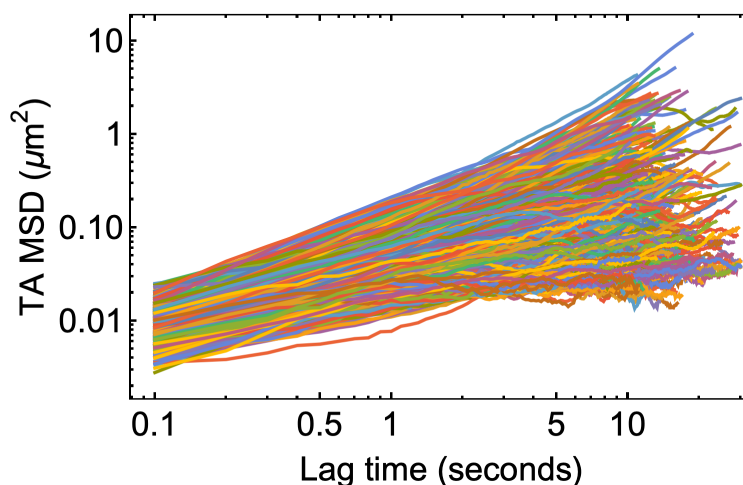

Figure 5.3. The time-averaged MSD for the individual Piezo1 tracks. Each color represents a different track out of the 473 mobile tracks. The maximum lag time for each track is ½ of the total length.

These individual $\overline{\delta^2(\Delta)}$ can be averaged over the number of tracks to obtain

$$\langle \overline{\delta^2(\Delta)} \rangle = \frac{1}{N} \sum_{i=1}^{N} \overline{\delta_i^2(\Delta)} \tag{5.2}$$

where N is the number of tracked particles. Alternatively, the squared-displacements can be averaged over the ensemble of tracked particles using the equation

$$\langle \mathbf{r}^2(t) \rangle = \frac{1}{N} \sum_{n=1}^{N} (\mathbf{r}_n(t) - \mathbf{r}_n(0))^2 \tag{5.3}$$

The quantities $\langle \overline{\delta^2(\Delta)} \rangle$ and $\langle \mathbf{r}^2(\Delta) \rangle$ are plotted in Figure 5.4. Performing linear fitting of the $\log_{10}$ data at short lag times allows us to obtain the exponent α for the time dependence. For $\alpha = 1$, there is a linear time-dependence of the MSD $\langle \mathbf{r}^2(\Delta) \rangle \sim \Delta$, indicative of normal Brownian motion. However, we see that the MSD scales sublinearly with time, $\langle \mathbf{r}^2(\Delta) \rangle \sim \Delta^\alpha$, where $\alpha < 1$, indicating subdiffusive motion. Interestingly, the spread of $\overline{\delta^2(\Delta)}$ also results in a wide distribution of α-values, shown in Figure 5.5, with most falling within the subdiffusive region, but several at $\alpha = 1$ or greater (i. e. superdiffusive).
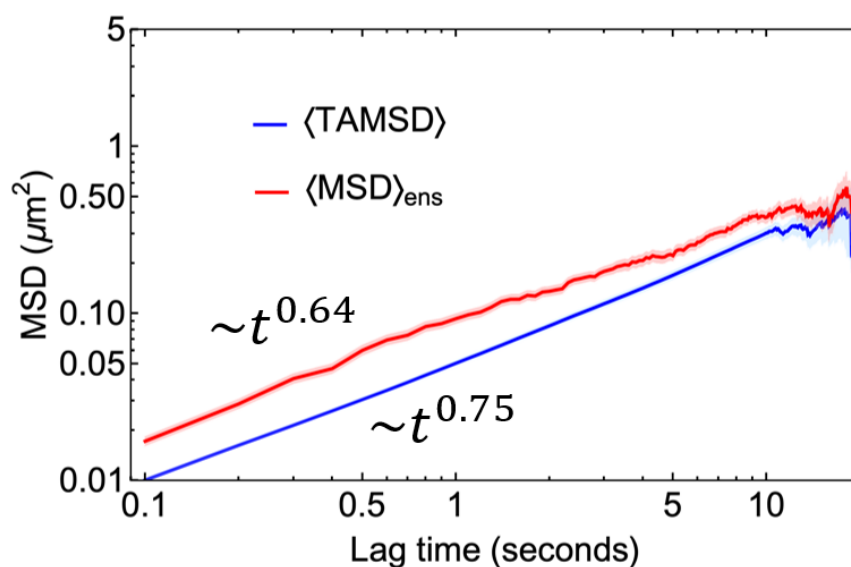

Figure 5.4. A comparison of the time and ensemble-averaged MSD of Piezo1. The shaded regions seen prominently at large lag times represent the standard error of the mean. The scaling of the MSD with lag time was obtained by linear fit to the $\log_{10}$ data.
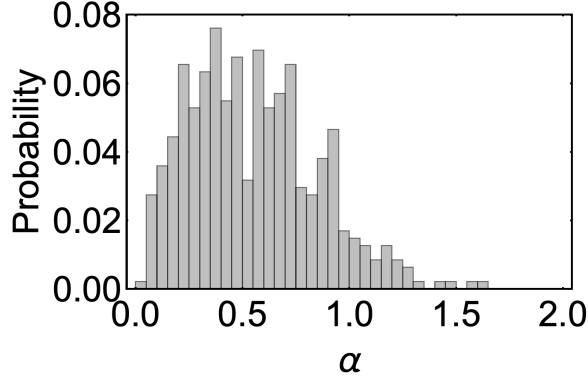
Figure 5.5. The distribution of α values of the time-averaged MSD. These were calculated using the first 10% of each of the MSD curves plotted in Figure 5.3. The bin widths are 0.05.

Anomalous diffusion can also be distinguished from normal diffusion by looking at the cumulative distribution function (CDF) of the squared displacements.[12,13] The CDF is given by the equation

$$CDF(r^2, \Delta) = \int_0^r P(r')2\pi r' dr' \tag{5.4}$$

with propagator $P(r)$. Normal Brownian motion results in a CDF with the form of a single-exponential function

$$CDF(r^2, \Delta) = 1 - \exp(-r^2/r_0^2) \tag{5.5}$$

where $r_0^2 = \langle \mathbf{r}^2(\Delta) \rangle$ the MSD. However, the expression for anomalous diffusion has a double-exponential form

$$CDF(r^2, \Delta) = 1 - [w \exp(-r^2/r_1^2) + (1 - w) \exp(-r^2/r_2^2)] \tag{5.6}$$

The weighting factor, w, approaches a value of 0.5 for anomalous diffusion. Figure 5.6A shows the CDF for a lag time of $\Delta = 100$ ms with a single and double-exponential fit and the corresponding residuals. The double-exponential fit from Equation 5.6 matches the data far better than the single-exponential function, and Figure 5.6B shows the weighting factor has a value

around 0.6 for various lag times. The mobility of the tracked Piezo1 channels are clearly subdiffusive.
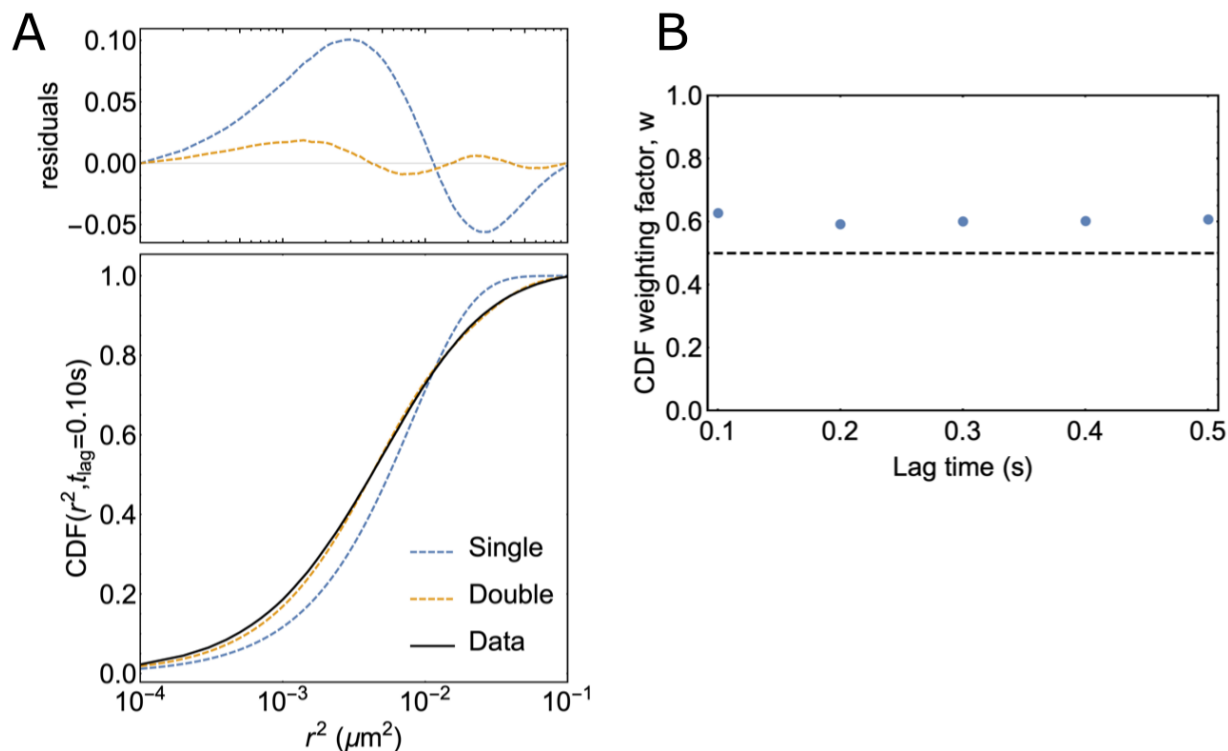

Figure 5.6. The cumulative distribution function of the displacements at 100 ms lag time. (A) The CDF is plotted with the single and double-exponential fits given by Equations 5.5 and 5.6, respectively. The residuals for the fits show a smaller deviation with the double-exponential function. (B) The weighting factor, w, for the double-exponential fits for various lag times. A value close to 0.5 signifies anomalous diffusion.

5.3.2 Non-ergodicity for the subdiffusion

A process is considered ergodic when it satisfies $\langle \mathbf{r}^2(\Delta) \rangle = \lim\limits_{\Delta/T \to 0} \overline{\delta^2(\Delta)}$. The difference in $\langle \overline{\delta^2(\Delta)} \rangle$ and $\langle \mathbf{r}^2(\Delta) \rangle$ shown in Figure 5.4 at suggests non-ergodicity. This difference is more easily observed in the distributions of squared displacements in Figure 5.7. The temporal MSD distribution is constructed from the individual tracks at a specific lag time, here $\Delta = 100$ ms or 1 frame. The ensemble MSD distribution is measured by averaging the squared displacements of all

trajectories occurring at a specific time for the same lag time, e.g. the displacements occurring between 10.0 s and 10.1 s. The widths of these two distributions is significantly different, verifying the non-ergodicity.
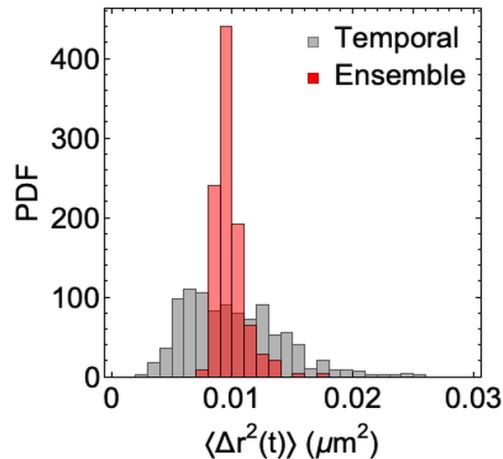

Figure 5.7. Distributions of the time and ensemble-averaged MSD values. The temporal MSD values are taken from the individual tracks at a lag time of 100 ms. The ensemble MSD values are obtained by averaging the squared displacements of all tracks at a specific time. Bin widths are 0.001 μm^2.

An additional quantity, the time-ensemble-averaged MSD (TEA-MSD) as a function of the measurement time, can be used to determine if the subdiffusion exhibits a property called aging. This is represented by a decreasing TEA-MSD with measurement time as the particle slows down the longer you watch it. Such behavior is a hallmark of the CTRW model, where a particle becomes trapped with a heavy-tailed waiting-time distribution. Figure 5.8A shows a strong dependence of the TEA-MSD on the measurement time. Although the trend predicted by the CTRW model, MSD~$T^{(\alpha-1)}$, is not followed. Instead the measurement time dependence decreases as $T^{-0.12}$, which would require $\alpha = 0.88$. The TEA-MSD expressed as a function of lag time in Figure 5.8B returns a subdiffusion exponent close to the value from Figure 5.4.
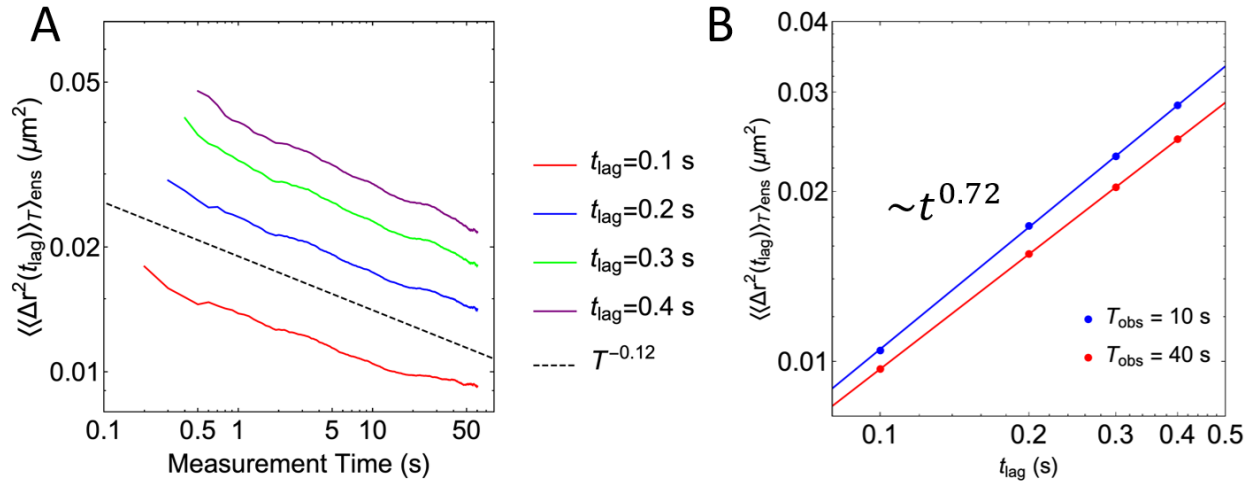
Figure 5.8. The time-ensemble-averaged MSD. (A) TEA-MSD as a function of measurement time. The decreasing behavior represents aging and is seen for different lag times. (B) TEA-MSD as a function of lag time. The two different measurement times show a similar dependence on lag time, with $\alpha = 0.72$. This value is close to the subdiffusion exponent from the time-averaged MSD.

Another verification that the behavior of the particles follows the CTRW model is seen by the waiting times. For a CTRW, the waiting time distribution is heavy-tailed with an infinite mean, allowing for the observation of immobilization of the particle. The waiting time distribution is constructed by measuring how long it takes a particle to escape from a radial threshold centered on the particle's position at a given time origin. Figure 5.9 shows the waiting time distributions for multiple thresholds, with a decay following the expected power law behavior $P_w(\tau) \sim \tau^{-(1+\alpha)}$.
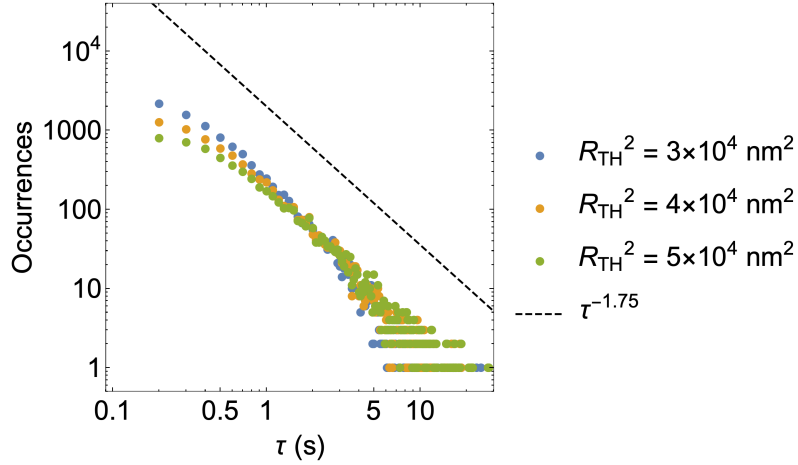
Figure 5.9. The waiting time distribution for Piezo1 excursions. The waiting time is defined as the amount of time it takes for the displacement of a particle to exceed a set radial threshold. CTRW has a heavy-tailed waiting time distribution of the form $P_w(\tau) \sim \tau^{-(1+\alpha)}$, where $\alpha = 0.75$ from the MSD.

5.3.3 Absence of a fractal structure

If a particle is diffusing within a system with an underlying fractal structure, the dimension of the diffusivity should be less than the actual system dimensions. The fractal dimension, d_f, can be uncovered by determining the probability of finding the particle at time t in a growing sphere of radius $r_0 t^{\alpha/2}$.[14] The value for r_0 is typically chosen to be a small multiple of $\langle \mathbf{r}(\Delta = 1) \rangle$. This probability scales as $\sim t^{\alpha(d - d_f)/2}$ with a subdiffusion exponent α and system dimension d. Figure 5.10 shows that this probability remains constant, and so $d = d_f$ and there is no underlying fractal structure.
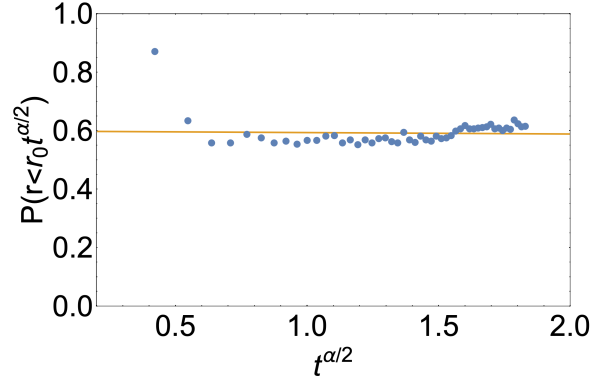
Figure 5.10. The growing sphere analysis gives the probability that a particle at time t is found within a growing sphere of radius $r_0 t^{\alpha/2}$. The probability scales as $\sim t^{\alpha(d-d_f)/2}$. From the fit (*yellow*) $d - d_f = 0.005$.

5.3.4 Correlations in the motion

All analyses so far point to the Piezo1 subdiffusion following a non-ergodic CTRW model. However, the displacement autocorrelation function, defined as

$$C_{\delta t}(t) = \langle [\mathbf{r}(t + \delta t) - \mathbf{r}(t)] \cdot [\mathbf{r}(\delta t) - \mathbf{r}(0)] \rangle / \delta t \qquad (5.7)$$

can reveal if the motion of the particle is correlated. Figure 5.11 shows the normalized displacement autocorrelation as a function of time. This reveals that the system is anticorrelated from the negative peak around $t = \delta t$. A CTRW has a first moment of zero, and as such, displays no correlation for $t > \delta t$. The anticorrelation behavior at long times is only observed in an FBM model.[15]

Additionally, as observed in Figure 5.4, the time-averaged MSD is not linear in lag time $\langle \overline{\delta^2(\Delta)} \rangle \sim \Delta$ as expected be for a CTRW (unlike $\langle r^2(\Delta) \rangle$ which is sublinear). Instead both $\langle \overline{\delta^2(\Delta)} \rangle$ and $\langle r^2(\Delta) \rangle$ are sublinear, a feature seen in ergodic subdiffusion models like FBM.

127
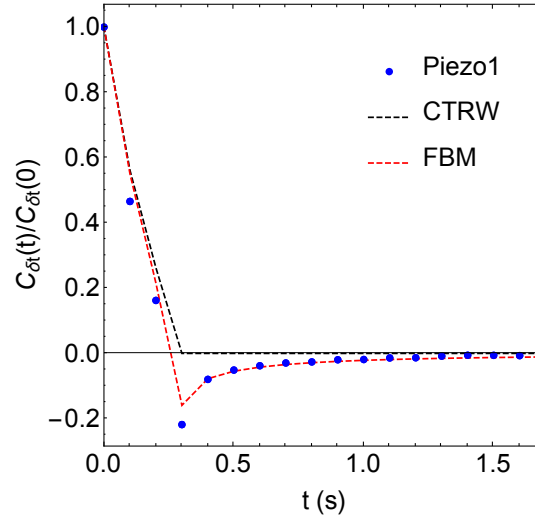
Figure 5.11. The normalize displacement autocorrelation function for $\delta t = 100$ ms. Expressions for the CTRW and FBM models can be found in reference (15). The error bars are smaller than the size of the points.

Another test that differentiates between CTRW and FBM is to calculate the p-variation, $V_n^{(p)}(t)$.[16] This method divides the trajectory into 2^n increments, for which the displacements of these segments are summed and raised to the p power. The scaling of $V_n^{(p)}(t)$ indicates if the process is CTRW or FBM. For FBM, the quadratic variation, $V_n^{(2)}(t)$, diverges as $n \to \infty$, however, a CTRW process stabilizes. As seen in Figure 5.12, calculated for the longest available trajectory (60 s), $V_n^{(2)}(t)$ increases with increasing n, similar to the FBM model.
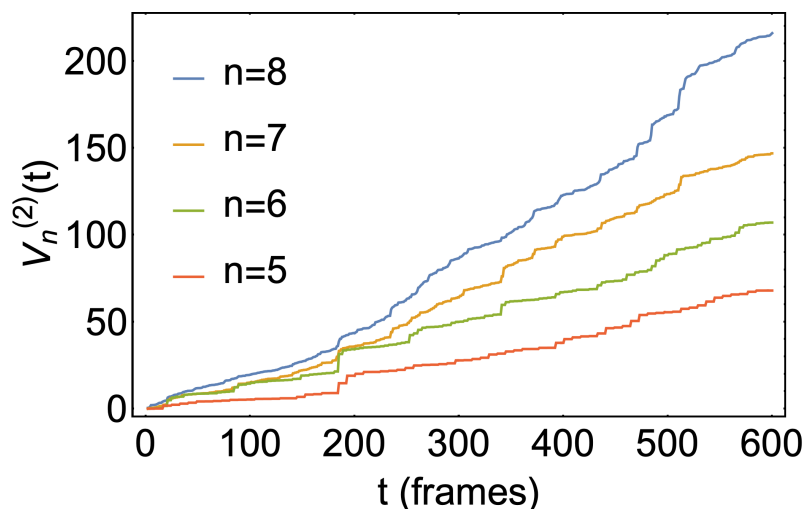
Figure 5.12. The quadratic variation calculated for 2^n increments. The longest trajectory (60 s) was used for this calculation. As n increases, $V_n^{(2)}(t)$ diverges.

5.3.5 Disruption of actin yields an interesting transition

To understand what could be causing the observation of two distinct subdiffusion mechanisms, we followed the lead of Weigel, *et al.*[9] and Tabei, *et al.*[10] Both observed subdiffusion for tracked particles that followed mixed models. Since Piezo1 has been shown to have enriched activity near force-producing regions containing actin and myosin,[8] we used the actin inhibiting drug, Cytochalasin D, to observe the effects on Piezo1 diffusion. Staining experiments showed that concentrations of 50 μM Cytochalasin D had the expected effect of disrupting the actin network, as seen in Figure 5.13. In the untreated cells, the green phalloidin stain for actin was very distinct and well-connected. The actin was evenly spread throughout each MEF cell and was unbroken. In contrast, the MEF cells treated with 50 and 100 uM CytoD had fragmented actin filaments, where the actin was no longer clean and undisturbed. If actin does play a role in Piezo1 diffusion, this perturbation should reveal a change from the untreated cells.
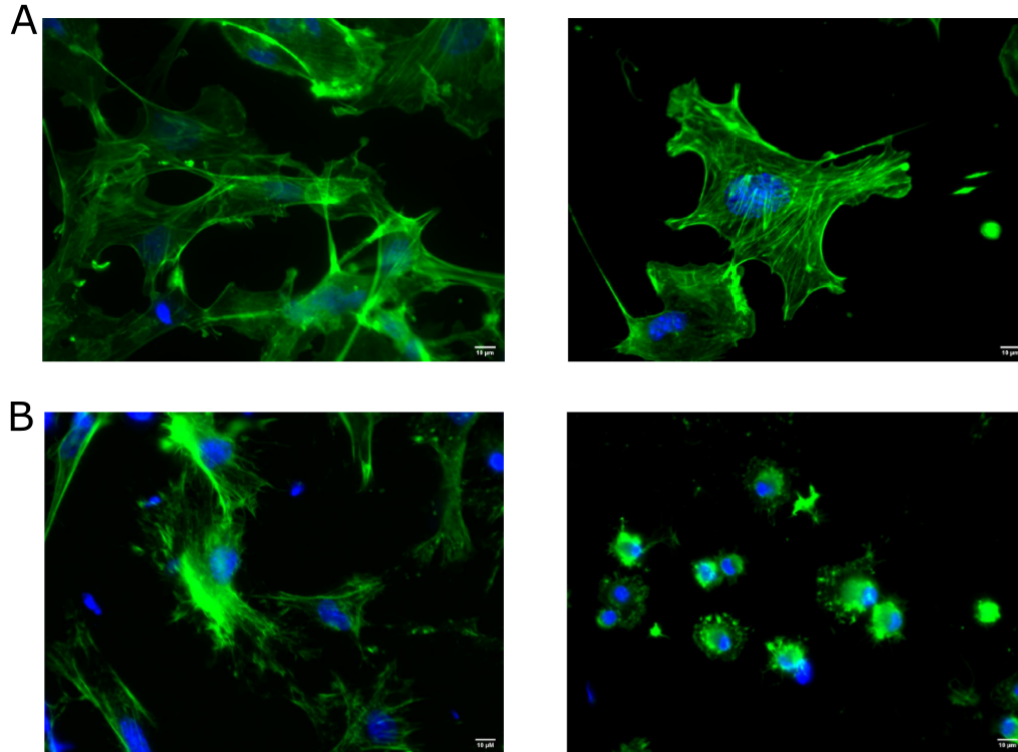
Figure 5.13. Staining experiments for actin in MEF cells. The phalloidin stain for actin is shown in green and the Hoechst stain for the nucleus is shown in blue. (A) The untreated cells have full and well-connected actin networks. (B) The cells treated with 50 µM Cytochalasin D, an actin disrupting drug, shows regions where the actin is less connected and highly fragmented.

Upon treatment with Cytochalasin D, the MSD still displays subdiffusion. Surprisingly, most of

the analyses yielded similar results to the untreated cells, with signs of both CTRW and FBM.

There were two unique features observed, however. The first was a crossover in the MSD at around

8 s lag time where the exponent for both the time and ensemble-averaged MSDs approached $\alpha =$

1, seen in Figure 5.14A. Additionally, the TEA-MSD appears to level off at measurement times

greater than 10 s, as seen in Figure 5.14B. Taken together, this could indicate a transition from

anomalous diffusion to normal Brownian motion. However, verification of this transition would

require longer trajectories to observe the long lag time behavior. An additional direction would be

to classify the individual trajectories based on their proximity to regions of the cell with disrupted

actin and regions free of actin. Selecting out individual trajectories from each of these regions may allow for a more definitive assignment of the change in the diffusion.
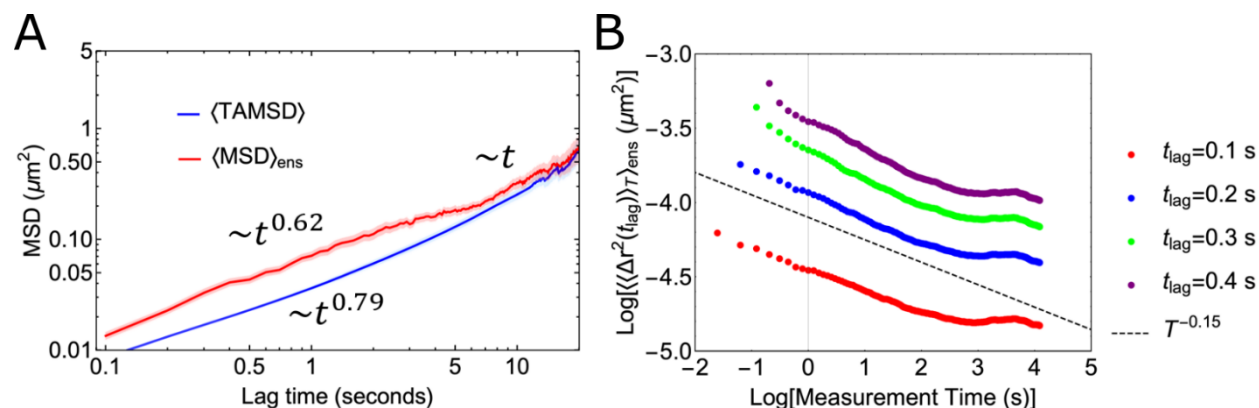

Figure 5.14. MSD analysis after treatment with actin disrupting drug, Cytochalasin D. (A) The time-averaged and ensemble-averaged MSD for 463 tracks. The behavior is subdiffusive at short lag times. At approximately 8 seconds, the behavior of both curves becomes linear with lag time. (B) The TEA-MSD as a function of measurement time plotted as the natural log. Up until a measurement time of approximately 20 s, the TEA-MSD is decreasing. After this, it appears to flatten out, suggesting a change in the dynamics.

5.4 Bibliography

1. Nourse, J. L. & Pathak, M. M. How cells channel their stress: Interplay between Piezo1 and the cytoskeleton. *Semin. Cell Dev. Biol.* 71, 3–12 (2017).

2. Coste, B. *et al*. Piezo1 and Piezo2 are essential components of distinct mechanically activated cation channels. *Science* 330, 55–60 (2010).

3. Coste, B. *et al*. Piezo proteins are pore-forming subunits of mechanically activated channels. *Nature* 483, 176–181 (2012).

4. Li, J. *et al*. Piezo1 integration of vascular architecture with physiological force. *Nature* 515, 279–282 (2014).

5. Ranade, S. S. *et al*. Piezo1, a mechanically activated ion channel, is required for vascular development in mice. *Proc. Natl. Acad. Sci. U. S. A.* 111, 10347–352 (2014).

6. Sugimoto, A. *et al*. Piezo type mechanosensitive ion channel component 1 functions as a regulator of the cell fate determination of mesenchymal stem cells. *Sci. Rep*. 7, 17696 (2017).

7. Pathak, M. M. *et al*. Stretch-activated ion channel Piezo1 directs lineage choice in human neural stem cells. *Proc. Natl. Acad. Sci. U. S. A.* 111, 16148–16153 (2014).

8. Ellefsen, K. L. *et al*. Myosin-II Mediated Traction Forces Evoke Localized Piezo1 Ca^{2+} Flickers. *Biophys. J*. 116, 377a (2019).

9. Weigel, A. V., Simon, B., Tamkun, M. M. & Krapf, D. Ergodic and nonergodic processes coexist in the plasma membrane as observed by single-molecule tracking. *Proc. Natl. Acad. Sci. U. S. A.* 108, 6438–6443 (2011).

10. Tabei, S. M. A. et al. Intracellular transport of insulin granules is a subordinated random walk. Proc. *Natl. Acad. Sci. U. S. A.* 110, 4911–4916 (2013).

11. Ellefsen, K. L., Settle, B., Parker, I. & Smith, I. F. An algorithm for automated detection, localization and measurement of local calcium signals from camera-based imaging. *Cell Calcium* 56, 147–156 (2014).

12. Schütz, G. J., Schindler, H. & Schmidt, T. Single-molecule microscopy on model membranes reveals anomalous diffusion. *Biophys. J*. 73, 1073–1080 (1997).

13. Deverall, M. A. *et al*. Membrane Lateral Mobility Obstructed by Polymer-Tethered Lipids Studied at the Single Molecule Level. *Biophys. J*. 88, 1875–1886 (2005).

14. Tejedor, V. *et al*. Quantitative Analysis of Single Particle Trajectories: Mean Maximal Excursion Method. *Biophys. J*. 98, 1364–1372 (2010).

15. Jeon, J.-H., Monne, H. M.-S., Javanainen, M. & Metzler, R. Anomalous Diffusion of Phospholipids and Cholesterols in a Lipid Bilayer and its Origins. *Phys. Rev. Lett*. 109, 188103 (2012).

16. Magdziarz, M., Weron, A., Burnecki, K. & Klafter, J. Fractional Brownian Motion Versus the Continuous-Time Random Walk: A Simple Test for Subdiffusive Dynamics. *Phys. Rev. Lett*. 103, 180602 (2009).